JACOBS
UNIVERSITY

Computational study of Excitation Energy Transfer Dynamics in Light-Harvesting Systems

by

Suryanarayanan Chandrasekaran

A thesis submitted in partial fulfillment
of the requirements for the degree of

Doctor of Philosophy
in Chemistry

Approved Dissertation Committee:

Prof. Dr. Ulrich Kleinekathöfer
(Jacobs University Bremen)

Prof. Dr. Thorsten Klüner
(University of Oldenburg)

Prof. Dr. Arnulf Materny
(Jacobs University Bremen)

Date of Defense: 24^{th} Nov 2016

Life Sciences & Chemistry

Dedication

I would like to dedicate this thesis to my MOM.

Acknowledgement

This dissertation would not have been possible without the guidance and help of several individuals, who is in one way or another contributed their valuable assistance in the completion of my thesis. First and foremost, my sincere thanks to my supervisor Prof. Dr. Ulrich Kleinekathöfer for his vast support, excellent guidance and inspiration. I would like to thank Prof. Dr. Thorsten Klüner and Prof. Dr. Arnulf Materny for being in my thesis committee and examining my thesis. Furthermore, I am very grateful to our collaborators Stephanie and Prof. Dr. Alan Aspuru-Guzik from Harvard University. In my daily work I have been blessed with many friendly and cheerful people. Special thanks to Meisam, Amigo Carlos (coffee dude), Pothula, Ilaria, Jignesh, Bogdan, Niraj, Hassan, Fabio, Vinay, Naresh and Team Assistant Britta.

I am also very grateful to my family for their vast support and being the backbone of life.

Finally I would like to thank DAAD and Jacobs University for generous funding to support my PhD. They have helped me not only transform my scientific career, but also my personal life with lot of inter-cultural experience.

Danke!
Thanks to all of you!

Abstract

Photosynthesis is one of the key processes to sustain life on earth. The initial step of photosynthesis involves capturing the sunlight by pigments in so-called light-harvesting complexes and transferring the excitation energy towards the reaction center where charge separation processes take place. In subsequent steps, the respective energy is used for the production of ATP. The transfer efficiency of the excitation energy to the reaction center might be enhanced by quantum effects. The detailed mechanism of this quantum effects is still under debate. In addition, this kind of quantum coherence effects might also help to improve the efficiency of (organic) solar cells. Sun light is not only used by plants as primary source of energy production but also bacteria and algae. In this thesis light-harvesting complexes from bacteria and algae are investigated theoretically. To this end, a multi-scale approach is employed using classical molecular dynamics simulation with subsequent electronic structure calculations and quantum dynamics. The Fenna-Matthews-Olson (FMO) complex of green sulfur bacteria and the Phycoerythrin 545 (PE545) antenna of marine algae are studied in detail. To be able to perform molecular dynamics simulations, one needs to obtain the respective force fields. Thus, here comparison between two different force fields for a bacteriochlorophyll molecule is carried out. As a test the so-called spectral density was determined, which describes the energy-dependent coupling between pigment and environment. Furthermore by calculating the excitonic coupling among the pigments, the population dynamics was determined using an ensemble-averaged wave packet formalism. In additon, a new parametrization of the bacteriochlorophyll *a* molecule was performed using the CGENFF formalism. Finally, the light-havesting complex PE555 has been simulated and compared to similar PE545 aggregate. The excitation energy transfer dynamics in the PE555 complex was determined using different sets of excitonic couplings.

List of Abbreviations

BChl a bacteriochlorophyll a

CGenFF CHARMM General force field

DFT Density-functional theory

EDA extended dipole approximation

EET excitation energy transfer

FF force field

FMO Fenna-Mathews-Olson

HF Hartree-Fock

LHC light-harvesting complex

MD molecular dynamics

PDA point dipole approximation

PE pycoerythrin

QM quantum mechanics

QM/MM quantum mechanics/molecular mechanics

RC reaction center

TrEsp Transition Electrostatic Potential charges

Contents

Chapter 1

Introduction

"If we want to describe what happens in an atomic event, we have to realize that the word "happens" can only apply to the observation, not to the state of affairs between two observations."

– Heisenberg (1958)

Photosynthesis is a key process to sustain life on earth. This process acts as the source of energy production in plants, algae, bacteria and in certain protistans using sunlight. In the oxygenic photosynthetic process carbon dioxide and water reacts to form glucose and oxygen as products [1]. The formed glucose is then converted into pyruvate which releases adenosine triphosphate (ATP) by cellular respiration [2]. In some cases photosynthetic process is anoxygenic, i.e., it does not produce oxygen as byproduct, instead a free electron will be used to oxidize inorganic compounds like hydrogen sulfide, sulfur compounds, hydrogen or ferrous iron. The anoxygenic photosynthetic process takes place in some bacterial systems (phototrophic green and purple bacteria [3]). The study of this mechanism has received tremendous interest due to the existence of this organisms in sludge, muddy or deep ocean environment under minimal sunlight conditions. After extracting and analyzing, the proteins present in these organism show the existence of light-harvesting complex (LHC). These complexes consist of chromophore molecules placed into proteins allowing for transfer of excitons, i.e., electron-hole pairs, formed by the absorption of sunlight. The 1988 Nobel Prize in chemistry was awarded to Johann Deisenhofer, Robert Huber and Hartmut Michel, for revealing the atomic structure of a membrane-bound protein that drives photosynthesis in a purple bacterium [4, 5]. The various types of bacterial systems have different LHC [6],

Figure 1.1: The plane *Solar Impulse 2* plane is shown. The wings of the plane have 17,000 solar cells which charge batteries to also run the flight propellers overnight. The ideal flight speed is 28 mph that can double during daytime [9].

which makes these kind of systems able to adopt to the respective complex environments. For instance, plant leaves contain the green pigment chlorophyll, while bacterial species contain bacteriochlorophyll molecules. The type of LHC existing in various organisms depends, at least to some degree, upon the amount of sunlight it is exposed. In some cases, LH complexes have mixed LH antenna pigments (BChl, BPh and carotenoid [7, 8]) or similar chemical compounds with changes in the functional groups of their side chains (BChl a, b, c, d, e and g) of the LHC complex.

In recent years the demand or need for renewable energy has attracted huge attention due to the depleting fossil fuel and increasing environmental pollution. To overcome this problem, one can use naturally available non-depletable energy resources such as sun, wind or geothermal heat energy. Of all the various newly available alternative technologies (bio fuel, bio gas and hybrid technologies) solar energy powered devices have got huge potential in smart materials industry (see, for example, Fig. 1.1). The sun is the source of solar energy in form of solar radiation and is located 90 million miles away from the earth. Despite traveling this long distance, the earth receive 120 Petawatt ($10^{15}W$) of incoming solar radiation [10]. Of this energy, large amounts get absorbed by oceans, clouds and land masses. Thus, by tapping this huge amount of energy one can produce megawatts (MW) of solar energy. Solar cells are already used as a power source in a lot of devices, such as solar cell powered calculators, watches, solar chimneys and so on. The solar cell market has shown a 23 percentage increase in over 9 years [11]. The recent development in rechargeable and highly efficient batteries and inverters along with a more efficient solar cell technology helps in the growth

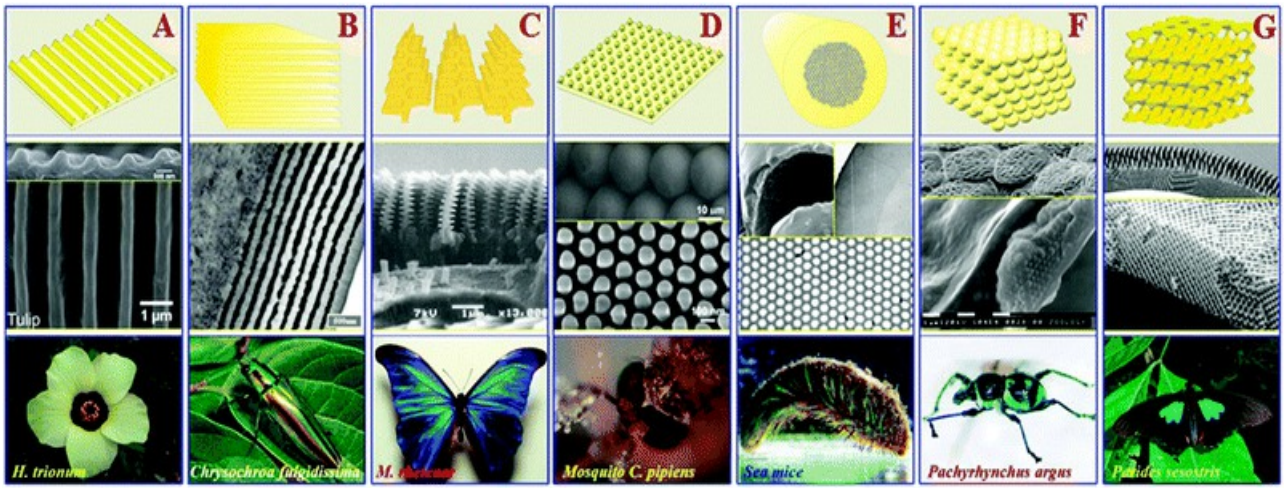

Figure 1.2: The figure shows the natural organisms (bottom row) and well patterned nano structures (middle row) in it. The 1D and 2D periodicity (top row) in the form of cylindrical and layered sheets of high-refractive-index medium exist in iridescent hair, skin or in some body parts of insects, birds, fish, plant leaves, berries, algae, etc. [14]

of the solar cell market. The basic function of a solar cell is very simple, when sunlight is absorbed by light-absorbing material, excitons and/or charge carriers (electrons and holes) will be generated and transported to a conductive contact that will transmit the electricity. Since the charge carrier mobility is controlled by the molecular assembly (morphology) [12, 13] or nonstructural patterns, the study of light absorbing material might help in increasing its conductivity. Since light absorption and charge separation processes also happen in photosynthesis, the understanding of the underlying mechanisms is of large importance in order to design even more efficient light absorbing devices. In the following section we give a brief overview of the connection between the structure-function relationship of natural LH systems and synthetic nanostructures.

1.1 Molecular assembly and Organisation

Nano-scale structures are of profound interest in emerging areas of science [15–17]. The changes in the dimension of the particle result in quantum effects at the nanoscale leading to variations in melting point, fluorescence, electrical conductivity, magnetic permeability and chemical reactivity. Moreover, the advances in microscopic techniques such as transmission electron microscope (TEM) and atomic force microscope (AFM) help in determining the alignment and arrangement on the nano and the micro scale. A recent review by Zhao et

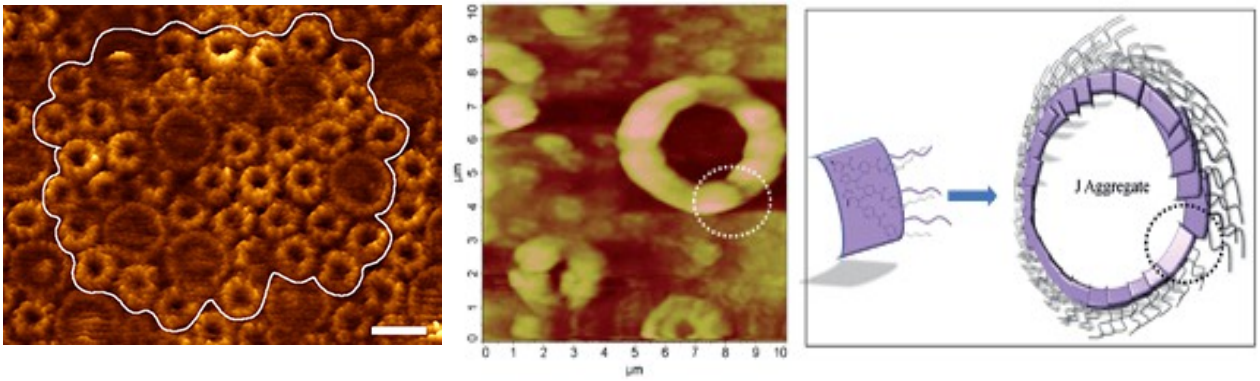

Figure 1.3: The AFM scanned image of LHCs purple bacteria (*Rhodospirillum molischianum*) is shown in the left panel [18] . The middle panel shows the AFM image of thiophene based mesogenic self organized polymer. The right panel shows the schematic illustration of J aggregate formation in the same polymer [19].

al. [14] has reported the significant advantages of bio-inspired nanostructures and the role of molecular self organization from natural organisms as a basis for future smart materials.

Hereby, I would like to discuss my previous research findings in the field of thiophene-based self organizing mesogens [19] for the study of organic smart materials (solar cells, thin film transistors, organic light emitting diodes (OLED), etc.,). This kind of organic or polymeric materials is found to be cost effective compared to conventional inorganic solar cells or silicon based solar cells. Thiophene-based hetero-conjugated polymers are found to exhibit excellent semiconductor properties because of their low band gap [20]. The thiophene-based polymers like n-hexyl thiophene have been found to feature a large charge carrier mobility in the case of highly ordered or oriented films [12]. One can vary the band gap of this polymers by simply changing the side chain functional groups or the main chain ordering by donor-acceptor moieties [21]. Hence, we have designed molecules with a mesogenic functional group in the side chain of the thiophene unit to obtain a self organizing property. AFM (atomic force microscope) morphology studies along with optical techniques have shown that octyl and decyl (alkyl groups) side chains exhibit circular concentrated ring patterns (Fig 1.3) along with higher absorption properties. Further studies have been carried out using Langmuir blodgett film studies [22] to monitor the average area occupied by the molecule and the changes in the molecular orientation. Interestingly the area occupied by the same octyl and decyl group (circular domain forming structures) were found to be higher. This study has its own significance since this kind of circular domain structure also exists in natural LH2 ring systems (Fig 1.3). In the following section the Fenna-Mathews-Olson (FMO) and PE555 LHC structures and the respective chromophoric pigments are discussed in some detail.

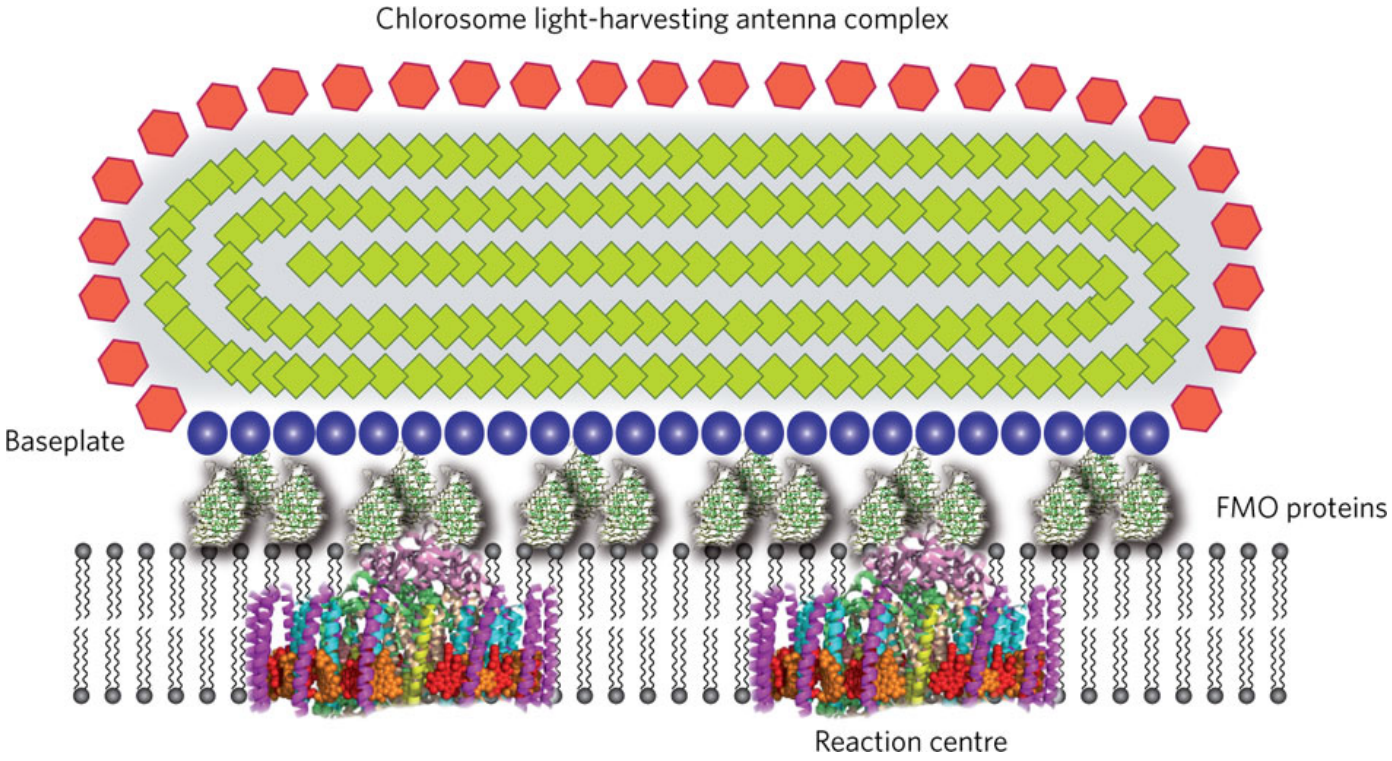

Figure 1.4: The figure shows the schematic representation of FMO complexes sandwiched between baseplate and respective reaction center (placed in a lipid bilayer membrane) [23]. The role of the FMO complexes is to act as a molecular wire to transfer the absorbed sunlight from its LHCs to the LHCs in reaction centre. The reaction center is the core of the structure which includes protein and bacteriochlorophyll (BChl) pigments. The FMO complex includes BChl-a pigments, the baseplate also contains proteins which act as a mediator between the chlorosome antenna complex and the FMO complex. The chlorosome is a large lamellar organization of protein containing 2,00,000 bacteriochlorophyll-c molecules.

1.1.1 Fenna-Mathews-Olson complex

The Fenna-Mathews-Olson (FMO) of green sulfur bacteria was first discovered in 1962 by Olson et al. [24, 25]. Green sulphur bacteria harvest sunlight in large pigment-containing vesicles known as a chlorosomes and the excitation energy is transported to reaction center (RC) for charge separation (Fig. 1.4). During this process FMO acts as a molecular wire in transporting the excitation absorbed by the chlorosome to get to the reaction center. FMO was the first structurally resolved water soluble protein complex containing 24 bacteriochlorophyll a (BChl a) pigments as shown in Fig. 1.5 [26]. The complex itself is organized in a protein trimmer form with 8 BChl a in each monomer [27]. Inside the protein, BChl a molecules are bound to amino acids histidine and aspartate. As excitation is passed between BChl a molecules in chlorosome to those in FMO and finally to those in the reaction center

(RC), it is constantly under the influence of thermal fluctuations. It is has been found that FMO can efficiently conduct excitation energy, i.e., without much energy loss. One way to do this could be by exploiting quantum coherence to speed up energy transfer [28, 29]. Further study has been carried out to determine the position and role of BChl a pigment inside FMO complex. A recent crystal structure elucidation has shown the existence of an eighth pigment per monomer [30]. Despite various theoretical studies, the role of the weakly bound eighth complex is not completely clear up to now. A recent hypothesis by Renger et al. [31] is that the eighth pigment might act as an exciton bridge between BChl 1 and 2 of another monomer. A further interesting observation by time-resolved optical spectroscopy is that BChl 3 drains the absorbed energy to the reaction center [32].

The chemical structure of the BChl a pigment differs from the Chl a pigment in its acetyl side chain functional group. Several modifications of BChl a occur among different photosynthetic organisms [33–36]. Accessory pigments (BChl b, c, d, e and g) absorb energy that BChl a does not absorb. The absorption of the BChl a molecule is around the violet-blue (400 nm) and the reddish orange (700-900 nm) wavelengths. The BChl a molecule also has an extended conjugation in the central ring with alternating π bonds. Thus, on exposure to sunlight, the molecule gets photo-excited resulting in a $\pi - \pi^*$ transition making it highly chromophoric. The transition dipole moment and the absorption properties of individual BChl molecules have found to vary based upon the solution used for the study [37].

1.1.2 PE555 aggregate

Cryptophytes are unicellular algae that contain pycoerythrin (PE) or phycocyanin (PC) aggregates inside their thylakoid membrane. The absorption range of phycobilins is usually in the higher wavelength range (red, orange, yellow, and green). Based upon the living water conditions, the light absorption properties vary. For instance, phycobilins found in deep, shallow waters tend to capture red and yellow light. Plant systems have phyllobilins, tetrapyrrolic and bilin-type chlorophyll pigments [38]. They are formed in leaves as side products of the chlorophyll catabolites degradation process which is responsible for the decolouration (green to yellow) of leaves in spring season [39]. In this study we focus on pycoerythrin (PE) complex of algal species, the PE complexes is found on the center intrathylakoid space which capture the initial sunlight later on the exciton formed is transferred to the core photosystem I (PS I) or PS II for charge separation process.

The phycoerythrin (PE555) (Fig. 1.5), extracted from the bacterium *Hermiselmis an-*

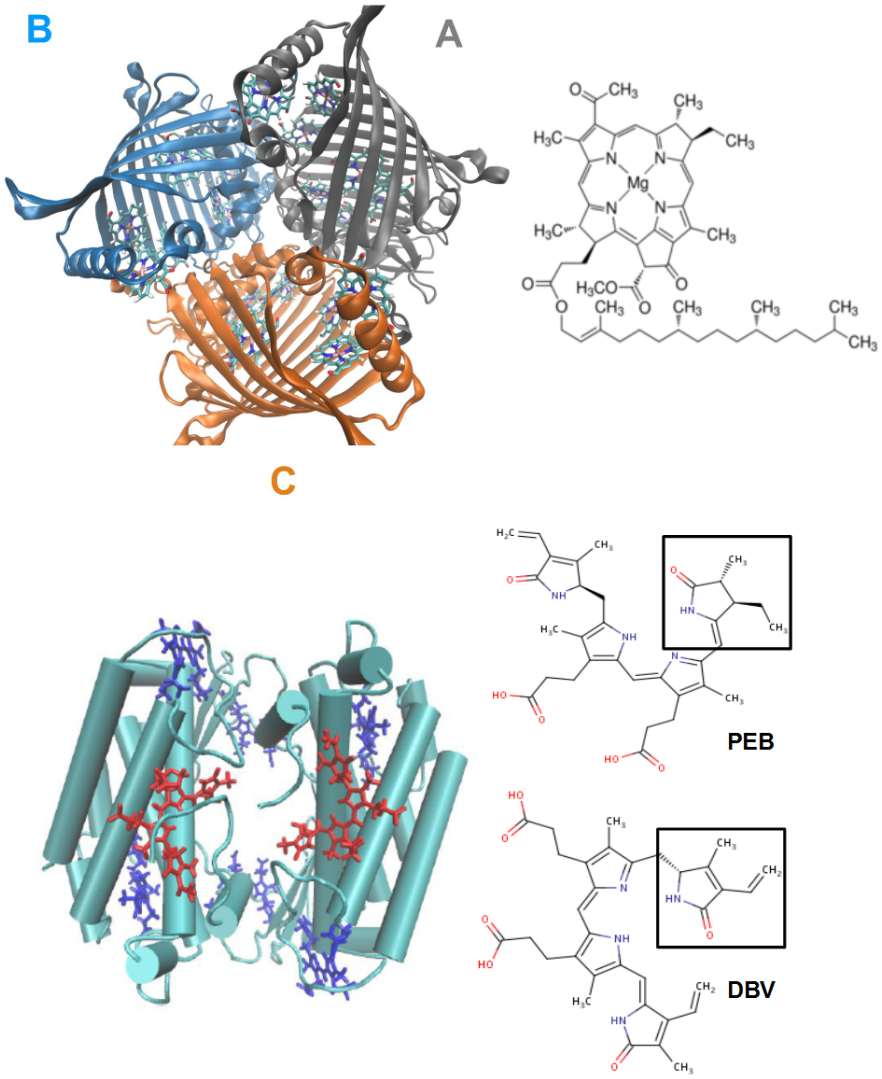

Figure 1.5: The FMO trimer complex (PDB id: 3EOJ) of *Prosthecochloris Aestuarii* is shown in the top panel together with the pigment BChl a. A structure of the PE555 LHC aggregate (PDB id: 4LMX) of the bacterium *Hermiselmis andersenii* is shown in the bottom panel. The phycoerythrobilin (PEB) and dihydrobiliverdin (DBV) pigments are shown in the bottom panel right. The square boxes over the PEB and DBV pigment shows the chemical structural difference ($C = C$) among them.

dersenii (PDB id: 4LMX) [40] is studied in detail. The PE555 aggregate contains 4 phycoerythrobilin (PEB) and 2 dihydrobiliverdin (DBV) pigments connected through cysteine unit to the protein. Almost all the phycobiliproteins are structurally similar, it has $\alpha\alpha'\beta_2$, that each α subunit contains one bilin chromophore, each β subunit carries three bilins. The phycobilins are named after there absorption spectrum maximum. So for three types of cryptophyte phycoerythrins (PE) PE 545, PE 555 and PE 566 and five types of cryptophyte

phycocyanins (PC) PC 569, PC 577, PC 612, PC 630 and PC 645 have been determined from variously existing 200 cryptophyte species. It is also found that based upon the light conditions the antenna size varies. The study of the PE555 complex along with FMO complex is significant because the pigment fluctuation in the later complex is dependent on the environment (protein), while PE555 is independent [98]. Further detailed study was carried out in comparison with its homolouge PE545 complex to see the effect of protein environment fluctuation. A more detailed description of the protein and its pigment organization is given in Chapter 4.

1.2 Molecular Dynamics Simulations

Computer simulations act as a tool to predict the observations from (macroscopic) experiments at a microscopic level: Atomic simulations help in predicting the complex working mechanism existing in nature (proteins, DNA etc, ...) [41, 42] and in man-made systems (semiconductors, polymers etc, ...) [43, 44]. Thus, molecular dynamics invented by Alder and Wainwright in 1959 [45] is used as a primary tool to study biological molecules, the behavior of molecular systems including its fluctuations as well as conformational changes of proteins and nucleic acids. Classical molecular dynamical simulations have already found a vast amount of applications in many fields including DNA docking studies [46], artificial neural network studies [47] and so forth. The principle underlying MD simulations is Newton's second law of motion:

$$\vec{F}_i = m_i \vec{a}_i = m_i \frac{\partial^2 \vec{r}_i}{\partial t^2} \tag{1.1}$$

where $\vec{F}_i$ is the force exerted on particle i, m_i is the mass of particle i and $\vec{a}_i$ is the acceleration of particle i. Thus, the present atom positions $\vec{r}_i$, velocities and accelerations yield the positions and velocities at the next moment in time. As already stated in the introduction, molecular dynamical simulations involve a simplified description of the complex interaction potential between all particles. So-called force field (FF) fitted from quantum calculations are used to approximate this multi-particle interaction. The usual description of FF has bonded and non-bonded terms. The non-bonded terms involve Coulomb and Van der Waals terms to describe long range force of interaction, while the bonded term involves bond stretching, angle bending, dihedral and improper angle terms.

In the present thesis, MD simulation are performed for proteins and ligands of light

harvesting complexes. The atomic coordinates of the system can be taken from X-ray resolved crystal structure [48] or NMR (Nuclear Magnetic Resonance) spectroscopy [49, 50]. From the available chemical structure, the simulation system is build by placing the system in a water box and ions are added to keep the system neutral or at given experimental pH. Simulations can be performed using different ensembles, i.e., NPT, NVT or NVE (N - number of particles, P - pressure, V - volume, T - temperature and E - energy) with constant number of particles, constant pressure, constant volume and/or constant energy. The NVT and NPT ensembles are the ones most commonly used. Due to the limitation of the simulation system size, periodic boundary conditions (PBC) are employed to simulate an infinite number of mirror images of the unit cell in all directions. The PBC can be used in conjunction with Ewald summation method as cuttoff for electrostatic interaction. However care should be taken in taking bigger enough cell size to avoid artifacts. Once the simulation parameters are set Newton's second law, one often uses the Velocity Verlet algorithm or the Leap Frog scheme [51].

The timescales of the simulation vary according to the purpose of the study. For example, in order to study intra-molecular bond changes, nanosecond simulations are long enough. Standard MD simulations vary from tens to hundreds of nanoseconds. However, for protein docking or protein folding studies of microsecond length will be needed. Very recently, there have been various efforts to simulate large scale systems like HIV viruses [52] containing 64 million atoms and photosynthetic units (PSU) of purple photosynthetic bacteria of approximately 70 nm cell size containing about 4.000 BChl a [35]. The above studies have not only proven the significance of molecular dynamics but the scale of computer power that can be used nowadays for studying large prototypes. However, one can also achieve, such kind of large scale simulation using coarse-grained model [53] or using Brownian dynamics simulation [54, 55] when atomic details are not of major importance. FF sets combine all parameters for a large class of systems. The sets are classified based on the optimization methods used for protein, ions, water and so forth. For example, some of the Class I [56] FF are CHARMM, AMBER, OPLS and GROMOS and Class II FF are CFF95 (Accelrys), MMFF94 (CHARMM, Macromodel) and UFF (universal FF). The total energy function in terms of force fields can be given by a sum of intra-molecular bond terms and intra- and inter-molecular nonbonded terms:

$$E_{tot} = E_{bond} + E_{nonbond} \tag{1.2}$$

In the present thesis we have used the CHARMM [57] and AMBER [58] FF sets for

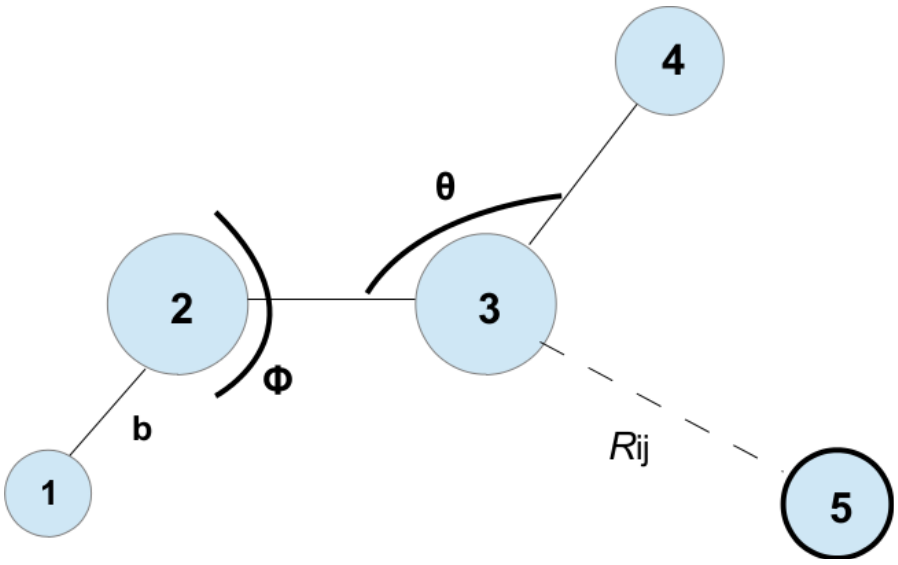

Figure 1.6: Schematic representation of the FF interactions. Bonded parameters are indicated by solid lines while the non-bonded interactions are depicted by dotted lines.

studying the FMO complex and PE555 aggregates, respectively. The general expression for the bonded and non-bonded terms is given below:

$$E_{bond} = \sum_{\text{bonds}} K_b(b - b_0)^2 + \sum_{\text{angles}} K_\theta(\theta - \theta_0)^2 + \sum_{\text{dihedrals}} K_\phi(1 + \cos(n\phi - \delta)) + \sum_{\text{impropers}} K_\omega(\omega - \omega_0)^2 \tag{1.3}$$

The bonded terms consist of bonded interactions (1-2 term), angle term (1-3 term) and dihedral angle (1-4 term) and improper angle (1-4 term) as shown in Eq. 1.4 and Fig. 1.6. Bond and angle terms are represented by a simple harmonic expression, while dihedral energies are represented by using a combination of cosine functions. The terms K_b, K_θ, K_ϕ and K_ω are the constants of the bond, angle, dihedral and improper angle terms as well as the dihedral terms. The parameters δ are determined with respect to the respective bond and angle terms. The non-bonded energy terms are given by Eq. 1.4, where the van der Waals (vdW) interactions are represented by a 6-12 Lennard-Jones potential and the electrostatic interactions are given by the Coulomb interaction of atom-centered point charges. The atomic partial charges are derived by fitting the molecular QM electrostatic potential. A detailed discussion of the FF parameterization and methods is given in chapter 2.

$$E_{nonbonded} = \sum_{\text{nonbonded}} \varepsilon \left[\left(\frac{\vec{R}_{\min,ij}}{\vec{r}_{ij}} \right)^{12} - 2 \left(\frac{\vec{R}_{\min,ij}}{\vec{r}_{ij}} \right)^{6} \right] + \frac{q_i q_j}{4\pi\varepsilon_o \vec{r}_{ij}} \tag{1.4}$$

where, r_{ij} is the distance between the particles, $R_{\min,ij}$ is the distance of the energy minimum and ε the depth of the minimum. As r_{ij} goes to infinity the energy goes towards zero. The term $\sim 1/r^{12}$, dominating at short distance, models the repulsion between atoms when they are brought very close to each other. The term $\sim 1/r^6$, dominating at large distance, constitute the attractive part. There are no theoretical arguments for choosing the exponent in the repulsive part of LJ to be 12 or 6, this is purely a computational convenience. The electrostatic coupling is given by the Coulomb potential. In this q_i and q_j are the charges of individual atoms of interest seperated by distance r_{ij}. In the present MD simulations the CHARMM and AMBER FFs are used for studying proteins, water, ions and other types of molecules in FMO and PE555 systems. For proteins in the case of AMBER the *ff99SB* is used. It is considered better than previous *ff94* because of its improved backbone parameters. For the CHARMM simulations, we have used the *CHARMM22* parameters for the proteins and the lipids. For water molecules different models exist [59]. In general, these models are classified by different properties. (i) The number of sites employed, e.g. TIP3P or TIP4P. In these models the partial atomic charges are placed at three atoms or four (one additional ghost) atoms whereas only oxygen atoms have the Lennard-Jones (LJ) parameters. (ii) The rigidity of the model is another classification scheme as well as (iii) the inclusion of polarization effects. Since the number of water molecules involved in an explicit water simulation can be very high, a trade-off between the computational complexity of the model and the size of the system has to be achieved. One possibility is to keep the O-H bond lengths and H-O-H bond angle frozen. For non-standard molecules, various individual parameterization procedures are available. A detailed discussion on parameterization for organic molecules is given in the FF chapter.

1.3 Quantum mechanical approaches [1]

Since MD simulations cannot be used in electronic structure calculations, quantum mechanics (QM) calculation are done for molecules to understand the physical (thermodynamics vs

[1] The contents in this section are taken from standard text books [60–63] and lecture notes.

kinetic control of reaction mechanisms) and chemical properties (free radical reaction mechanisms) of reactants or products. In QM calculations the atoms or molecules degrees of freedom have been treated by a given set of rules and approximations.

In 1926 Erwin Schrödinger proposed that any continuous time-independent wave function of mass m moving in one dimension with energy E can be written as:

$$H\Psi(\vec{x}) \equiv -\frac{\hbar^2}{2m}\frac{\partial^2\Psi(\vec{x})}{\partial\vec{x}^2} + U(\vec{x})\Psi(\vec{x}) = E\Psi(\vec{x}) \tag{1.5}$$

where the Hamiltonian operator ($\hat{H}$) can be described by a sum of $U(\vec{x})$, the potential energy, and a kinetic energy term of the time-independent wave function ($\Psi(\vec{x})$) of the particle at position $\vec{x}$.

For the theory of many body systems containing several atoms, a more complex description of the nuclear and electronic wave functions is needed. In this case the molecular Hamiltonian operator is given by:

$$H_{(r,R)} = \sum_{I=1}^{N_I}\frac{\vec{P}_I^2}{2M_I} + \sum_{i=1}^{N_i}\frac{\vec{P}_i^2}{2m_e} + \frac{1}{2}\sum_{j\neq i}^{N_i}\frac{1}{4\pi\epsilon_o}\frac{e^2}{|r_i - r_j|} + \frac{1}{2}\sum_{J\neq I}^{N_I}\frac{1}{4\pi\epsilon_o}\frac{Z_I Z_J e^2}{|R_I - R_J|} - \sum_{i=1}^{N_i}\sum_{I=1}^{N_I}\frac{1}{4\pi\epsilon_o}\frac{Z_I e^2}{|R_I - r_i|}$$

$$\equiv T_N + T_e + V_{ee}(\vec{r}) + V_{NN}(\vec{R}) + V_{eN}(\vec{r},\vec{R}) \tag{1.6}$$

In this expression, m denotes the mass of the electron, N_I the number of nuclei with coordinates $\vec{R}_1, ..., \vec{R}_N \equiv \vec{R}$, momentum operator $\vec{P}$ is given by $\vec{P} = -i\hbar\frac{\partial}{\partial\vec{x}}$ and masses $M_1, ..., M_N \equiv M_I$. The N_i electrons are described by coordinates $\vec{r}_1, ..., \vec{r}_{N_i} \equiv \vec{r}$, momenta $\vec{P}_1, ..., \vec{P}_{N_i} \equiv \vec{P}_i$, mass m_e is the mass of the electron. Z_I and Z_J denote the charges of the electron and nucleus. A simplified form given in the second row of Eq. 1.6. The T_N, T_e represents the nuclear and kinetic energy operators and V_{ee}, V_{eN} and V_{NN} are the electron-electron, electron-nuclear, and nuclear-nuclear interaction potential operators, respectively.

Since solving the exact wave function of the multi-particle system is exceedingly complicated for larger systems, one needs to use the *Born-Oppenheimer* approximation to simplify the problem. It is based on the principle that the masses of the nuclei are much heavier than that of the electrons. Thus the motion of the electrons are faster than that of the nuclei and therefore the nuclei can be treated as fixed particle while solving the Schrödinger

equation for the electronic degrees of freedom. Using this approximation, one can neglect the kinetic energy (K.E.) of the nuclei from the total Hamiltonian and the electronic wave function depends parametrically on the nuclei as $\Psi(\vec{r},\vec{R}) = \psi(\vec{r},\vec{R}_a)\chi(\vec{R})$. Since the nuclei positions ($\vec{R}$) are fixed, we can solve the electronic wave function $\psi(\vec{r},\vec{R}_a)$ for a particular fixed nuclei value $\vec{R}_a$ to obtain the electronic potential energy surface. The reduced form of pure electronic Hamiltonian can be written as:

$$H_{el} = T_e(\vec{r}) + V_{eN}(\vec{r},\vec{R}_a) + V_{ee}(\vec{r}) \tag{1.7}$$

Thus, by first solving the above given electronic Hamiltonian and later solving the equations for the nuclei separately, one can determine the total energy $E(\vec{r},\vec{R})$ of the molecule.

The Hartree-Fock (HF) theory is one the simplest approximate theories for solving the many-body Hamiltonian for a multi-electron atom or a molecule as described in the *Born-Oppenheimer* approximation. The molecular orbital is calculated by the linear combination of atomic orbital (LCAO) as given below:

$$\Psi = \sum_i c_i \psi_i \tag{1.8}$$

where Ψ is the molecular orbital equals to the sum extends over all atomic orbitals ψ_i of the molecule and c_i are the orbital coefficients of the respective atomic orbitals. The occupation of electrons in each individual orbital will be according to the Pauli exclusion principle. According to this principle, not two electrons of the same spin are allowed to fill the same orbital. A spin-orbital is a product of an orbital wavefunction and a spin function and given in the form of $\phi_a(\vec{x}_i;\vec{R})$, where $\vec{x}_i$ is the spin-space coordinates of electron i.

The spin-orbitals that give the best n-electron determinantal wavefunction are found by using variation theory. The total wave function of the molecule can be written as a Slater determinant as given below:

$$\Phi(1,2,...,N) = \frac{1}{\sqrt{N!}} \begin{bmatrix} \phi_a^\alpha(1) & \phi_b^\beta(1) & ... & \phi_z^\beta(1) \\ \phi_a^\alpha(2) & \phi_b^\beta(2) & ... & \phi_z^\beta(2) \\ \vdots & \vdots & \ddots & \vdots \\ \phi_a^\alpha(N) & \phi_b^\beta(N) & ... & \phi_z^\beta(N) \end{bmatrix} \tag{1.9}$$

In this formula, N corresponds to the number of electrons in the molecule. The distribution

of electrons is done with respect to the atomic orbitals $\phi_{a..z}$ with electron spin α or β. The corresponding spin orbitals obey the orthonormality conditions ($\langle\alpha|\alpha\rangle = 1; \langle\alpha|\beta\rangle = 0$). Then using the variational principle once can obtain the lowest energy eigen states.

$$\epsilon = \frac{\langle\psi|H|\psi\rangle}{\langle\psi|\psi\rangle} \tag{1.10}$$

Here, we assume that there is some overlap between the ansatz and the ground state. The denominator is assumed to be a normalized wave function $\langle\psi|\psi\rangle = 1$, to be able to minimize the energy: $\epsilon = \langle\psi|H|\psi\rangle$. In the case of symmetric energy expression, we can employ *variational theorem* to obtain better approximate minimum energy. It uses the trial wave function at the begining to obtain the lowest value of ϵ, which corresponds to the ground state E_o of the atom and molecule. The variational principle minimization procedure is used in Hartree-Fock (HF) and Ritz method for calculating the ground state Hamiltonian.

The HF equation for spin-orbital $f_1\phi_a(1)$, where we have arbitrarily assigned electron 1 to spin-orbital ϕ_a, is given by:

$$f_1\phi_a(1) = \epsilon_a\phi_a(1) \tag{1.11}$$

Where, ϵ_a is the spin-orbital energy and f_1 is the fock operator:

$$f_1 = h_1 + \sum_u 2J_u(1) - K_u(1) \tag{1.12}$$

Where, h_1 is the core hamiltonian or hydrogenic hamiltonian for electron 1 in the field of a bare nucleus of charge Ze. The sum is over all spin-orbitals $\vec{u} = \vec{a}, \vec{b}, ...\vec{z}$, and the **Coulomb operator,** J_u and the **exchange operator,** K_u are defined as follows:

$$J_u(1)\phi_a(1) = j_0\left\{\int \phi_u^*(2)\frac{1}{r_{12}}\phi_u(2)\partial\vec{x}_2\right\}\phi_a(1) \tag{1.13}$$

$$K_u(1)\phi_a(1) = j_0\left\{\int \phi_u^*(2)\frac{1}{r_{12}}\phi_u(2)\partial\vec{x}_2\right\}\phi_u(1) \tag{1.14}$$

Where, $j_0 = \frac{e^2}{4\pi\epsilon_o}$, The Coulomb and exchange operators are defined here in terms of spin-orbitals. In terms of spatial wavefunction the general expression for HF is given by:

$$Fc = \epsilon Sc \tag{1.15}$$

Here, ϵ and c denotes the atomic orbital energies and coefficient respectively, S is the overlap matrix between basis functions, and F is the Fock matrix of atomic orbitals (for eg: ψ_μ and ψ_ν) is given by:

$$F_{\mu\nu} = \langle \psi_\mu | F | \psi_\nu \rangle;\ S_{\mu\nu} = \langle \psi_\mu | \psi_\nu \rangle \tag{1.16}$$

Here, the fock operator (F) contains two parts 1.17, the first is the effective one-electron Hamiltonian and the second term consists of Coulomb J and exchange K operators [63]. The more compact notation of the Fock operator is given by:

$$F_{\mu\upsilon} = H_{\mu\nu} + \sum_i J_{\mu\nu} - K_{\mu\nu} \tag{1.17}$$

Where, the Hamiltonian operator $H_{\mu\nu}$ (similar to the Schrödinger equation) is the sum of kinetic energy (first term) and potential energy operator (second term) for force of attraction between electron j over sum of all nuclei:

$$H_{\mu\nu} = \left\langle \mu \middle| \sum_i h_i + \frac{1}{2} \sum_{ij} \left(\frac{e^2}{4\pi\epsilon_o r_{ij}} \right) \middle| \nu \right\rangle \tag{1.18}$$

Where, the Coulomb ($J_{\mu\nu}$) is the sum of coulombic interaction between $\mu\nu$ and similar type of atomic orbitals $\lambda\sigma$. The exchange ($K_{\mu\nu}$) integrals is the sum of product or multiple two centered atomic orbitals:

$$J_{\mu\nu} = 2 \sum_{\lambda,\sigma} c_\lambda(1) c_\sigma(2) \int \int \mu(1)\nu(2) \left(\frac{e^2}{4\pi\epsilon_o r_{12}} \right) \lambda(1)\sigma(2) d\tau_1 d\tau_2 \tag{1.19}$$

$$K_{\mu\nu} = \sum_{\lambda,\sigma} c_\lambda(1) c_\sigma(2) \int \int \mu(1)\lambda(1) \left(\frac{e^2}{4\pi\epsilon_o r_{12}} \right) \nu(2)\sigma(2) d\tau_1 d\tau_2 \tag{1.20}$$

In this expression, $c_\lambda(1)c_\sigma(2)$ denotes the product of orbital coefficients over all occupied molecular orbitals. Thus, to determine the unknown MO orbital coefficients we start with a initial guess. Then the Fock matrix (F) is constructed and diagonalized to form a new set

of Fock matrix and coefficients. This process is repeated to obtain a set of coefficients. It is known as self-consistent field (SCF) solution. Using a large basis set increases the computational effort to the fourth power but at the same time the accuracy of the orbital coefficients usually will improve. One of the greater drawbacks in HF theory is that by treating electrons as independent particles they only see an average field of the other electrons leading to a poor description of the electron-electron repulsion energy. To overcome this drawback, correlation methods have been developed to find a better match between experimental and calculated energy values [64, 65].

1.3.1 Density Functional Theory (DFT)

One approach to treat the electron correlation is through Density-functional theory (DFT). In this approach, the many electron wavefunction $\Psi(\vec{r}_1, \vec{r}_2, ..)$ is replaced by the electron density, $\rho(\vec{r})$, based on the assumption that the integral of the density defines the number of electron. Therefore,by determining the electron density map of individual atoms and their overlap, the total energy of the molecule is obtained. Moreover, since the system is described by its electron density, the number of degrees of freedom has been reduced to 3 spatial coordinates rather than $3N$ degree of freedom. This fact leads to the advantage of an increasing computational efficiency of a QM calculation since less computer resources are needed [66].

In 1965 Kohn and Sham proposed the DFT method. In this theory, the ground state Hamiltonian of a molecule has been divided into four terms including the total electron kinetic energy E_K and the potential energy term of electron-electron repulsion and electron-nucleus attraction given by $E_{e,e}$ and $E_{e,N}$. The electron repulsion term can be divided into two parts, i.e., the Coulomb (J) and the exchange-correlation term (XC). The KS equation for the one-electron orbitals $\psi_i(\vec{r}_1)$ have the form:

$$\left\{ -\frac{\hbar^2}{2m_e}\nabla_1^2 - \sum_{j=1}^{N}\frac{Z_j e^2}{4\pi\epsilon_0 r_{j1}} + \int \frac{\rho(\vec{r}_2)e^2}{4\pi\epsilon_0 r_{12}} dr_2 + V_{xc}(\vec{r}_1) \right\} \psi_i(\vec{r}_1) = \epsilon_i \psi_i(\vec{r}_1) \tag{1.21}$$

Where, ϵ_i is the KS orbital energies and exchange-correlation potential (V_{xc}) with respect to exchange-correlation energy (E_{xc}) is given by:

$$V_{xc} = \frac{\delta E_{xc}[\rho]}{\delta \rho} \tag{1.22}$$

The E_{xc} can be determined by first solving the exact ground-state KS electron density $\rho(\vec{r})$ then V_{xc} is solved consecutively until the density and E_{xc} is under tolerance limit. The $\rho(\vec{r})$ is a sum of one-electron spatial orbitals $[\psi_i(i = 1, 2, ..., N_i)]$ given by:

$$\rho(\vec{r}) = \sum_{i=1}^{N_i} |\psi_i(\vec{r})|^2 \tag{1.23}$$

This functional attains its minimum value with respect to all allowed densities if and only if the input density or trial density $[\tilde{\rho}(\vec{r})]$ matches the true ground state density, $\tilde{\rho}(\vec{r}) \equiv \rho(\vec{r})$. So by defining E_{xc} properly one can determine the exact ground state energy ($E_o \leq E_{xc}$ of an atom or molecule. The main difference in the choice of various DFT methods is to obtain the best possible electronic description as stated above. Of these there are various theories has been proposed i) Local Density Approximation (LDA) adopting the exchange and correlation energy density of an uniform electron gas, ii) Generalized Gradient Approximation (GGA) assume that the functional depends on the up and down spin densities and their gradient, iii) hybrid GGA, introducing a combination of GGA with Hartree-Fock exchange, iv) long-range corrected (LRC) and Coulomb-attenuating method (CAM) introducing a partition of the two-electron repulsion operator in the exchange functional into short- and long-range parts. Of these one can study methods by employing varying Basis set and functionals. One of the popular and most widely used one is hybrid functional method of B3LYP [67, 68]. It has huge application in predicting ground state properties in organic and inorganic molecules like atomic structure, lattice properties, electronic density, elastic constants and phonon frequencies etc.,

1.3.2 Time Dependent DFT

Since DFT can be used only for ground state calculations the time-dependent DFT (TDDFT) is developed to describe the excited state phenomenon[69]. The extension of DFT method by linear response (LR) method helps in predicting the transition state energy levels and local excitations. The method has become so popular in the last two decades because of its low computational cost and higher accuracy. Because of that it got huge application in predicting excited state electronic structure, bandgap, optical and dielectric properties in

metal/insulator/semiconductor materials [68, 70–73].

The TDDFT method applies TD (transition density) perturbation to the ground state of the molecule to obtain the excited state properties of the molecule. The perturbed transition between the ground and excited state of the molecule depends on the applied electric field and density of the ground electronic state $\rho_o(\vec{r})$ of the molecule. The vertical transition among the different energy levels depends on the energy gap and geometry of the molecule taken. The transition frequency is applied to the time-independent ground state of the molecule to time-dependent excited state of the molecule [61]. We assume that the system, before the application of the external field, is in its ground state determined by the standard time-independent KS equation. The time-dependent KS equation in TD-DFT is given as:

$$\left\{ -\frac{\hbar^2}{2m_e}\nabla_1^2 - \sum_{j=1}^{N}\frac{Z_j e^2}{4\pi\epsilon_0 r_{j1}} + \int \frac{\rho(\vec{r}_2,t)e^2}{4\pi\epsilon_0 r_{12}}dr_2 + V_{ext}(t) + V_{xc}(\vec{r}_1,t)\right\}\psi_i(\vec{r}_1,t) = i\hbar\frac{d}{dt}|\psi_i(\vec{r}_1,t)| \tag{1.24}$$

$$\rho(\vec{r},t) = \sum_{i=1}^{N}|\psi_i(\vec{r},t)|^2 \tag{1.25}$$

where, V_{ext} is the external potential, the exchange-correlation potential ($V_{xc}(\vec{r}_1,t)$) and the density are all time-dependent. So by varying the external potential using the perturbation theory the density can be determined.

1.3.3 Semi-empirical methods

The semiemprical method are primarily based upon Hartree Fock (HF) formalism, but it uses lesser basis set function and limits the two electron integral in Fock matrix element, which makes it computationally less expensive and more efficient for larger molecules. Given below are the certain approximations used in various semi-emprical calculation:

- Only the valence electrons are taken into consideration by taking the core electron and nuclei as single term.
- Electron-nuclei repulsion potential are treated with limited basis set (slater type orbitals). So hydrogen atom has one basis function and the other atoms include only S and P orbitals.

The restricted Fock matrix of semi-emprical method is similar to Fock operator as described in HF (eq. 1.17) can be written as:

$$F_{\mu\nu} = H_{\mu\nu} + \sum_{\lambda\nu} P_{\lambda\sigma}\left[\langle\mu\nu|\lambda\sigma\rangle - \frac{1}{2}\langle\mu\lambda|\nu\sigma\rangle\right] \tag{1.26}$$

It includes the kinetic energy of the single electron ($H_{\mu\nu}$) Hamiltonian along with the nuclei and mean field potential formed by other electrons (eq.1.27). Similarly the ($\mu\nu|\lambda\sigma$) denotes the multi center two-electron integral and ($\mu\lambda|\nu\sigma$) denotes the exchange integral. $P_{\lambda\sigma}$ is an element of the density matrix.

$$H_{\mu\nu} = \left\langle \mu \right| -\frac{1}{2}\nabla^2 - \sum_a \frac{Z_a}{R_a} \left| \nu \right\rangle \tag{1.27}$$

$$P_{\lambda\sigma} = \sum_j^{M_{basis}} c_{\sigma j} c_{\lambda j} \tag{1.28}$$

The two-electron integrals in the atomic basis are given as :

$$\langle\mu\nu|\sigma\lambda\rangle = \int\int \phi_\mu(1)\phi_\nu(2)\frac{1}{|r_1 - r_2|}\phi_\sigma(1)\phi_\lambda(2)d\vec{r_1}d\vec{r_2} \tag{1.29}$$

Where, the bra-ket notation has the electron indices $\langle 12|21\rangle$. They may also be written in an alternative order with both functions depending on electron 1 on the left, and the functions depending on electron 2 on the right ($\langle 11|22\rangle$). From these various semi empirical methods have been made using various approximations like limited orbital treatment and reduced coupling factor and so on. For example in the case of zero differential overlap (ZDO) method the overlap integrals is neglected. In the Neglect of Diatomic Differential Overlap (NDDO) method the overlap integral among different atoms have been treated as coulomb coupling. whereas in the case of Intermediate Neglect of Differential Overlap Approximation (INDO), two center integrals are omitted. The improved version of this method is known as *Zerner intermediate neglect of differential orbital* [ZINDO/S] method. The ZINDO/S method helps in predicting accurately $n- > \pi^*$ transition for various organic and inorganic molecules including main group elements and transition metal atoms [74].

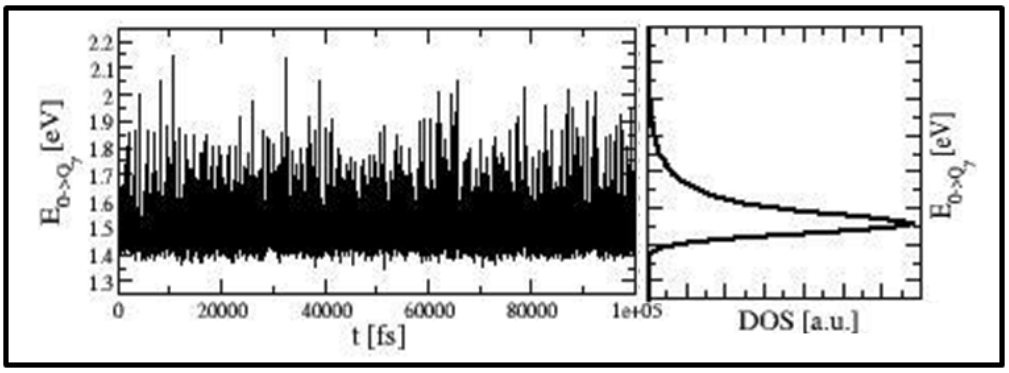

Figure 1.7: The figure shows the vertical excitation energy along the trajectory and in the right side the histogram of distribution of excitation energy is shown.

1.4 Quantum mechanics/Molecular mechanics (QM/MM)

The quantum mechanics/molecular mechanics (QM/MM) methods are gaining interest in predicting reaction mechanisms in bimolecular systems [75]. In principle, QM and MM methods are two different approaches employed for calculations and simulations on different scales [76]. For example, QM methods are employed for electronic calculations involving only hundred or less atoms based upon the theoretical level of calculations. On the other hand, molecular dynamics (MD) calculations nowadays have the capability to treat systems of several million atoms with the present computer power [52]. However, MD simulations have their own limitations, e.g., they do not involve electronic structure calculations or bond breaking or forming reactions. To overcome these drawbacks, the QM/MM approach has been developed by A. Warshel, M. Levitt [77] and M. Karplus [78] to join the advantages of both methods. This work has been recently awarded with the Noble Prize in Chemistry in 2013. The QM/MM approach is now a well established method for studying systems like enzymatic reaction kinetics [79], organo-metallic/inorganic [80] and solid state systems [81]. In our case, the pigment molecules were treated at the QM level while the protein, water and ions etc., at the MM level. An example schematic representation is given in Fig. 1.8.

In the present thesis, the main application of the QM/MM simulations is to model LH antennae pigments [82]. For this purpose, MD simulations are performed to sample conformations and l energies of the whole pigment protein complexes in order to obtain reasonable electronic properties (QM). During the QM calculations only the pigment coordinates are used for the electronic structure calculations by incorporating the MM influence as (fluctuating) point charges. Having said that, there are also reports of single point calculations on the crystal structure of the whole pigment protein complex using quantum calculation [83]. However the

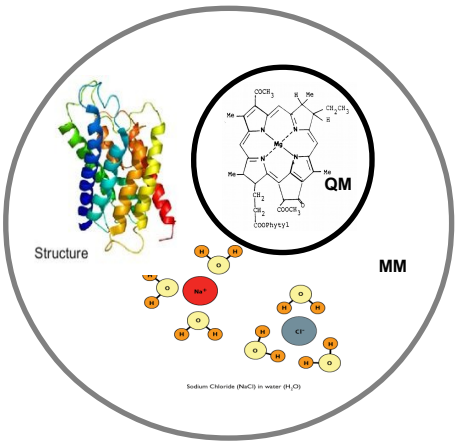

Figure 1.8: Schematic representation of a QM/MM partition is shown. The QM part is where the system of interest is selected for electronic structure calculation (in our case the chromophoric pigments), the rest of the system is included in the MM part (protein, water and ions etc.,).

results obtained from this calculations shows significant difference from various other quantum level of calculation. Therefore, by performing QM/MM calculations one can include the environmental electrostatics and thermal effect of the bath. From the QM/MM calculations excitation energies are obtained along the MD trajectory, leading to series of excitation energies. From these results, one can obtain the distribution of excitation energies or also called density of states (DOS). The detailed properties of the DOS curve shapes and their effects are discussed in detail in chapter 2 of the FF comparison.

1.5 Spectral density and Autocorrelation

For a full description of excitation energy transfer (EET) in LH complexes it is not enough to describe the interactions among the excitonic states. One need also to compute the LH pigment interactions with their environment. It is also known that the interaction between the system and the bath brings in disorder to the site energies fluctuation and which will also vary EET among LH pigments [84]. The experimental results of stokes shift (difference in energy between absorption and fluorescence spectra) can be used to calculate the magnitude of energy difference ('reorganization energy') among different pigments.

In the theory of open quantum systems, the spectral density is a key property to analyze the

system-bath coupling. The distribution of phonon frequencies in the environment and their coupling to the electronic transitions of the chromophores is characterized by the spectral density [84]. The spectral density is defined by the following expression [85]:

$$J(\omega) = \frac{\pi}{\hbar} \sum_{\xi} c_{\xi}^2 \delta(\omega - \omega_{\xi}) \ . \tag{1.30}$$

In this equation, the c_ξ denote the coupling strengths of the mode with frequency ω_ξ to the system. The spectral density is computed for each individual site because the site energies are obtained independently. The spectrum obtained can be compared to experimentally obtained fluorescence line narrowing spectra. To obtain the spectral density, one first needs to compute the energy autocorrelation of the respective system including the fluctuations caused by the environment. The autocorrelation is calculated using the following equation [85]:

$$C(t_i) = \frac{1}{N-i} \sum_{k=1}^{N-i} \langle \Delta E(t_i + t_k) \Delta E(t_k) \rangle \ . \tag{1.31}$$

Here, the relation between difference in fluctuation of energy gaps (ΔE) of various time steps i and k are correlated. The energy difference $\Delta E(t_i)$ is given by

$$\Delta E(t_i) = E(t_i) - \langle E \rangle \tag{1.32}$$

The auto-correlation function decays roughly double-exponentially [82, 86] and the obtained auto-correlation function can, for example, be fitted using a combination of exponential and cosine functions. The simplified form of the spectral density $J(\omega)$ with respect to the classical treatment of bath can be written as:

$$J(\omega) = \frac{\beta\omega}{\pi} \int_0^{\infty} \mathrm{d}t \, \mathrm{C}(t_i) \cos(\omega t) \tag{1.33}$$

1.6 Theory of open quantum systems

The closed system (S) or isolated system will not interact or exchange energy or matter with another system and it can be described by a normalized vector $|\psi\rangle$ as given below:

$$\langle A \rangle = \langle \psi | A | \psi \rangle \tag{1.34}$$

where, A is an hermitian operator $A = A^*$ and the evolution of the system is determined using Schrödinger equation as given below:

$$\frac{d}{dt}|\psi(t)\rangle = -\frac{i}{\hbar} H |\psi(t)\rangle \tag{1.35}$$

However in many cases the natural systems are always open and continuous, so limiting the system under particular wall of closed boundaries is not possible. For that purpose the theory of open quantum systems has been proposed. An open system is made out of two parts, a system S and an environment E. The boundary between S and E is arbitrary. The system (S) part is divided purely to do quantum calculation involving Schrödinger equation for the electronic sub-systems for a limited number of degrees of freedom to predict experimental properties of a molecule (e.g., infrared spectroscopy (IR), nuclear magnetic spectroscopy (NMR) and ultra-violet spectroscopy (UV), ...). Moreover, in some quantum calculations it is impossible to involve all environmental degrees of freedom or to involve all quantum levels in the calculation. Thus, by making some approximations or using a coarse-grained model of the system, various degree of freedom (DOF) can be treated implicitly leading to a smaller quantum system for which computations are feasible. This kind of calculations are widely applied in the case of biological or huge complex systems. For example, in the present case a wave packet dynamics approach is employed to calculate the population dynamics of the system using an Hamiltonian constructed from the vertical excitation energies of the LH pigment molecules on the diagonal and from the electronic couplings among the pigments in the off-diagonal elements.

Spectroscopic studies of light harvesting pigments [87, 88] revealed various types of absorption and emission transition energies. The transition energies of the individual pigments depend on the transition dipole moment of the molecule and its respective oscillatory strength. Usually, fluorescence excitation spectra are employed to compute the energy transfer efficiencies among various pigment molecules at room and/or cryogenic temperatures. The radiation less EET mechanism occurs among various LH pigments without fluorescence or emission. This transfer of energy occurs between various pigments using either the Förster or the Dexter energy transfer mechanisms (Fig. 1.9). The Förster energy transfer mechanism involves only energy transfer among the particles, i.e., when the excited donor (D^*) relaxes back to the ground state the emitted energy is transferred to the acceptor (A) molecule. Thus

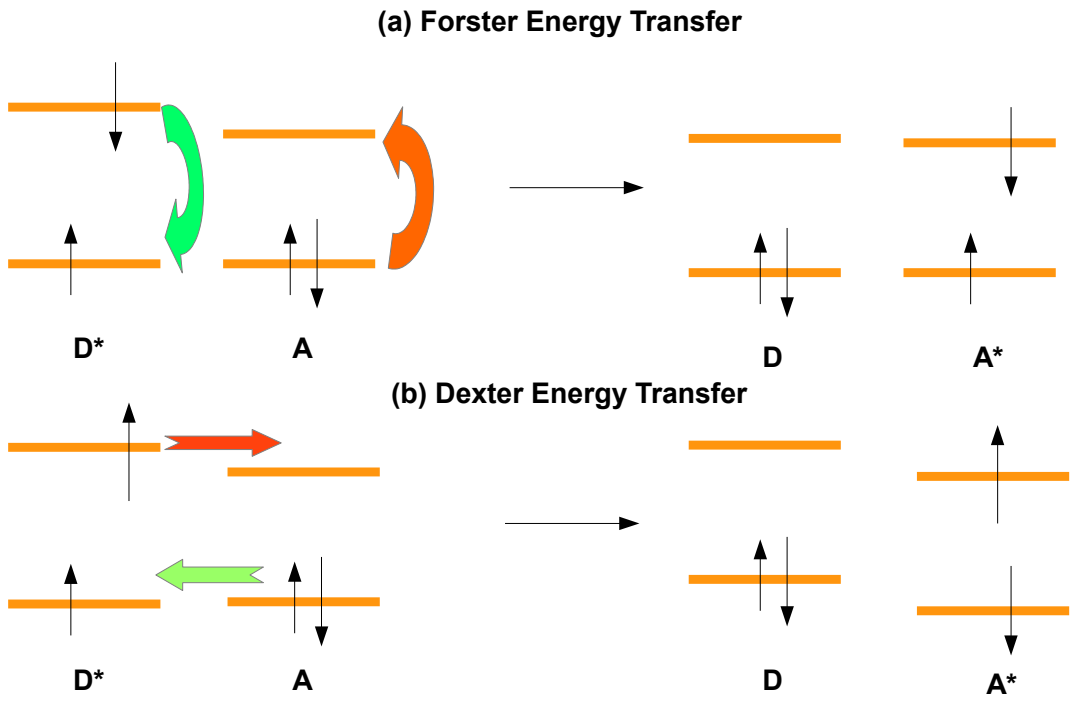

Figure 1.9: Schematic representation of Förster (a) and Dexter (b) energy transfer among donor and acceptor states is shown.

the acceptor molecule gets excited. In the case of Dexter energy transfer, the electron in the excited state is transfered to the excited state of the acceptor molecule and the ground state particle of A gets transferred to the D molecule. For the energy transfer to occur between the donor and acceptor molecules, they need to be close enough to each other. In Förster mechanism the energy transfer occurs through the Coulomb coupling which decreases with the sixth power of the distance between donor and acceptor. The theory of Förster energy transfer also assumes that the transfer rate from donor to acceptor is smaller than the vibrational relaxation rate. This ensures that once the energy is transferred to the acceptor, there is little chance of a backtransfer to the donor.

1.6.1 Ensemble-average wave-packet dynamics

2D spectroscopy studies showed long lived coherence in LH antenna complexes [2] of bacterial [24, 40] and plant systems [28]. Due to the limitation of experimental studies in predicting exciton transport at the molecular level, theoretical studies have been carried out. The transfer of excitons occurs among various pigments between occupied donor (D) and unoccupied acceptor (A) levels of molecules. Multiple transfer of excitons among various energy levels results in broad distributions of energy levels (absorption spectrum). The exciton dynamics among the pigments can be predicted by constructing the Hamiltonian of the system. The total Hamiltonian of the system can be written as:

$$H = H_S + H_R + H_{SR} \tag{1.36}$$

In this expression, H_S represents the system Hamiltonian and its bath counterpart H_R and H_{SR} describes the system-bath coupling. In this expression, the system Hamiltonian includes each individual sites. The system Hamiltonian can be further classified as:

$$H_S = \sum_m H_m^{(el)} + \sum_{m,n\ m\neq n} V_{mn} \tag{1.37}$$

Here, the Hamiltonian $H_m^{(el)}$ represents the subsystem Hamiltonian. The term V_{mn} represents the coupling term among the pigments and its co-ordinates. The electronic Hamiltonian $H_m^{(el)}$ of each individual molecule needs to be solved separately by quantum calculations such as HF, DFT or by semi-empirical methods to obtain the individual energy levels (ϵ_{ma}) of the molecule (Eq. 1.38)

$$H_m^{(el)}\phi_{ma}(\vec{r}_m, \vec{R}) = \epsilon_{ma}\phi_{ma}(\vec{r}_m, \vec{R}) \tag{1.38}$$

Here, $\vec{r}_m$ represents the pigment co-ordinates and $\vec{R}$ represents reservoir co-ordinates. The bath is assumed to consist of harmonic oscillators which can be described by their potential and kinetic energy operators as:

$$H_R = \sum_\epsilon \frac{\hat{p}_\xi^2}{2m_\xi} + \frac{m_\xi \omega_\xi^2 \hat{x}_\xi^2}{2} \tag{1.39}$$

In this expression, p_ξ and m_ξ are the momentum and mass of the harmonic oscillator of mode ξ. The x_ξ and ω_ξ are the displacements around the equilibrium position and the respective frequency. The system-bath coupling is considered as linear ($H_{SR} = \sum_{a\epsilon} \phi_a c_{a\epsilon} \hat{x}_\epsilon$) with $c_{a\epsilon}$ being the coupling strength. However, an additional approximation has been made in the ensemble-averaged wave packet dynamics. In this approximation the bath stays always in equilibrium and is not perturbed by the system (weak coupling approximation) [89]. Later this approximation is used in the Ehrenfest wave packet dynamics to solve the time-dependent Hamiltonian using the Schrödinger equation.

1.6.2 Excitonic Coupling methods

The off-diagonal elements of the excitonic Hamiltonian is described as coupling among the pigments. To determine the EET among the pigments one needs to compute the interaction or coupling strength between them. Based upon the coupling strength among the pigments, the distribution of exciton delocalization can be determined. The exciton distribution can exist in one pigment or over several pigments based upon the coupling between the pigments. The coupling can be computed using various methods, e.g., the point dipole approximation (PDA), extended dipole approximation (EDA) and Transition Electrostatic Potential charges (TrEsp) method. In my work i have used PDA and TrEsp methods for calculating the couplings among pigments.

Point Dipole Approximation (PDA)

The PDA-based excitonic coupling (V_{ij}^{PDA}) is computed by taking the individual transition dipole moments of each pigment. This method has been developed by Förster himself. Figure 1.10 shows a schematic representation of two molecular dipole vectors μ_i and μ_j separated by a distance R_{ij}. The PDA coupling can be written as:

$$V_{ij}^{PDA} = \mu_i \mu_j \frac{k}{R_{ij}^3} \ . \tag{1.40}$$

Here, k represents the relative orientation between the dipole ϕ_i and ϕ_j with respect to the planar angle γ and can be written in in terms of cosine functions as:

$$k = \cos\gamma - 3(\cos\phi_i . \cos\phi_j) \ . \tag{1.41}$$

The PDA method is widely used excitonic coupling method because it needs only the dipole moments of the respective molecules including their centers of mass as positions for the dipole moments. Previous reports have shown that the PDA [90] works well for larger distances between the pigments rather than for close chromophores. The values obtained by this method can be compared with linear dichroism studies of absorption experiments [91]. However, these results cannot give key information such as the nature of the transition and the center of symmetry for asymmetric molecules.

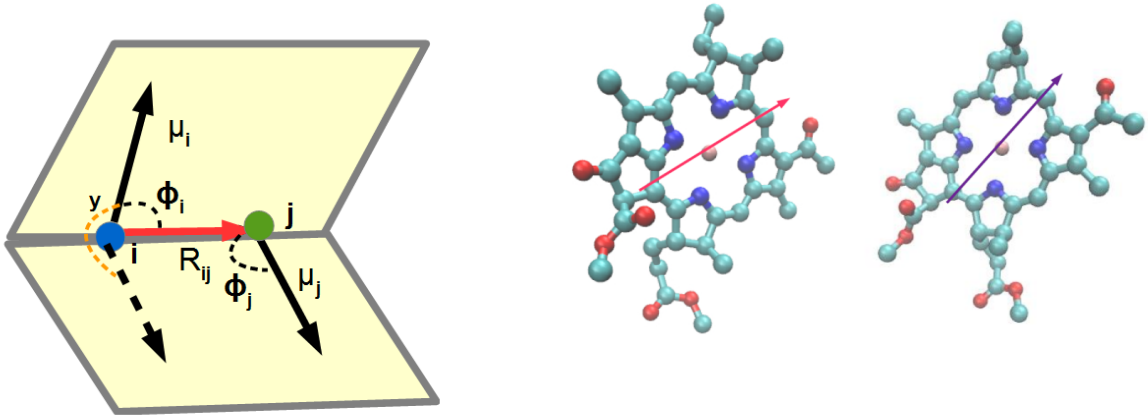

Figure 1.10: The left figure shows the schematic representation of simple point dipole vector at atoms i and j. The right figure shows the TrEsp calculated dipole vector for BChl a molecules.

Multipolar Approximation

The multipolar approximation is better than the previously mentioned dipolar approximations because the dipolar method accounts only for the transition dipoles rather than the transition density. So the Transition Electrostatic Potential charges (TrEsp) method involves obtaining Mulliken transition state charges for the whole molecule of interest similar to obtaining electrostatic charges for force fields. Within this TrEsp approach, charges are obtained using the Coulomb coupling method as stated below:

$$V_{mn}^{TrESP} = \frac{f}{4\pi\epsilon_o} \sum_{i\in m} \sum_{j\in n} \frac{q_i q_j}{|R_i - R_j|} \ . \tag{1.42}$$

Here q_m and q_n are the transition charges of the fitted transition density for pigments m and n, respectively. Based upon the quantum chemistry method and basis set employed, the transition state charges may differ. Sometimes scaling of the charges will be needed to match the experimental dipole moment. Since the quantum calculations are primarily done for vacuum state, a screening factor f will be employed to account for solvent effects. A detailed analysis of various screening methods and the effect on coupling is reported elsewhere [92].

Outlook of Results and Discussion

The results obtained from the different research projects during my PhD are presented in detail below. All research projects involve studies on EET in LH pigment-protein complexes. One project is focused on the comparison of FF quantum chemistry methods as well as a new CGenFF development of the BChl a pigment present in the FMO complex. The other project is on the phycoerythrin PE555 LH complex which includes bilin molecules as chromophores. Given below is the order of results and discussion of the above mentioned projects in detail:

Chapter 2: *Influence of Force Fields and Quantum Chemistry Approach on Spectral Densities of BChl a in Solution and in FMO complex.*

In this study the EET among BChl a pigments present in the FMO complex is studied in detail. A QM/MM method is used to construct the excitonic Hamiltonian for the whole complex. In a first step the EET between two different FMO complex extracted from *Prosthecochloris aestuarii* and *Chlorobaculum tepidum* bacterium is compared. This comparison was performed using two different existing FF (CHARMM and AMBER) in combination with either the ZINDO/S-CIS approach or the TDDFT quantum method on the B3LYP/3-21G level. Subsequently, the spectral densities are determined which are key quantities for reduced density matrix approaches. Moreover, the population transfer among different BChl a pigments present in the FMO complex is studied using ensemble-averaged wave packet dynamics.

Chapter 3: *A CHARMM General force field for Bacteriochlorophyll* a *and its application to the FMO Protein Complex.*

In this chapter a new CHARMM General force field (CGenFF) parameterization is determined and test simulations are performed for single BChl a in solution and for the whole FMO complex. The new FF parameterization has been carried out following as closely as possible the CGenFF procedure while the previously existing CHARMM FF was determined in a way not following the CHARMM procedure too closely. For example, the partial charges were now fitted using the interaction energies of the BChl a molecule with TIP3P water molecules. The bond and angle fitting was done using a MM Hessian calculation. Furthermore, the dihedral angles were fitted for each individual QM twisting angle. In a further step, a spectral density analysis was performed for an individual BChl a in solution and for the FMO complex.

Chapter 4: *Protein Arrangement effects the Exciton Dynamics in the PE555 Complex*

The subsequent chapter focuses on a QM/MM study of the PE555 complex. The PE555 complex has PEB and DBV LH pigments similar to the PE545 complex. The spectral density results are computed and compared between the PE555 and the PE545 complexes. Moreover, the population transfer among the different pigments has been studied in detail with a special emphasis on two different ways of calculating the excitonic coupling, i.e., the PDA and TrEsp coupling methods.

Appendix *Supplementary Information: Protein Arrangement effects the Exciton Dynamics in the PE555 Complex*

This appendix contains the computed TrEsp charges for the PEB and DBV pigments. Moreover, the PE545 PDA coupling and PE555 TrEsp couplings are reported. In additon, the averaged spectral densities of the PE555 and the PE545 complexes are compared to an experimental one for the PE545 complex.

Chapter 2

Influence of Force Fields and Quantum Chemistry Approach on Spectral Densities of BChl *a* in Solution and in FMO Proteins [1,2]

[1]Adapted with permission from the article by Suryanarayanan Chandrasekaran, Mortaza Aghtar, Stphanie Valleau, Aln Aspuru-Guzik, Ulrich Kleinekathöfer "Influence of Force Fields and Quantum Chemistry Approach on Spectral Densities of BChl *a* in Solution and in FMO Proteins" *J. Phys. Chem. B* **2015**, 119, pp 9995–10004. **DOI**: 10.1021/acs.jpcb.5b03654. Copyright © 2015 American Chemical Society.

[2]My contribution to this paper includes the MD simulations and QM calculations along the trajectories for various force fields, obtaining the site energies and couplings and subsequently calculating the density of states and spectral densities. Moreover, I participated in preparing the manuscript.

Abstract

Studies on light-harvesting (LH) systems have attracted much attention after the finding of long-lived quantum coherences in the exciton dynamics of the Fenna-Matthews-Olson (FMO) complex. In this complex, excitation energy transfer occurs between the bacteriochlorophyll *a* (BChl *a*) pigments. Two QM/MM studies, each with a different force-field and quantum chemistry approach, reported different excitation energy distributions for the FMO complex. To understand the reasons for these differences in the predicted excitation energies, we have carried out a comparative study between the simulations using the CHARMM and AMBER force field and the ZINDO/S and TDDFT quantum chemistry methods. The calculations using the CHARMM force field together with ZINDO/S or TDDFT always show a wider spread in the energy distribution compared to those using the AMBER force field. High- or low-energy tails in these energy distributions result in larger values for the spectral density at low frequencies. A detailed study on individual BChl *a* molecules in solution shows that without the environment, the density of states is the same for both force field sets. Including the environmental point charges, however, the excitation energy distribution gets broader and, depending on the applied methods, also asymmetric. The excitation energy distribution predicted using TDDFT together with the AMBER force field shows a symmetric, Gaussian-like distribution.

2.1 Introduction

Photosynthesis is a physio-chemical process by which plants and bacteria use light energy for the synthesis of organic compounds. These photosynthetic processes begin with the absorption of light by the so-called light-harvesting (LH) complexes embedded in and around the photosynthetic membrane, followed by the transfer of the absorbed energy to the reaction center. At the reaction center, the ionization process takes place leading to further chemical processes. [2] The LH complexes are aggregates of proteins and chromophoric pigments designed by nature to funnel sunlight efficiently towards the reaction centers. In recent years, the study of light-harvesting and associated complexes has attracted much interest because of the experimental finding of long-lived quantum coherences in the exciton dynamics. [28, 30, 93] These dynamic quantum effects are in addition to the so-called static quantum effects which already increase the rate of photon absorption and energy conversion. [94] There are also various other aspects such as noise assisted excitation energy transfer [95] which make

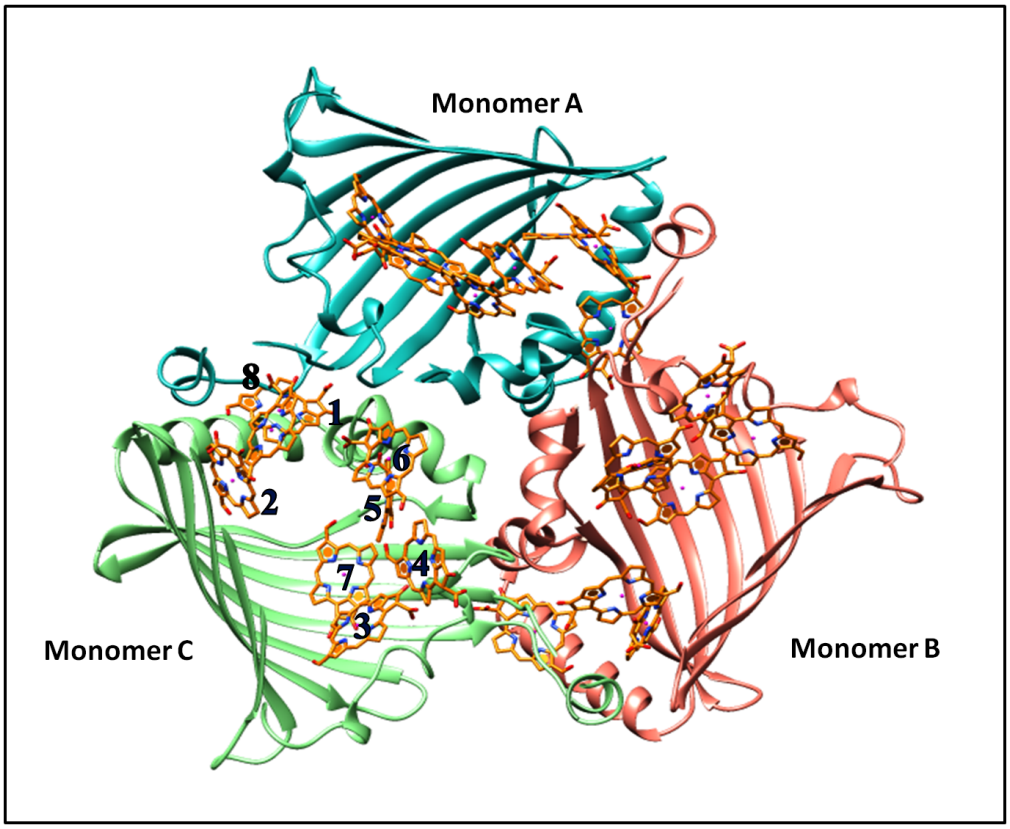

Figure 2.1: Structure of the FMO trimer with pigments (orange) and proteins differently colored. The protein scaffold in the front has been removed to obtain an enhanced view of BChl *a* pigment units. The figure shows FMO from *C. tepidum* though in this representation the one from *P. aestuarii* is almost indistinguishable.

LH complexes interesting objects of study. Understanding the underlying physics of efficient exciton transport inspires scientists and engineers to devise the design principles for artificial solar systems, for instance, with the goal of minimizing exciton trapping: one of the problems of artificial LH systems.[96]

In Fig. 1 we show the crystal structure of the Fenna-Matthews-Olson complex (FMO) from *Chlorobaculum tepidum* (pdb code 3ENI) [97] bacterium, one of the most extensively studied pigment-protein complexes (see, e.g., Refs. 31, 86, 98–105). In addition to the crystal structure for FMO from *Chlorobaculum tepidum* also the one from the bacterium *Prosthecochloris aestuarii* (pdb code 3EOJ) [97] is available. With these crystal structures one can carry out all-atom molecular dynamics (MD) simulations of these systems. Classical molecular dynamics are, however, alone not sufficient to describe excitation energy transfer and spectra. On the other hand, quantum chemistry calculations for this kind of complexes are still very expensive especially if one wants to combine them with time-dependent cal-

culations [106]. Therefore, a sequential coupling of MD calculations, QM/MM (quantum mechanics/molecular mechanics) and quantum dynamical simulations has been proposed [107]. One of the key properties being calculated in this and similar schemes is the spectral density which determines the frequency-dependent coupling between relevant system degrees of freedom and thermal bath modes. For the FMO complex, spectral densities have been determined using such a theoretical scheme by the two groups authoring this study [104, 108] and later refined [99, 109]. The differences between the results of the two groups triggered this study with the goal of understanding whether the differences originated from the force fields or the quantum chemical approaches. Later on, more studies on the FMO system in the same or a similar spirit followed [110–112]. The LH systems which have been treated in a combined molecular based quantum-classical approach include LH2 [107], photosystem II [113], and PE545 [98, 114, 115]. The limits and potentials of these QM/MM models in describing light-harvesting systems have recently been discussed [116].

BChl *a* molecules have been parametrized for different force fields sets including CHARMM [107], AMBER [117] and OPLS [118]. For these parameterizations different procedures and underlying philosophies have been used. For the partial charges, for example, in AMBER one fits the electrostatic potential (RESP) while for CHARMM the partial charges are obtained by fitting interaction energies with nearby water molecules. It is *a priori* not clear which force field set will yield more accurate results for the problem at hand, i.e., the calculation of spectral densities of LH systems. For the FMO complex, one study used the CHARMM force field [99, 104] and the other one, which we want to compare to, employed the AMBER force field [108, 109].

The other major methodological difference is the approach used for the calculation of the vertical excitation energies of the individual BChl *a* molecules along the MD trajectory. In one of the studies [99, 104] the vertical excitation energies were determined using the semi-empirical ZINDO/S-CIS approach (Zerner Intermediate Neglect of Differential Orbital method with parameters for spectroscopic properties together with the configuration interaction scheme using single excitations only). The advantages and limitations of this approach have been discussed earlier [86, 119, 120]. The other quantum-classical scheme for FMO which we would like to compare employed the TDDFT approach at the BLYP-3-21G level [108, 109]. Computationally this is much more expensive than the ZINDO/S-CIS calculations but again, it is *a priori* not clear which of the methods yields more accurate results. In a recent study by List et al.[100] the accurate DFT/MRCI scheme was used as a benchmark and ZINDO/S-CIS as well as various TDDFT variants were compared for an FMO crystal structure. In this comparison TDDFT with the B3LYP but also with the BLYP functionals

performed more accurately than the ZINDO/S-CIS calculations. The latter showed a particularly large deviation for one of the pigments. The TDDFT-BLYP and B3LYP schemes underestimated the environmental shifts while ZINDO overestimated them. The TDDFT calculations together with the CAM-B3LYP functional deviated more from the DFT/MRCI results than the B3LYP findings. In another investigation [121] for BChl *a* molecules in different solutions the CAM-B3LYP performed best compared to experiments leaving some open questions. Moreover, in an earlier study [122] on absorption shifts for retinal proteins it was shown that INDO/S calculations produced more reliable shifts than TDDFT approaches.

For the present problem of spectral densities of the FMO complex, we need to investigate whether the force field sets or the quantum chemistry approaches mainly lead to the differences in the spectral densities for the FMO complex in Refs. 99, 109, 123. To this end, this contribution starts with a brief description of the FMO results and a discussion of their differences. To perform a more detailed analysis, we will then limit ourselves to a subset of the system, i.e., we will study a single BChl *a* molecule in water in detail. These results will finally be used to explain the differences in the spectral densities for the FMO complex.

2.2 Exciton dynamics Hamiltonian and spectral density formalism

Due to the large system size (more than 50.000 atoms when including solvent) it is still unfeasible to determine the dynamics in the FMO complex fully quantum mechanically. In the model often employed, each pigment is described as a two-level system interacting with a thermal bosonic bath. The bath represents the environment of the pigment and includes all degrees of freedom, which are not explicitly in the two-level pigment. The energy gaps in the two-level systems correspond to the vertical excitation energies between ground and Q_y state of the individual pigments. The obtained excitation energy can be employed to obtain a time-dependent Hamiltonian and this can be combined with ensemble-averaged wave packet dynamics or density matrices to determine the population transfer or optical properties [89]. The fluctuations in the energy gaps result from the thermal variations of the molecular conformations during the MD simulation. Therefore, the results obtained certainly depend on the force field chosen and on the employed quantum chemistry approach to determine the vertical excitation energies.

The system-bath approaches always assume that the total Hamiltonian H

$$H = H_S + H_B + H_{SB} \ , \tag{2.1}$$

is partitioned into a system part H_S, a bath part H_B and a coupling part H_{SB} denoting the coupling between system and bath. The system Hamiltonian, H_S, is given by the coupled two-level systems which represent the interacting pigments. The bath Hamiltonian, H_B is given by an infinite set of harmonic oscillators. The system-bath H_{SB} expression is assumed to be of the form

$$H_{SB} = \sum_j K_j \Phi_j = \sum_j K_j \sum_\xi c_{j\xi} x_\xi \ . \tag{2.2}$$

In this expression K_j represents the system operator and Φ_j represents the system-bath coupling operator for pigment j. The latter one is assumed to be linear in the bath modes each with a respective coupling constants $c_{j\xi}$. The coupling constants $c_{j\xi}$ furthermore appear in the expression of spectral density J_j of pigment j as weighting factors

$$J_j(\omega) = \frac{1}{2} \sum_\xi \frac{c_{j\xi}^2}{m_\xi \omega_\xi} \delta(\omega - \omega_\xi) \ . \tag{2.3}$$

Here m_ξ denotes the mass of the bath oscillator with frequency ω_ξ. The spectral density in the Caldeira-Legett model $J_{CL,j}(\omega)$ is connected to this definition by $J_{CL,j}(\omega) = \pi/\hbar J_j(\omega)$. The spectral density $J_j(\omega)$ of BChl j can be rewritten with respect to the energy gap auto-correlation function $C_j(t)$ as

$$J_j(\omega) = \frac{\beta\omega}{\pi} \int_0^\infty dt C_j(t) cos(\omega t) \ . \tag{2.4}$$

The energy gap correlation function can be determined using the energy gaps $\Delta E_i(t_i)$ at time steps t_i using the expression

$$C_j(t_k) = \frac{1}{N-k} \sum_{l=1}^{N-k} \Delta E_j(t_k + t_l) \Delta E_j(t_l) \ . \tag{2.5}$$

In this equation the number of time points is denoted by N. Below some details will be given on how the energy gaps $\Delta E_j(t_l)$ can be determined. The connection between this type of open quantum system description of the exciton dynamics and the QM/MM approach used to extract a spectral density has been discussed in detail in our previous publications [107, 109, 120].

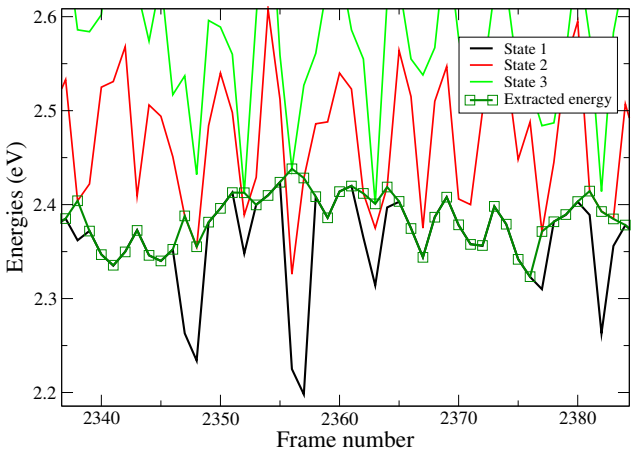

Figure 2.2: Part of the energy trajectory from the TDDFT-B3LYP calculations showing the first three excited states together with the extracted Q_y state.

2.3 Computational details

High resolution crystal structures are available for the FMO complexes of the green sulphur bacteria of *Prosthecochloris aestuarii* (pdb code 3EOJ) [97] and *Chlorobaculum tepidum* (pdb code 3ENI) [97] at 1.30 Å and 2.20 Å resolution, respectively. We would like to stress that the results for *C. tepidum* obtained using the CHARMM force field together with the ZINDO/S-CIS quantum chemistry approach have been reported earlier [99, 104]. Moreover, results for the FMO complex of *P. aestuarii* performed using the AMBER force field and the TDDFT (BLYP/3-21G) method have been published earlier [108, 109]. However, these calculations were performed on a FMO monomer. To get consistent setups for a comparison, we redid all four combinations of force fields, CHARMM or AMBER, and electronic structure theories, ZINDO/S-CIS and TDDFT, for the same trimer starting structure, i.e., the one from *P. aestuarii*. The TDDFT calculations were performed with the B3LYP instead of the BLYP functional which often yields improved results. The 3-21G basis was used as in the earlier BLYP calculations for the monomer. Surprisingly the TDDFT-BLYP results for the monomer are quite similar to those of the trimer and the B3LYP functional (see Fig. 2.3). All discussions below refer to the TDDFT-B3LYP calculations unless otherwise stated.

The whole FMO trimer complex of *P. aestuarii* including protein, pigments and ions (19914 atoms) were simulated in a TIP3P water box of size 123 × 123 × 102 Å^3 containing 143,118 atoms. The CHARMM22 and AMBER99SB force fields were employed for the proteins while for the BChl *a* we employed the force fields for AMBER and CHARMM previously reported by Ceccarelli et al.[117] and by Damjanović et al.[107]. All the system setup was carried out using the VMD software[124] and the molecular dynamics simulations using

the NAMD package[125] with a fixed time step of 1 fs and SHAKE constraints for all atoms. The systems were initially equilibrated for 20 ns and during the production run the complete system was stored every 5 fs for 300 ps leading to 60.000 snapshots. These snapshots were all used for the ZINDO/S-CIS calculations, while for the TDDFT calculations only the first 3300 frames have been selected to reduce the computational cost. Both, the ZINDO/S-CIS and the TDDFT calculations were performed using the ORCA 3.0 package [126]. During the course of the molecular dynamics simulations, periodic boundary condition are maintained, but in the case of the quantum calculations, the coordinates are extracted with respect to a single simulation box setup and then the excitation energies are computed individually for each pigment. During the quantum calculations the respective BChl *a* molecule was always positioned at the center of the first period image of the MD simulation setup and the rest of the atoms were treated as point charges. The Q_y state is extracted based on the angle between the corresponding transition dipole from the quantum calculation and the direction of two specific nitrogen atoms from the MD trajectory [107]. Moreover, it is checked that this state has the largest oscillator strength among the TDDFT excited states also to discriminate from artificial states. A piece of the resulting energy trajectory is shown in Fig. 2.2.

As test systems individual BChl *a* molecules in water have also been simulated. Different cubic simulation box sizes between 10 Å and 25 Å have been studied in connection with the TIP3P [127] and TIP4P [128] water models and the CHARMM as well as AMBER force fields. The system was initially equilibrated for 10 ns and then production runs were carried out for 100 ps by recording the atomic positions every 1 fs. Subsequently, the excitation energies were determined for 100,000 snapshots at the ZINDO/S-CIS level with an active space of the 10 highest occupied and the 10 lowest unoccupied states. Due to the higher computational cost of the TDDFT B3LYP/3-21g calculations, only 3500 snapshots were computed for this approach. In all the QM/MM calculation detailed above, the quantum system was restricted to a truncated structure of the BChl molecule. Each terminal CH_3 and CH_2CH_3 group as well as the phytyl tails were replaced by hydrogen atoms. This approximation has been tested in detail earlier [119, 129, 130]. Moreover, in the present study we enlarged the QM region by including more and more surrounding water molecules. In this investigation all the atoms in the surrounding 4 Å are included and also the part of the tail in this region is included. To avoid problems with water molecules changing positions during the MD simulation, we constrained the water molecules inside the 4 Å region by putting a harmonic position constraint on the corresponding oxygen atoms. We need to mention, however, that increasing the QM region caused increasing problems with the convergence of the ZINDO/S-CIS calculations. When including 55 surrounding water molecules only about 2/3 of the 12,500 frames which were investigated showed converged energies. Since we were

only interested in the distribution of energy levels and not the spectral densities for these setups, the number of converged energies were still more than necessary to obtain accurate average energies.

Concerning the exciton dynamics described below, the results were obtained by stochastic integration of the time-dependent Hamiltonian with 5000 averages[108]. For simplicity the couplings were assumed to be constant. The values were taken from Ref. 99. The first 10000 steps of the energy gap trajectories from ZINDO were taken for the Hamiltonian with a 5 fs time step. The dynamics was carried out with the excitation starting in site 1 (Site 360 in 3EOJ) for 1250 fs.

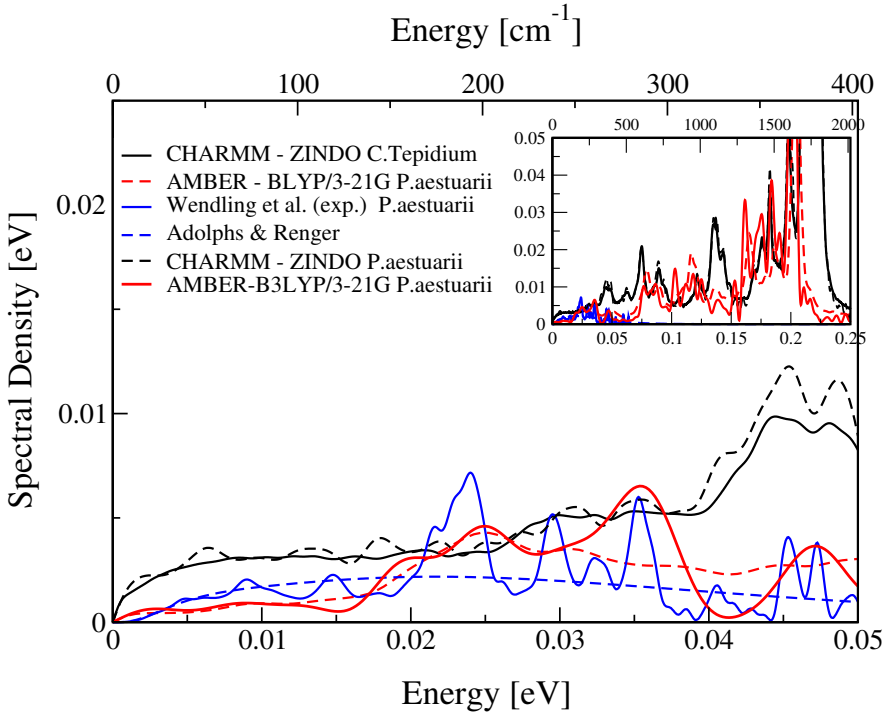

Figure 2.3: Comparison of previous results for the spectral density of FMO using CHARMM together with ZINDO [99], using AMBER together with TDDFT-BLYP [109], the experimental results by Wendling et al. [131] with results for FMO from *P. aestuarii* using CHARMM together with ZINDO and using AMBER together with TDDFT-B3LYP. The inset shows a larger frequency range.

2.4 Comparison of spectral densities for FMO

The aim of this study is to enhance the understanding of the differences in the spectral densities for the FMO complex published in Refs. 109 and 99. To simplify the comparison, here,

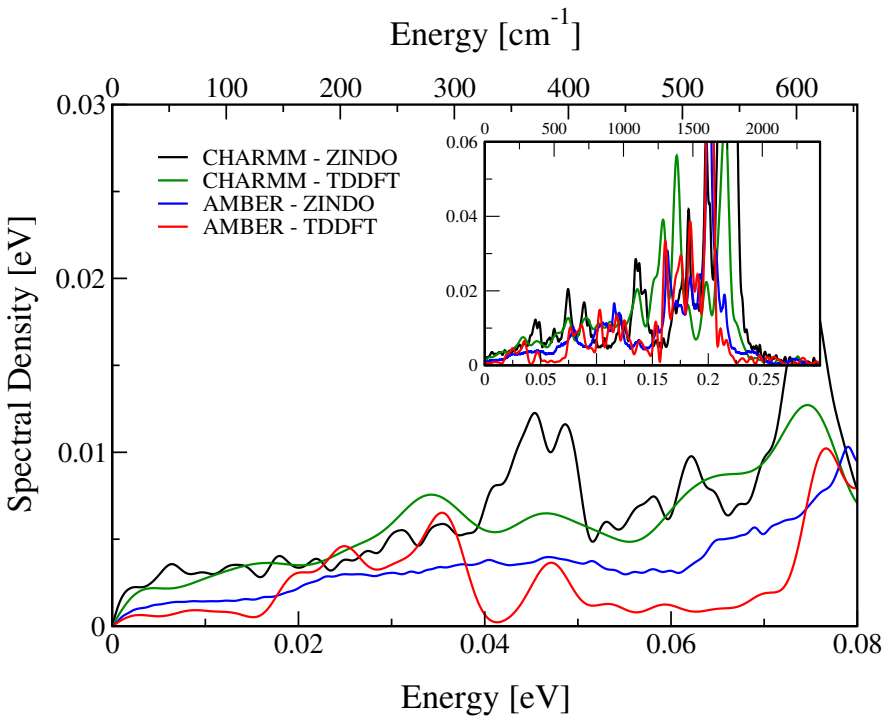

Figure 2.4: Spectral densities for FMO of *P. aestuarii* in the different combinations of CHARMM and AMBER force fields together with ZINDO/S-CIS and TDDFT-B3LYP for the vertical excitation energies.

we focus on a single spectral density, the average of the individual site spectral densities. The previously obtained results [99, 109] are shown in Fig. 2.3 together with an experimental spectral density based on a fluorescence line narrowing spectrum of FMO published by Wendling *et al.* [131]. For the later spectral density an estimated Huang-Rhys factor of 0.5 [132] was combined with the functional form based on the original experimental data [131]. As stressed previously, the two theoretical spectral densities which we are investigating, have been obtained for two different species of bacteria: *C. tepidum* and *P. aestuarii*. Therefore, the simulations with the CHARMM force field together with ZINDO/S-CIS excitation energies have been repeated for *P. aestuarii* to rule out any possible differences due to the varying bacterium. The results for this variant are shown in Fig. 2.3 as well. Clearly the effect of the bacterial species is very small. It is reassuring to see that these two independent setups yield similar results, indicating the stability of the approach under small variations. We would like to point out that such a calculation has previously been reported by Gao et al.[111] based on the same scheme which we originally applied to *C. tepidum*. Therefore, we refrain from any further detailed analysis here. All simulations and discussions below will be on FMO from *P. aestuarii*.

Two additional simulations using the AMBER force field together with ZINDO/S-CIS

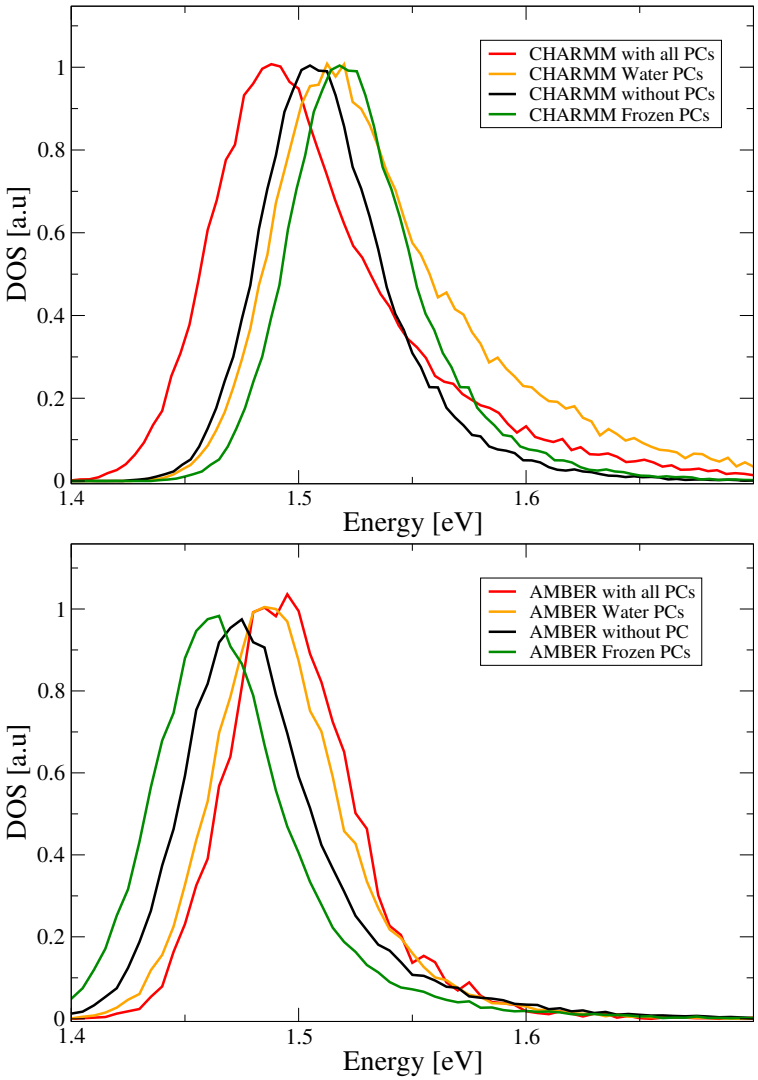

Figure 2.5: Distribution of energy gaps for different selections of external point charges for BChl 1 of the FMO complex.

and the CHARMM force field together with TDDFT (B3LYP/3-21G) were performed to be able to analyze the effect of the different theoretical approaches. From Fig. 2.4 it is evident that the AMBER force field in the low frequency regime are always lower than those using the CHARMM force field. At the same time there are also clear variations with the approach employed for determining the vertical excitation energies though these seem smaller than the force field effects.

To better understand the distribution of energy levels, also known as distribution of states (DOS), we plotted this quantity for the ZINDO/S-CIS calculations in Fig. 2.5. It can be seem that the CHARMM DOS using all environmental PCs is broader than the results for the AMBER force fields. Performing the QM calculations without coupling to the MM

charges (without PCs), the findings for the two force fields are very similar and show rather symmetric distributions which are shifted with respect to each other. This shift is induced by the slightly different average conformations obtained when using the two different force fields (data not shown). It is surprising to see that including the effect of a "frozen" environment, i.e., keeping the PCs from the first frame for all subsequent frames while changing the pigment conformations, leads to shifts with opposite signs for the two different force fields. For the AMBER force fields, including only the PCs of the water molecules, i.e., excluding the effects of the protein and other pigments, leads to similar results to those of the full QM/MM calculations. Surprisingly this is not the case for the CHARMM force field.

Given the complexity of the FMO trimer with its 24 pigments and the fact that TDDFT calculations for the whole complex are computational quite expensive, we decided to perform more elaborate studies on a reduced system. To this end, we removed the protein and simulated a single BChl *a* molecule in solution. To avoid the introduction of any further differences between this reduced model and the complete system, we kept water as solvent though BChl *a* is not experimentally solvable. However, this will not influence the conclusion made on the theoretical approach performed in this investigation.

2.5 Single BChl *a* in solution

The DOS for different simulation setups containing a single BChl *a* molecule in a water box is shown in Fig. 2.6. At first we tested the size of the water box and already got the first interesting finding. At this point it is important to realize that in the classical MD simulation, full periodic boundary conditions are used. This periodicity is also used when moving the pigment into the center of the primary box. Then in the QM/MM step only the MM charges from the water in this primary box are taken into account. This procedure leads to visible box size effects when going from a cubic length of 10 Å to 20 Å but not for larger box side lengths. The surprising point here is that this effect is much larger for the AMBER than for the CHARMM force field as shown in Fig. 2.6. So larger boxes are needed for the AMBER simulations to obtain converged DOS results. Some variations are also visible when using the 4-site TIP4P models instead of the 3-site TIP3P water model though they are not very large (data not shown).

Neglecting the electrostatic QM/MM modeling while determining the vertical excitation energies, i.e., not taking the water into account at all during this quantum chemistry step, leads to quite symmetric Gaussian-like distributions. These DOS are the same independent

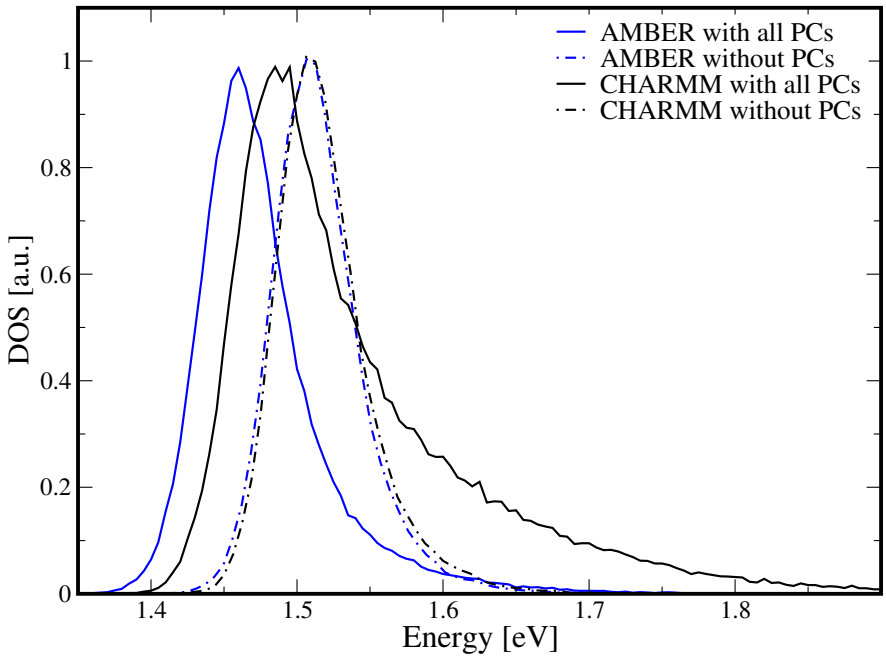

Figure 2.6: Comparison of the density of states (DOS) based on ZINDO/S-CIS for AMBER and CHARMM force fields for an individual solvated BChl *a* molecule.

of the water model employed during the MD step. The results without external point charges also show a shift with respect to the previously described simulations. So the distributions of the energy gaps are not only broadened by the environmental coupling but also shifted in energy as to be expected.

In a recent study by Martin et al. [133] concerning the green fluorescent protein (GFP) the low frequency motion of interfacial water molecules close to the protein were shown to be responsible for the non-Gaussian asymmetric distributions of the electronic states. In the case of an individual BChl *a* molecule in solution, we have shown that the asymmetry is not only dependent on the electrostatic interaction of the molecules near to it. The asymmetry also depends significantly on the long-range electrostatic interaction between pigment and environment as can be seen by the variations in the water box size.

In Fig. 2.7 we show the spectral densities corresponding to the energy gap distributions discussed in Fig. 2.6. There are clear differences between each spectral density. For all simulations including water point charges, the CHARMM spectral densities are larger than those obtained using the AMBER force field. More interestingly, there is a clear correlation between the width and/or asymmetry of the DOS and the amplitudes of the spectral densities. Both quantities are of course based on the same energy gap trajectories. The DOS only yields information on the abundance of certain gap energies, while the spectral densities contain

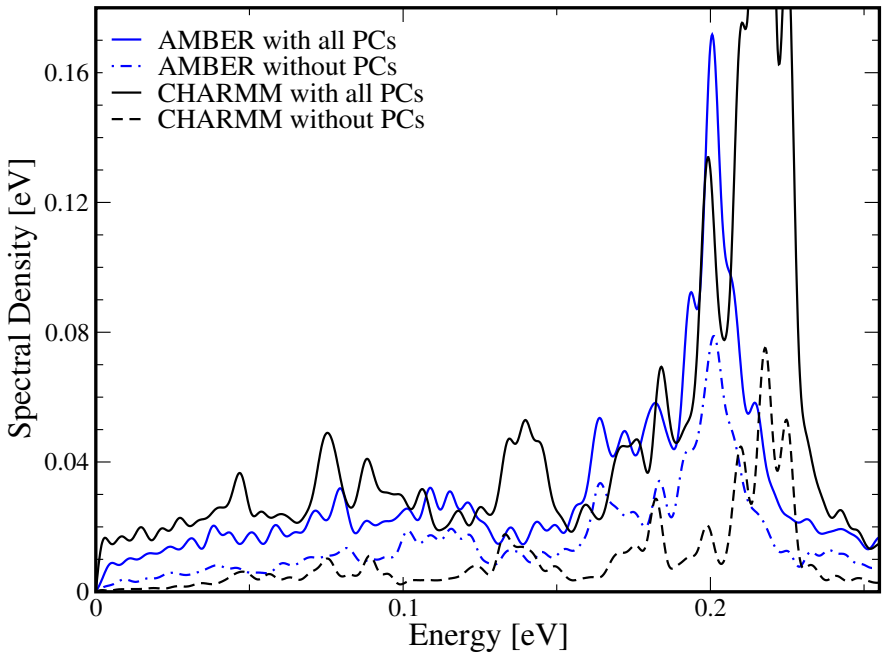

Figure 2.7: Spectral densities for the same simulations as shown in Fig. 2.6.

(indirect) information on their temporal order. Assuming that the noise fluctuations causing the energy gap fluctuations are well behaved, i.e., do not show pathological cases, one can deduce that energy gaps with a low abundance for example represented in the far wings of the DOS are directly related to low-frequency events. In other words, oscillations with low frequencies but large amplitudes lead to the long tails in the DOS and are, of course, visible in the low frequency parts of the spectral densities. The CHARMM simulation leads to the most asymmetric DOS with a long high-energy tail. Therefore, this simulation also results in a spectral density with the largest values at low frequencies. This direct correspondence between DOS and spectral densities and their relative order are consistent for all results displayed in Figs. 2.6 and 2.7.

Employing the AMBER force field, the differences between spectral densities belonging to the various setups are much smaller than those for the CHARMM force field. For the latter force field also the absolute values for the spectral densities in the region between 0.2 and 0.25 eV are much larger.

So far all simulations for the single BChl *a* molecule in water were based on ZINDO/S-CIS vertical transition energies. As we have shown, the DOS obtained without taking the environment point charges into account are almost identical, i.e., similar pigment conformations are sampled by the two force fields. The effect of the differences between pigment force fields becomes significantly visible only when the electrostatic QM/MM coupling is

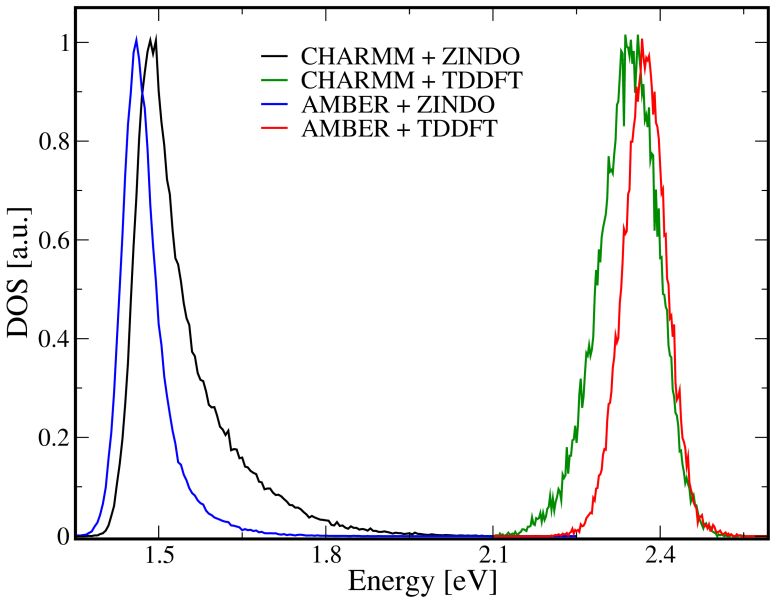

Figure 2.8: Density of states for a single BChl *a* using water box size of 20 Å and the TIP3P water model for the two investigated force field and quantum chemistry approaches.

considered (N.B. the MM charges of the BChl *a* molecule are not included in this part of the calculation). The charges of the different BChl *a* force fields lead to dissimilar oriental polarizations of the surrounding water molecules in turn leading to unlike DOS and spectral densities. We also find that the average equilibrium geometry of the BChl is different in the case of each force-field.

To better understand the differences between the two sets of force fields, we list in Table 2.1 the partial charges for some of the prominent atoms in the BChl *a* molecule. These partial charges are of key importance for the environmental coupling between molecule and protein as well as water since it is given by the electrostatic coupling. On looking at the charges one can see that central magnesium atom is drastically low in the case AMBER and also out of four nitrogens of bacteriochlorin macrocyle only one nitrogen is negatively charged. Also on average the partial charges of the CHARMM force field are larger in magnitude than those of the AMBER one. The sum of the squares of the partial charges is 14.4 for CHARMM and 6.1 for AMBER. This can, at least to some extent, explain why the spectral densities determined using the CHARMM force field are on average larger than those determined using the AMBER force field.

In addition to the ZINDO/S-CIS results for the CHARMM and AMBER force fields, Fig. 2.8 displays the findings for vertical excitation energies based on TDDFT calculations.

Table 2.1: Partial charges of some atoms belonging to the BChl *a* atoms for the two different force fields under consideration. The naming of the atoms is the same as in the respective pdb files.

Atom name	**CHARMM**	**AMBER**
MG	1.02	0.13
NA	-0.33	0.04
NB	-0.72	-0.06
NC	-0.28	0.07
ND	-0.50	0.07
C1A	-0.28	-0.12
CHA	0.46	0.07
C4D	0.02	-0.13
C1B	0.48	-0.03
CHB	-0.71	-0.22
C4A	0.39	-0.04
C1C	0.23	-0.09
CHC	-0.65	-0.27
C4B	0.55	0.20
C1D	0.17	-0.05
CHD	-0.28	-0.26
C4C	-0.13	-0.06
C2A	-0.31	0.09
CAA	0.09	-0.06
C3A	0.49	0.26
CMA	-0.54	-0.28
C2B	0.11	0.20
CMB	-0.19	-0.24

One can clearly see the well-known fact that TDDFT calculations overestimate the energy gap. For the present study, this shift in all excitation energies is of little interest since we are mainly concerned with the gap fluctuations. Interestingly however, the asymmetric tail of the TDDFT distributions is to lower rather than to higher energies as in the case of the ZINDO/S-CIS calculations. For both electronic structure theories the distributions are significantly narrower and less asymmetric in the case of the AMBER rather than the CHARMM force field.

As before, when comparing the ZINDO/S-CIS and TDDFT approaches, there is a direct connection between width/asymmetry of DOS and amplitude of the spectral densities (see Fig. 2.9). The simulation with the largest tail, i.e., CHARMM force field with ZINDO/S-CIS excitation energy calculations, yields the largest spectral densities at low frequencies. The

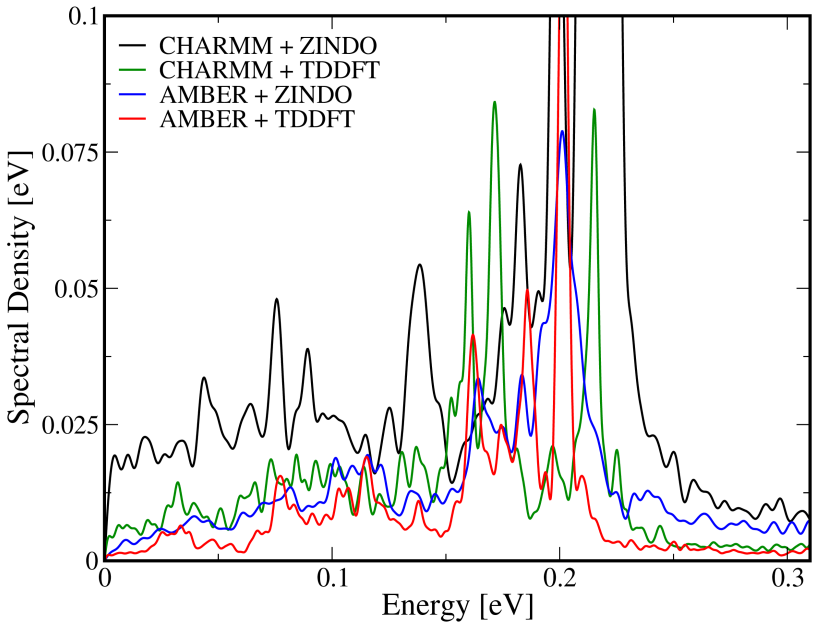

Figure 2.9: Spectral density for a single BChl *a* using the AMBER and CHARMM force fields together with the TIP3P water model. The vertical excitation energies have been determined using the ZINDO/S-CIS or TDDFT approaches.

most symmetric variant, i.e., AMBER force field together with TDDFT calculations, results in the smallest spectral densities at low frequencies. It does not matter if the tail in the DOS is to higher or lower energies. What counts is the fact that there are energy gaps with a low abundance with rather large deviations from the average. This can be interpreted as energy gaps belonging to fluctuations with a low frequency which correspondingly show up in the spectral density.

2.6 Enlarging the QM region in the QM/MM calculations

One of the possible options to test the effect of the force field on the excitation energies is to enlarge the QM region, i.e., include waters close to the solute molecule from the MM into the QM region. Surrounding a QM with MM point charges can potentially lead to overpolarization [134] and effects like charge transfer between solute and solvent can be included by increasing the QM region. Here we want to test if we can see a clear difference between the CHARMM and AMBER force fields when enlarging the QM region. So we

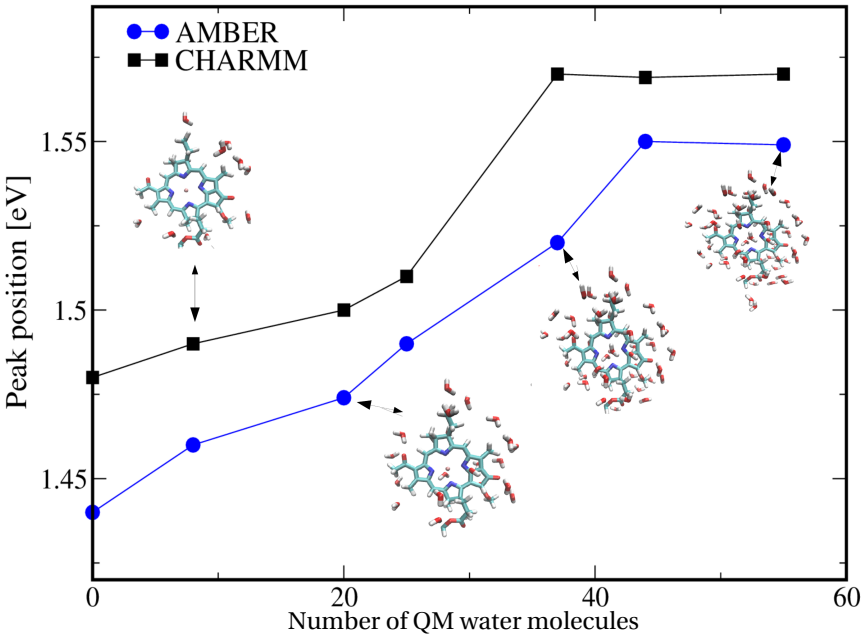

Figure 2.10: Peak position of the DOS after including an increasing number of TIP3P water molecules into QM region in addition to the single BChl *a*.

convert the nearest waters within a radius of about 4 Å around the QM chromophore to a QM representation in order to determine the influence on the site energy distribution. Due to the computational effort needed we only perform this study using the ZINDO/S-CIS approach. A similar study for rhodopsin has been performed by Valsson et al. [71] On the TDDFT level such a study is computational very expensive unless one uses a quantum chemistry code running on GPUs [134].

In Fig. 2.10 we show the results for the peak positions of the energy gap DOS. On increasing the QM region the excitation energies show a blue shift for both force fields. The largest effects are shown for replacing the nearby MM water by QM waters. For waters in a distance of 3-4 Å the effect becomes considerably smaller. This is consistent with earlier findings for other systems [71, 134, 135]. The study on rhodopsin using the ZINDO/S-CIS approach leads to findings which bear some similarities with the present one. Another interesting observation is that upon adding water molecules to the QM region, the asymmetry of the distributions increases as well as the broadening of the widths of the distribution for both forcefields (data not shown).

Concerning the comparison of the CHARMM and AMBER force fields, both behave rather similar. Using the CHARMM force field, the plateau energy is reached with a slightly smaller number of QM water molecules than in case of the AMBER force field. At the same

time, the difference of the peak position using no QM waters and the energy using more than 50 QM waters (the plateau energy) is slightly smaller in case of the CHARMM force field. This is partly due to the smaller energy differences using no or using 10 QM waters. So the fact that the CHARMM results change less when converting MM into QM waters is slightly in favor of the CHARMM over the AMBER force field.

2.7 Discussions and Conclusion

Two force fields and two approaches to calculate the vertical excitation energy have been compared based on the site distribution of energy states and on the spectral density. Further more detailed analysis, were performed on a single BChl a molecule in solution. Interestingly, the CHARMM force field leads to energy distributions significantly more asymmetric than those obtained using AMBER. In particular, the long tails of the asymmetric distribution can be connected to infrequent site energies which in turn lead to larger spectral densities at low frequencies. Especially the combination of CHARMM force field and ZINDO quantum chemistry lead to a very long tail in the energy distribution. This kind of large spectral density in the low frequency range found to vary exciton transfer dynamics in this kind of systems [98].

These results for a single BChl *a* can be directly connected to those for the pigments in the FMO complex, we can see exactly the same trend as for the single BChl *a* molecule. For example, in Ref. 86 a quite asymmetric DOS for the combination of CHARMM force field and ZINDO/S-CIS quantum chemistry can be seen. In Ref. 108, however, the combination using AMBER and TDDFT leads to an energy distribution that is quite symmetric and Gaussian-like. As in the case of a single BChl *a* molecule in solution, also in the FMO complex the spectral densities obtained using the CHARMM force fields are the largest in the low frequency region. The AMBER force field seems to lead to more symmetric DOS and therefore smaller spectral densities. The combination of CHARMM force field and ZINDO/S-CIS method, always seem to result in the largest spectral densities in the interesting frequency regime. AMBER force field with TDDFT yields in all studied cases to the lowest spectral densities. This is consistent with the study by List et al. [100] in which it was shown that TDDFT calculations with the BLYP and B3LYP functionals react less on changes in the environmental point charges as the ZINDO/S-CIS scheme. There is a possibility, however, that TDDFT-B3LYP actually reacts to little to changes in the environment as seen by a study on retinal proteins [122].

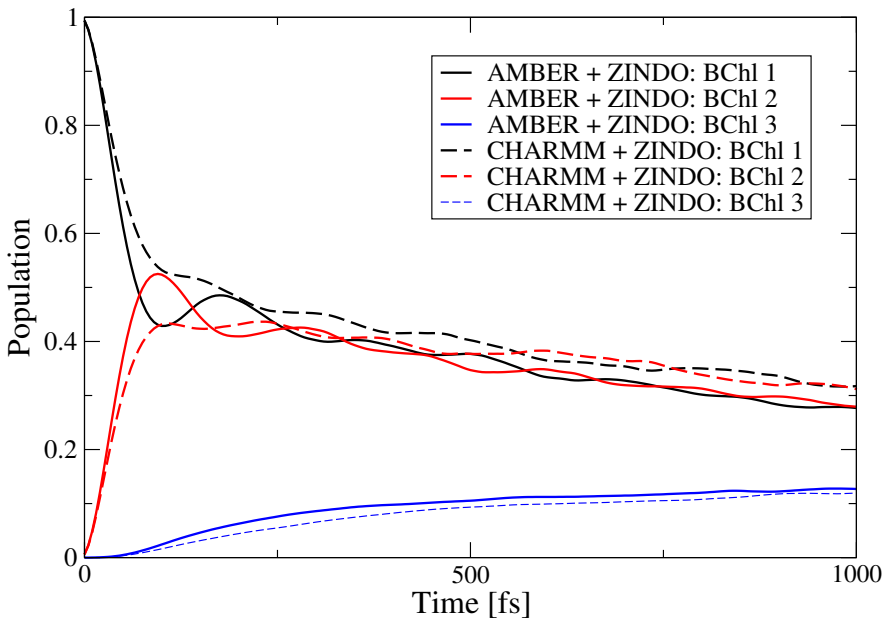

Figure 2.11: Population dynamics obtained by stochastic integration of the CHARMM-ZINDO and AMBER-ZINDO time-dependent Hamiltonians for the FMO complex of *P. aestuarii* with initial excitation in site 1.

We want to stress once more that, though the differences in the spectral densities between the four variants of force fields and QM method are not tremendous, the outcome of quantum dynamical simulations using the different simulations is rather large [102, 136, 137]. To see the effect of the different site energy fluctuations we briefly show the population dynamics in the FMO complex. We excite BChl 1 and determine the population transfer to the other BChls and show results for the first three pigments in Fig. 2.11. Concerning the intensively discussed question of coherences in the population transfer the AMBER-ZINDO/S combination shows some clear oscillation while the CHARMM-ZINDO/S version only shows weak reminiscences of oscillations though the two respective spectral densities do not differ very much.

Effects of force fields on the molecular dynamics and especially on the secondary structure formation have been studied in detail [138–140]. Moreover, the effect of force fields and especially partial charges on linear and non-linear spectroscopy [141–144] have been investigated to some extent. The present study the effect of the force fields and partial charges on the coupling between solute and solvent became apparent.

To be able to reduce the effect of the force field artifacts on the excitation energies, surrounding water molecules were included into the QM region in case of a single BChl. It became apparent that the waters with roughly 4 Å around the solute are mostly affecting the excitation energies. In this study, however, both force field sets behave rather similar. At

this point it would be interesting to get a comparison with fully quantum simulations which might be possible with approximate approaches.

In conclusion, we can state that, within the tested range of combinations, the effect of the force fields on the spectral densities seems to be larger than that of the quantum approach. It might well be that the combination of CHARMM and ZINDO yields too large spectral densities at low frequencies. CHARMM and AMBER lead to similar energy distributions when the QM/MM coupling is neglected indicating that similar pigment conformations are sampled. When, however, the electrostatic coupling between the pigments and the partial charges of the environment, i.e., protein, other pigments and water, is taken into account, there is a severe difference between the employed force fields. As discussed above, a large portion of these variations are due to different orientational polarizations of the surrounding liquid by the charges of the chromophores. The MM charges of the two force fields are quite different due to the dissimilar parametrization strategies for the partial charges in CHARMM and AMBER. None of them is, however, designed for QM/MM calculations and more research in this direction is in order.

Chapter 3

A CHARMM general force field for Bacteriochlorophyll *a* and its application to the FMO Protein Complex

Abstract

Bacteriochlorophyll *a* (BChl *a*) is one of the key chromophoric pigment of many light harvesting complexes. The intrinsic atomistic behavior of the molecules can be better elucidated using theoretical studies in a huge complex protein environment rather than experimental studies. The QM/MM calculation for these kind of complexes has been found to describe the long-lived quantum coherence behavior for LH systems. For that proper description of nuclear and electronic degree of freedom is necessary. For these BChl *a* force field (FF) was re-parameterized using CHARMM General FF (CGenFF) method. The new force field parameters were developed using the actual CGenFF procedure in obtaining partial charges. The bond, angle and dihedral parameters are obtained by reduced quantum computation (B3LYP/6-31G**) method. The new CGenFF BChl *a* FF was tested by MD simulation of single BChl *a* and Fenna-Matthews-Olson (FMO) complex. The obtained excitation energy of new CGenFF peak position matches with the AMBER FF results, however the shape of the curve matches with previous CHARMM FF results. This result again proves that the system excitation energy varies mainly on the environmental fluctuation or mainly depends on the behaviour of bath and not on the system FF used.

3.1 Introduction

Bacteriochlorophylls are photosynthetic pigments that exist in various phototrophic bacteria[2, 145] mainly involved in anoxygenic photosynthetic process. Of the different types of Bacteriochlorophylls, Bacteriochlorophyll *a* (BChl *a*) is one of the key pigments found in many of these bacterial systems, i.e., for example, in light harvesting complexes like LH-I [146], LH-II [146, 147] and the Fenna-Matthews-Olson (FMO) complex [148]. In these LH systems, the BChl *a* pigments are arranged in various organizational structures and lead to the absorption of photons, to efficient excitation energy transfer but also to charge transfer in special pairs. The observation of long-lived quantum coherence in some light-harvesting complexes lead to an enormous interest in these systems [28, 96].

Due to the large size of most biomolecular systems including light-harvesting complexes, quantum chemistry and especially quantum dynamical calculations are unfeasible. For these systems, molecular dynamics (MD) simulations have become a very valuable tool [149]. In MD simulations, the potential energy is calculated based on empirical potentials, which have been determined in advance to reproduce quantum chemical calculations and experimental results. The set of parameters that determines a specific functional form of this potential is generally denominated as FF. Several standard FFs for proteins exist, i.e., AMBER [150], CHARMM [151], GROMOS [152] and OPLS [153]. However, non-standard residues or cofactors can be involved in protein complexes for which no parameters exist in these standard FF sets. In those cases, new FFs need to be developed, which are either based on existing parameters or new ones need to be generated usually based on ab-initio calculations. Developing a reliable and reproducible FF for describing a set of selected properties is a challenging task [154]. To this end, several tools are available which allow for the development of new FFs consistent with standard FF sets, for example, the General AMBER FF (GAFF) [154] and the CHARMM General FF (CGenFF) [155].

The various FF sets differ as a consequence of their varying parametrization procedures used to obtain the bonded and non-bonded parameters. One of the important differences among the different FF sets is the fitting procedure for the partial charges. For example, partial charges are obtained from fitting the electrostatic potential in the AMBER FF [156], while they are derived by fitting experimentally measured condensed phase properties in the OPLS parameter set [157]. Moreover, the CHARMM FF parametrization is based on reproducing quantum chemical interaction energies between the molecule of interest and TIP3P water molecules [155]. The convention followed in CHARMM is to assign each water-accessible atom of the compound to a list of hydrogen bond donors, acceptors or

both [155, 158]. Subsequently, the interaction energies among these atoms is obtained from QM calculations. Finally, the interaction energies and dipole moments are reproduced using molecular mechanics by fitting the partial charges.

Several light-harvesting systems have been studied over the last year used MD simulations alone or in combination with quantum calculations [82, 159]. The FMO complex, for example, mediates the exciton energy transfer between chlorosomes and the respective reaction centres. FMO is a trimmer protein existing in green sulfur bacteria from, for example, *Prosthecochloris aestuarii* (pdb code: 3EOJ) [97] and *Chlorobaculum tepidum* (pdb code: 3ENI) [97]. This complex contains 24 BChl *a* molecules, i.e., 8 BChl *a* pigments in each monomer. Since the crystal structure of it exist from different bacteria for quite a while [25, 97, 160], various theoretical studies at the molecular level have been performed [106, 159]. In this protein environment, the central magnesium atom of the BChl *a* chromophore is bound to a histidine residue of the protein. In a previous study [161], the present authors among others carried out a FF comparison between the CHARMM and AMBER sets for a FMO complex and for a single BChl *a*. This study which also involved a combination to QM methods revealed that the environmental charges play a key role in determining the excitation energies in QM/MM calculations. For example, QM/MM calculations using the CHARMM FF together with the semi-empirical ZINDO/S-CIS approach (Zerner Intermediate Neglect of Differential Orbital method with parameters for spectroscopic properties together with the configuration interaction scheme using single excitations only) [86, 119, 120] always resulted in broader distributions of excitation energies compared to other combinations. The non-Gaussian distributions of the excitation energies can be correlated to an increased spectral density in the lower frequency region. The spectral density is one of the key analysis method that one can employ to determine the magnitude of coupling between bath and system. [86, 104, 162, 163]. The spectral density can be computed by correlating the extracted transition energies along different sampling times.

The detailed spectral density analysis method is reported else where [107, 163, 164]. However, the AMBER FF along with the time-dependent density functional theory (TDDFT at B3LYP/3-21G* level) method underestimates the environmental effect [108]. When performing the excitation energy calculations without environmental charges, both FFs have the same energy distribution using various QM methods. From this finding one can conclude that the system FF has only an indirect influence on the QM method. In a similar fashion Wang et al. [165] reported a comparative FF study for the FMO complex using the ZINDO/S-CIS and the charge density coupling (CDC) quantum chemistry approaches.

Folope et al.[166] developed the first CHARMM FF parameters for BChl *a* and bacte-

riopheophytin molecules using Mulliken population analysis employing semi-empirical QM methods like AM1 (Austin Model 1) and PM3 (parametrized model 3). Later on Damjanovic et al. [107] modified the partial charges of the FF parameters by Folope et al. using the electrostatic potential (RESP) method. In 2005, a CHARMM parametrization for Chl *a* was published [167]. Together with a detailed normal mode analysis, BChl *a* for the AMBER set were reported in Ref. 117. Later on, this approach was extended to other pigments [168]. In the present contribution, we are revisiting the parametrization of BChl *a* for the CHARMM FF set more strictly following the CHARMM procedure for the generation of FF parameters. To this end, we have a parametrization according to the CGenFF scheme [155] using the FFTK plugin developed by Mayne et al. [169]. Moreover, it is investigated as a test whether the excitation energy calculations lead to proper maybe even outplacing the present CHARMM FF [107], which has already been used in numerous studies.

The manuscript is organized as follows. In the methods section we describe in detail the quantum methods and the parametrization work flow. Later the detailed description of parametrization procedure (partial charges, bond, angle and dihedral) for BChl *a* were obtained. Subsequently, the generated CGenFF parameters are tested for an individual BChl *a* in solution and further study has been carried out in FMO complex and spectral density analysis is carried out in comparison with previous results [104, 108, 109, 161].

3.2 Methods

The various FF differ not only by the parametrization procedures between the various but also by smaller differences in the employed functional forms. The CGenFF potential energy is composed by a sum of bonded and non-bonded terms via [155]:

$$\begin{aligned} U = &\sum_{\text{bonds}} K_b(b-b_0)^2 + \sum_{\text{angles}} K_\theta(\theta-\theta_0)^2 + \sum_{\text{dihedrals}} K_\phi(1+\cos(n\phi-\delta)) \\ &+ \sum_{\text{impropers}} K_\omega(\omega-\omega_0)^2 + \sum_{\text{Urey}-\text{Bradley}} K_{UB}(r_{1,3}-r_{1,3;0})^2 \\ &+ \sum_{\text{nonbonded}} \varepsilon\left[\left(\frac{R_{\min,ij}}{r_{ij}}\right)^{12} - 2\left(\frac{R_{\min,ij}}{r_{ij}}\right)^{6}\right] + \frac{q_i q_j}{4\pi\varepsilon_o r_{ij}} \,. \end{aligned} \tag{3.1}$$

The bonded interactions contain terms for covalent bonds, bond angles, improper angles and dihedral angles. While the first three terms are described by harmonic functions, the dihedral angles are represented in terms of sigmoidal functions. Moreover, a Urey-Bradley

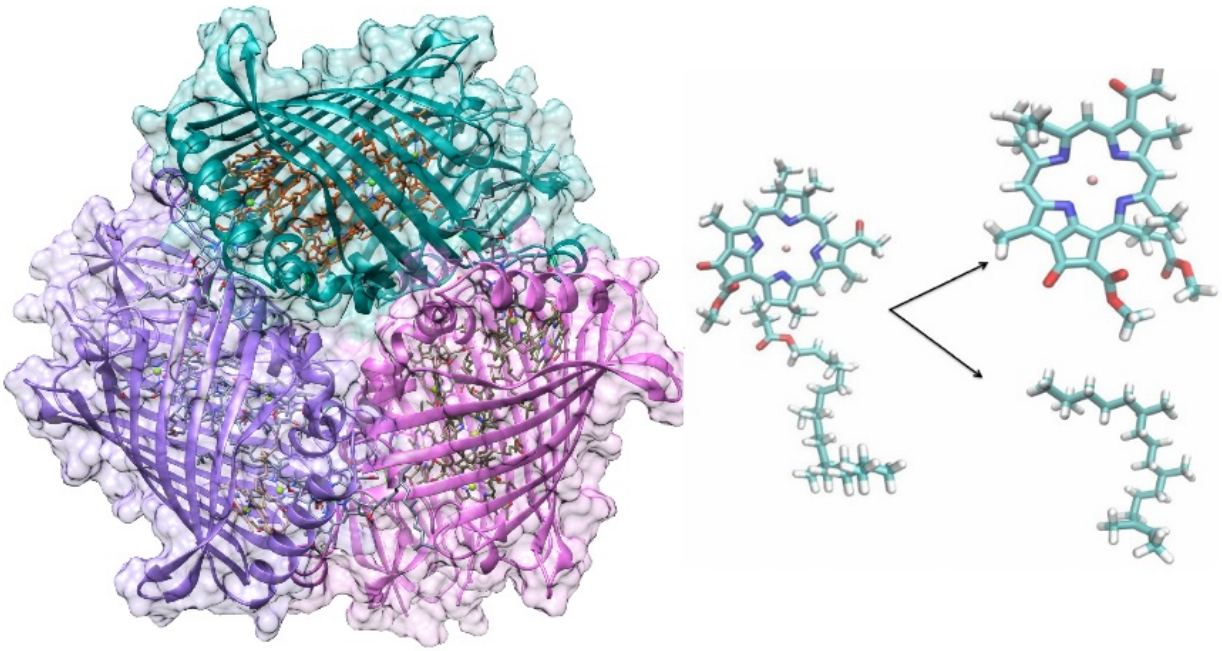

Figure 3.1: Structure of the FMO trimer including its pigments in the left panel. The middle panel displays a single BChl *a* molecule and on the right the truncation of the chromophore into head part phytyl chain is depicted.

term is present in the general form of the CHARMM FF although not being used in the present study. The non-bonded terms include the Coulomb and van-der Waals interactions. In Eq. 3.1, K_b, K_θ, K_ϕ, K_ω, and K_{UB} are the force constants for bond stretching, valence angle bending, dihedral angles, improper angles and the Urey-Bradley term respectively. The constants b_0, θ_0, ϕ_0, ω_0 and $r_{1,3;0}$ denote the corresponding equilibrium values. The pairwise non-bonded interactions between atoms i and j separated by a distance r_{ij} is given by the sum of the Coulomb interaction between their atomic partial charges q_i and q_j and the van der Waals energy computed as a Lennard-Jones potential. In calculations with explicit solvent, the dielectric constant ε is set to 1 (permittivity of vacuum). For the Lennard-Jones term the ε_{ij} denote the well depths and the $R_{\min,ij}$ the corresponding distance at the Lennard-Jones minimum. Interactions between atoms separated by one or two covalent bonds (1-2 and 1-3 interactions, respectively) are described through bond and valence angle terms. Non-bonded interactions between atoms separated by three bonds are not scaled in the CHARMM FF, i.e., no 1-4 scaling is present. The force constants, equilibrium values, atomic partial charges, and van der Waals parameters, are part of the force-field parameters. The force field parameters for a given molecule are derived using data from experiments and/or quantum chemical computations on these compounds.

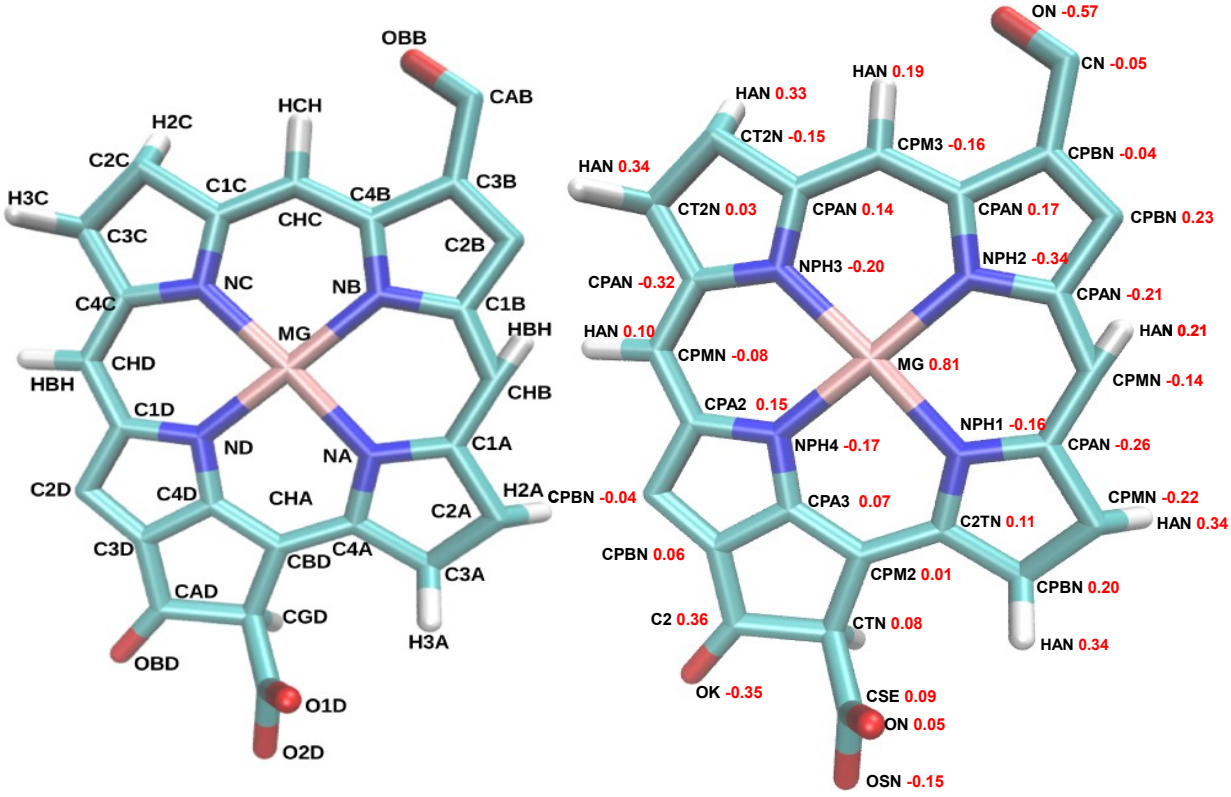

Figure 3.2: Structure of BChl *a* with the atom selection employed during the quantum calculations [161]. The left panel presents the atom names used as also used in several PDB files. The right part depicts the assigned atom type along with optimized partial charges.

Force fields exist for all amino acids and mostly in various protonation states so that modelling of protein and other simple biological molecules causes usually little problems in this respect. For non-standard residue such as ligands or drugs the FF parameters do not exist or the extracted parameters from standard libraries will not be suitable sometimes. The chromophore BChl *a* is such a non-standard molecule and therefore no standard FF parameters do exist. Previous attempts have been discussed above. In the present study we tried to follow the CGenFF procedure as close as possible for such a large molecule to get a consistent FF for the use with CHARMM FFs. The initial coordinates of the BChl *a* were taken from the crystal structure of FMO complex(fig:3.1) from *Prosthecochloris aestuarii* (pdb code 3EOJ) [97]. Missing hydrogen atoms were added to the BChl *a* molecule from the crystal structure. Since an earlier CHARMM FF for the BChl *a* pigment is available [107], the same atom names and types have been assigned. For computational efficiency, we

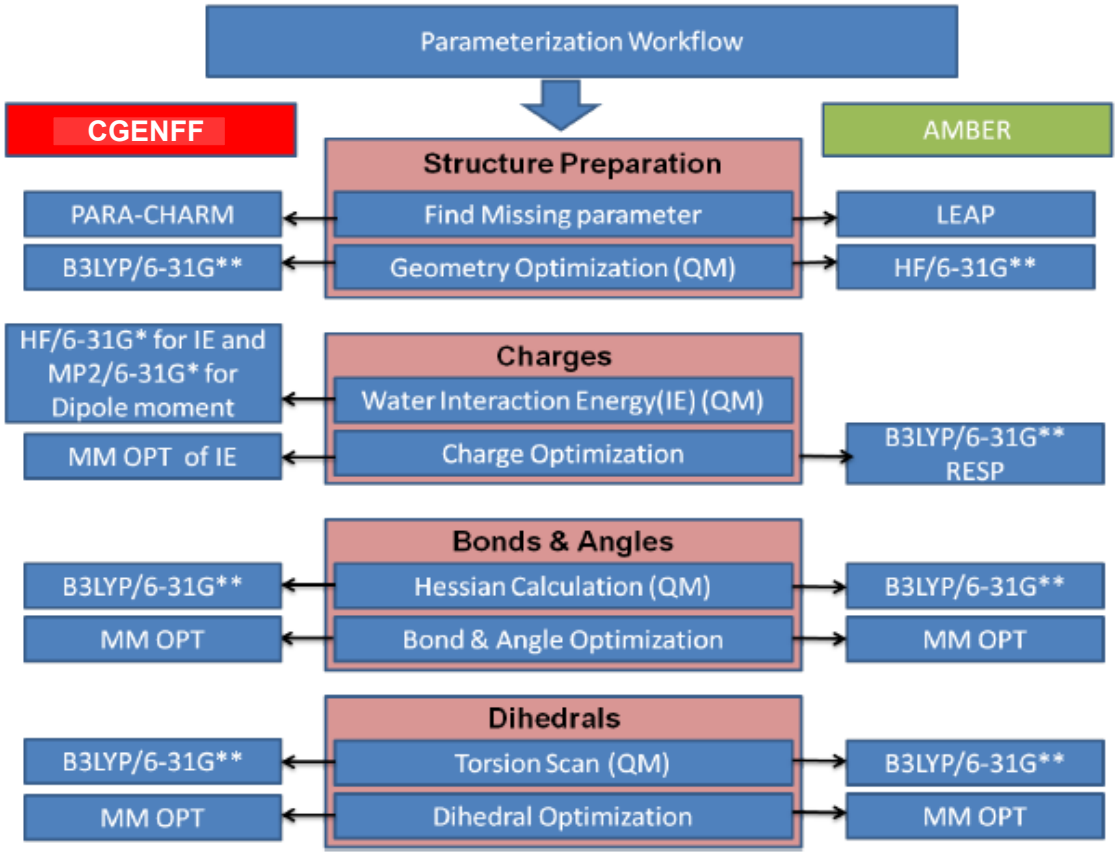

Figure 3.3: The flowchart shows the schematic representation of parametrization procedure followed. The left side depicts the modified CGenFF parametrization, while the right side shows the AMBER FF parametrization followed by Ceccarelli et al. [117] for single BChl *a* pigments.

truncated the phytyl tail as shown in (Fig. 3.1) such that only the head part was considered for the parametrization procedure. This procedure was also followed in earlier parametrization attempts [117]. Later the ParamChem software [155, 170, 171] was used to determine the parameters for the phytyl part. The QM calculations were carried out only for the core structure, i.e., the head of the BChl *a* molecule containing 85 atoms. Due to this large number of atoms, we have deviated from the CGenFF parametrization procedure [169] in the case of bond, angle and dihedral optimization except charge optimization step. A work flow of the adopted CGenFF procedure is shown in Fig. 3.3. All electronic structure calculations were done using the Gaussian09W package[172] and FFTK plug-in[169] of VMD is used to optimize the obtained MD property.

The initial step is to assign the Lennard-Jones and improper angle from the standard

CHARMM27 set. Since FFTK does not include parametrization step to obtain the Lennard-Jones and improper angle parameters. Later the geometry of the BChl *a* chromophore was optimized at the B3LYP/6-31G** level. The next step is to determine the partial charges, which were determined by reproducing the QM interactions with specifically placed TIP3P water molecules at each hydrogen bond donors (hydrogen and magnesium) or acceptors (oxygen and nitrogen). The placement of water molecules was automatically determined by the FFTK plugin. For example, three water molecules are placed per oxygen atom and in some cases of neutral carbon atoms, TIP3P water molecules with different direction, i.e., hydrogen and oxygen atoms pointing towards the carbon atom, are positioned. Subsequently the single point quantum calculations were done independently at the HF/6-31G* level for each individual sites to obtain the interaction energies and their respective minimum distances. The QM interaction energies are defined relative to the bare optimized geometry energies together with the energy of a separate water molecule. The obtained QM interaction energies are scaled by a factor of 1.16 to account for the bulk properties used for neutral molecules.

Later the partial charges are fitted (Eq. 3.2) with respect to minimum distances and energies for each interaction site $\Psi_{interacions}$ and Ψ_{dipole} between QM and MM calculations using a simulated annealing algorithm to fit the objective value with set of trial charges. The optimization has been carried out by setting the QM to MM interaction distance by ± 0.1 $\mathring{A}$ and interaction energies by ± 0.2 kcal/mol. The detailed algorithm function and the MM optimization procedure is reported elsewhere [169].

$$\Psi_{charge} = \Psi_{interactions} + \Psi_{dipole} \tag{3.2}$$

The next step in the parametrization scheme is to determine the bond and angle parameters. For that QM Hessian calculation at B3LYP/6-31G** level is performed [173]. Unlike the partial charge optimization, automatically fitting the bond and angle parameters is not straightforward because correlating the vibrational spectrum directly with force constant and angle parameter is a complex task, which sometimes needs some manual intervention. For that FFTK optimizes the bond and angle parameters simultaneously, while the dihedral angle calculations are carried out separately. The bond and angle parameters are fitted with respect to the potential energy difference of QM with respect to various trial MM Hessian calculation. The main difference in force constant values occurs primarily due to fitting procedure between QM and MM potential energy surfaces (PES), because they are fitted with respect to internal coordinates. So the change in one force constant of one bond might change the motions of neighboring atoms affects the vibrational modes. This is due to the

fact normal modes are fitted with respect to Cartesian coordinates. The bond and angle were also fitted under various trial methods using simulated annealing algorithm with the following parameter.

The QM and MM bond force constant difference with respect to lower and upper bound is 0 to 1000 kcal/(mol*A^2) and the bond distance equilibrium values of deviation have been set ± 0.03 $\mathring{A}$ and for angles the equilibrium of deviation was kept ± 10 ° and the force constant lower and upper bound is set between 0 to 300 kcal/(mol*radian^2). A detailed description of the bond and angle parameter fitting is given in the Results and Discussion section. The QM dihedral angle energy profiles were obtained at the B3LYP/6-31G** level with ±90° with a step size of 5.0°. In most of the cases it is assigned to 0° or 180° by default depending on whether it is a cis or trans confirmation respectively.

The obtained FF parameters were tested using MD simulation for an individual BChl *a* molecule in a TIP3P water box using NAMD 2.9 [174]. The simulations were performed using periodic boundary conditions under NPT ensemble by keeping constant pressure at 1 bar and temperature at 300 K using the Langevin piston and thermostat methods. The short-range electrostatic interactions were evaluated for every step, while the long-range electrostatics was determined every second step. The cut-off for non-bonded interactions was 12 Å with a smoothing function applied starting at 10 Å. The non-bonded interactions were excluded for the 1-2 and 1-3 terms. Moreover, the NAMD energy plugin was employed to obtain the total energy and the individual bond, angle, dihedral and non-bonded energies of the molecule in solution.

3.3 Force Field Parametrization

CHARMM FF parameters can also be predicted using the CGenFF web server called Paramchem website (www.paramchem.org)[155, 170, 175]. It employs a structural matching algorithm and obtains the parameters and gives out scores for better matched parameters from the standard CGenFF. The main problem in the present case is the magnesium atom present in BChl *a*, since the automated parameter assignment tool is not suitable for such inorganic complexes and also it failed for bacteriopheophytin due to the extended conjugation in the system because the penalty score was high. Therefore, we have decided to use the FFTK to undergo complete parametrisation procedure. First the atom names and atom types are matched with respect to Haemoglobin and BChl *a* atom types from standard. Later the

Table 3.1: The table lists the atom names, QM and MM interaction energies, positions of the QM energy minima and deviations of the MM minimum positions from the QM ones.

Interaction site	ΔE_{QM}	ΔE_{QM-MM}	R_{QM}	ΔR_{QM-MM}
MG	-12.69	0.28	2.49	-0.100
NA	-2.77	-0.04	3.47	-0.100
NB	-4.00	0.23	3.30	-0.050
NC	-3.19	0.33	3.43	-0.100
ND	-3.71	0.36	3.30	-0.050
C1A	-5.56	-0.234	4.128	-0.150
C1C	-2.59	0.043	3.661	-0.050
C1D	-3.69	-0.428	3.558	-0.350
C2B	-1.77	-0.421	3.641	-0.200
C3D	-3.90	0.259	3.652	-0.100
C4A	-1.81	-0.257	3.761	0.150
C4B	-2.37	0.187	3.625	-0.250
C4D	-5.39	-0.140	3.563	-0.300
CGA	-3.05	-0.345	3.785	-0.200
CHA	-5.75	0.352	4.540	-0.050
CHB	-3.46	-0.012	3.519	-0.300
CHD	-3.66	0.199	3.508	-0.250
O1D	-4.39	0.821	3.394	0.250
O1D	-6.90	0.325	2.984	-0.050
O2A	-3.86	0.105	3.060	0.100
O2D	-8.07	0.432	3.019	0.000
OBB	-6.06	-0.605	2.999	-0.100
OBB	-6.63	-0.461	2.970	-0.050
OBD	-1.20	0.039	5.037	-0.100
OBD	-4.17	1.250	4.235	0.400
OBD	-6.00	1.075	3.015	0.000
C1C	-1.16	-0.165	3.886	0.000
C2B	-1.07	-0.631	3.504	-0.050
C4A	-1.44	-0.218	4.321	0.100
C4C	-1.22	0.335	3.948	0.250
C4D	-1.37	-0.726	3.194	0.100

phytyl part is truncated into two major parts from the central ring to reduce the computational cost during the FF optimization process.

Table 3.1: The table lists the atom names, QM and MM interaction energies, positions of the QM energy minima and deviations of the MM minimum positions from the QM ones.

Interaction site	ΔE_{QM}	ΔE_{QM-MM}	R_{QM}	ΔR_{QM-MM}
H2C	-2.03	0.444	2.643	0.200
H3A	-2.46	-0.406	2.786	0.100
HAA2	-2.35	0.016	2.606	0.200
HAC1	-1.79	0.303	2.637	0.250
HAC2	-1.92	-0.215	2.897	-0.050
HBA1	-2.37	0.675	2.542	0.250
HBA2	-2.17	0.100	2.860	0.150
HBB1	-3.05	0.570	2.661	0.150
HBB2	-2.97	0.801	2.680	0.150
HBC1	-1.08	0.369	2.797	0.150
HBC2	-1.36	-0.133	2.778	0.100
HBC3	-2.59	0.817	2.778	0.150
HBD	-1.76	-0.577	2.523	0.250
HD1	-1.09	-0.457	2.674	0.100
HD2	-1.16	0.402	5.443	-0.250
HDH	-2.49	0.017	2.660	0.150
HMB2	-3.06	0.954	2.585	0.300
HMB3	-1.62	-0.220	5.037	0.300
HMC1	-4.48	0.573	2.417	0.250
HMC2	-1.40	0.371	2.771	0.150
HMC3	-1.78	0.739	2.686	0.250
HMD1	-1.01	0.747	2.396	0.400
HMD2	-1.24	0.366	2.664	0.200
HMD3	-1.44	0.368	2.673	0.200

3.3.1 Fitting partial charges

For fitting the partial charges the truncated BChl *a* was taken and interaction energies were obtained at the single point calculation (HF/6-31G*) for TIP3P water molecule at 102 sites. (Interaction energy and fitting procedure is explained in detail at methods section). Further, we have selected 53 site energies to optimize the partial charges. The site energies are selected by expelling the sites with positive interaction energy and very low interaction energy, for eg., smaller than 1 Kcal/mol were removed before the subsequent analysis. For instance the potential energy converged along longer reaction coordinate are also not taken into account.

The table:3.1 shows the interaction energy and interaction distance for selected sites and also the difference in QM and MM fitted values. The magnesium atom has the largest

interaction energy of all pairs, i.e., -12.69 Kcal/mol. Subsequently charges are fitted using the simulated-annealing variant and downhill simplex method over repeated runs. Of these interactions, a poor fit is only observed in case of oxygen atom with a difference larger than 1 Kcal/mol. This mismatch is observed only in the case where two extra water molecule where placed for the same oxygen atom that is energetically quite unfavorable. The total dipole moment obtained from the QM calculations is found to be 2.69 D, while from MM it is 3.86 D. The agreement between QM and MM has been found to be better in our case despite the huge number of interaction sites selected. The optimized charges of CHARMM [107] and AMBER [117] are shown in table3.2. The optimized new CGenFF charges varies considerably compared to previously developed FF for BChl a. For example the optimized charge of magnesium atom by the present approach is 0.81 e while the previous charges are 1.17 e for CHARMM and 0.13 e for AMBER for the same BChl a molecule.

Table 3.2: List of partial charges BChl *a* from the present approach compared to two previous FF sets.

Atom name	**CGenFF**	**CHARMM[107]**	**AMBER[117]**
MG	0.81	1.02	0.13
NA	-0.16	-0.33	0.04
NB	-0.34	-0.72	-0.06
NC	-0.20	-0.28	0.07
ND	-0.17	-0.50	0.07
C1A	-0.26	-0.28	-0.12
CHA	0.01	0.46	0.07
C4D	0.07	0.02	-0.13
C1B	0.19	0.48	-0.03
CHB	-0.14	-0.71	-0.22
C4A	0.11	0.39	-0.04
C1C	0.14	0.23	-0.09
CHC	-0.16	-0.65	-0.27
C4B	0.17	0.55	0.20
C1D	0.15	0.17	-0.05
CHD	-0.08	-0.28	-0.26
C4C	-0.32	-0.13	-0.06
C2A	-0.22	-0.31	0.09
CAA	0.04	0.09	-0.06
C3A	0.20	0.49	0.26
CMA	-0.21	-0.54	-0.28
C2B	0.23	0.11	0.20
CMB	-0.12	-0.19	-0.24

3.3.2 Bond and Angle Parameter Optimization

The bond and angle parameters QM Hessian calculation are done at B3LYP/6-31G** level for the target molecule. Better agreement has been obtained in terms of QM and MM fitted bond length (table 3.3), but the force constant values obtained by the optimization procedure has a huge difference between the QM and MM values. It might be due to fact that FFTK employs NAMD energy calculation for each step to obtain the respective force constant and bond length by simulated annealing algorithm. So we have selected similar atom types and it's respective angles to fit the QM data step by step. For example Mg and it is four N atom (atom types Mg, NPH1, NPH2, NPH3 and NPH4) related bond and angle parameters are optimized as a set. The normal difference in force constant are fitted between $\approx$ 10 Kcal/mol, but in some extreme cases the results are still really unmatchable. Like in the case of CSE-ON the difference is around $\Delta QM - MM$ -158 Kcal/mol and for CSE-OSN $\Delta QM - MM$ is +234 Kcal/mol. Having considered that it might be the optimal force constant parameters for the respective charges, a test simulation was attempted using single BChl a molecule (the single BChl a system setup has been explained in methods section). But the results obtained by spectral density has been found to show some abnormal peaks compared to the QM IR plot and the results also varies from the previous FF spectral density results. The main peak of carbonyl (C=O) which usually observed at $\approx$ 0.21 eV appears at $\approx$ 0.27 eV, this is due to the fact of unmatched force constant values stated above. The spectral density peaks basically represents the fingerprint region of IR peaks, but the lower frequency part is believed to be the electronic coupling arising due to the system and bath coupling. So in this case the lower frequency part matches with previous CHARMM FF, but not with respect to higher frequency region. So we have tweaked the force constant values to obtain the appropriate IR finger print region peaks in the higher frequency part.

3.3.3 Dihedral angle optimization

The QM dihedral calculations are done at B3LYP/6-31G** level by twisting the bonds with respect to specific angle, simultaneously total energies are obtained for each twisted conformation of a specific dihedral atom (detailed procedure has been already stated in methods section). Later on the obtained energy for each individual twisted angle were combined to obtain PES for each individual dihedral angle, which was later used to fit with MM simulated annealing method. The previously reported single BChl a FF [107] contains the dihedral parameters assigned from standard CHARMM FF and many of the central ring dihedral terms force constant were kept zero. To overcome this drawback we have parametrized dihedral

Table 3.3: Reference bond length (Å) along with reference values (b_o) taken from FMO-crystal structure PDB-id 3EOJ of resid 371 BChl-a.

Bond/angle	**Ref.value b_o**	**QM value**	**MM value**
CPBN-CPAN	1.466	1.430	1.451
CPBN-CPA2	1.431	1.348	1.460
CPBN-CPA3	1.394	1.422	1.419
CPBN-CPBN	1.405	1.396	1.402
CPM3-CPAN	1.398	1.400	1.406
CPMN-CPA2	1.439	1.418	1.418
NPH4-CPA3	1.383	1.353	1.348
NPH4-CPA2	1.396	1.395	1.392
NPH1-MG	2.164	2.153	2.169
NPH2-MG	2.043	2.057	2.049
NPH3-MG	2.107	2.127	2.110
NPH4-MG	2.008	2.005	2.027
NPH1-CPAN	1.355	1.366	1.356
NPH2-CPAN	1.361	1.370	1.389
NPH3-CPAN	1.351	1.358	1.357
CT2N-C2TN	1.543	1.546	1.546
C2-CPBN	1.424	1.453	1.457
CSE-ON	1.232	1.216	1.220
CSE-OSN	1.314	1.347	1.334
CN-OK	1.220	1.232	1.230
CT2N-CT2N	1.541	1.546	1.546
CTN-CSE	1.462	1.502	1.525
C2-OK	1.219	1.218	1.217
CPBN-C2	1.424	1.453	1.461

terms by fitting the QM PES surface scan with MM energy for each individual terms. While fitting the dihedral terms care need to be taken in choosing appropriate phase angle δ and multiplicities. Sometimes over fitting of dihedral terms like huge force constant and many multiplicities will result in un-physical behavior of atoms. For example the test simulation for the central ring containing MG-NX atoms describing their dihedral angle the equilibration run crashes. On looking back at the previous CHARMM and AMBER FF parameters for the same term the force constant ($K\chi$) was assigned zero, which means it's only controlled by bond, angle and improper terms. Also on looking back at the Hemoglobin the dihedral connecting term for the central iron (FE) and nitrogen (NX) term was kept zero. The Fig. 3.4 shows the fitted PES curve for NPHX-CPAN term. In this case we have a periodicity of 1 and 2 with phase angle 180°. In most of the cases the periodicity were assigned 1 and

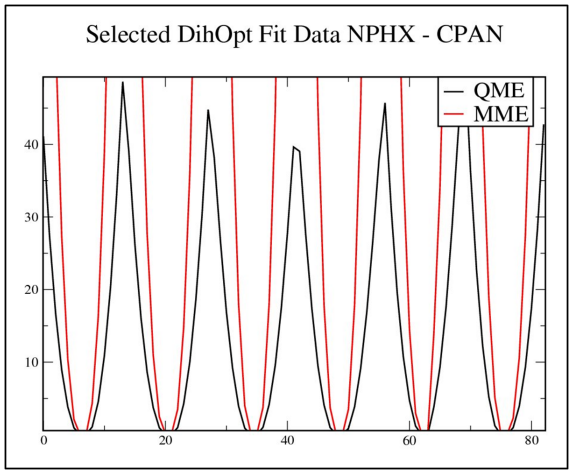

Figure 3.4: Shows the dihedral fit data for NPHX-CPAN atom type. The multiple curves correspond to an invidual NPH1-CPAN and similar atom types.

2, then the phase angle is allowed to be either 0 or 180° also exceptions are for chiral and carbonyl terms.

The FF terms have been fitted for the dihedral terms with extensive parameterization like multiple periodicities for specific dihedral term and so on. To avoid multiple periodicities single term are kept in some cases like HAN-CTN-CTN-HAN. The test MD simulation have been done for single BChl *a* in water box. The simulation results show that the dihedral energy have been found to be around 322 kcal/mol. On looking at the RMSD curve in the first case (multiple dihedral terms) takes longer equilibration time on the given simulation time. The second case (single dihedral term) has obtained equilibrium in 500 frames. So in the case where we have employed multiple periodicities has been found to be of poor agreement. The similar kind of over parameterization problem is also observed for Macrolide antibiotics too[176].

3.3.4 Validation of Force Field

To further validate the newly developed FF parameters, we have carried out MD simulation of single BChl *a* in water box as test system the same as reported in our previous publication[177]. For doing these we have initially equilibrated the system for 10 ns and production run of 100 ps of 1 fs time step is carried out. The RMSD of the QM optimized geometry in vacuum is found to be around 0.55 Å without phytyl tail. The RMSD of MM simulation in water for the same system is found to be around 0.17 Å, in this case the initial structure is from crystal structure and not QM optimized. When the same simulation was

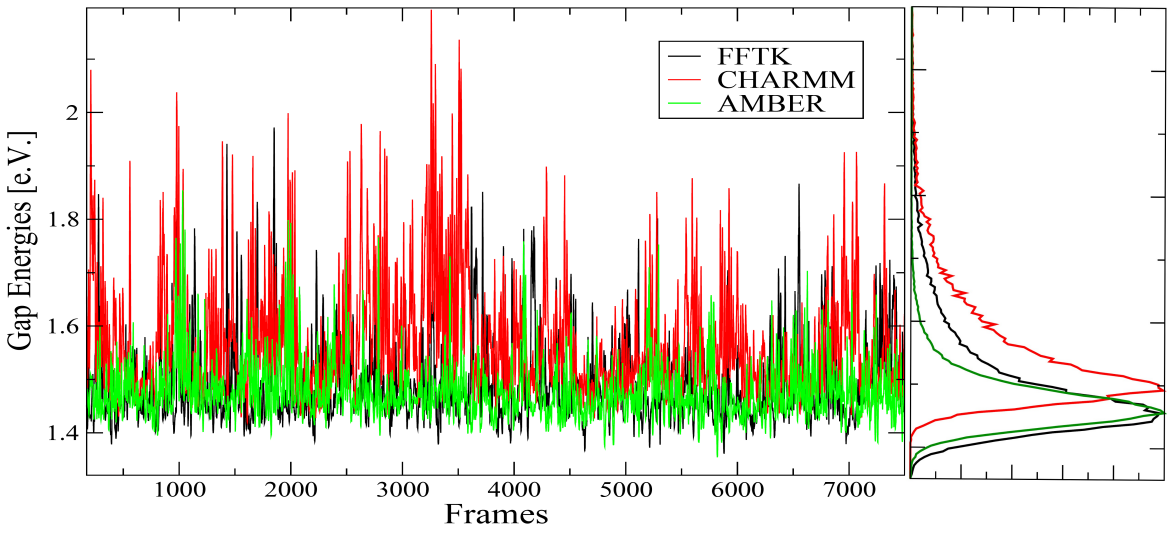

Figure 3.5: Shows the energy gap fluctuation for single BChl *a* for different FF. The right panel shows the average distribution of each individual FF

repeated inside the FMO crystal structure it is 0.56 Å.

The figure 3.5 shows the new CGenFF, CHARMM and AMBER calculated vertical transition energies(ZINDO S/CIS) along the trajectory for single BChl a. The right panel histogram shows the distribution of excitation energy (DOS) for the new CGenFF, CHARMM and AMBER. From these one can clearly see that the peak position matches with distribution of excitation energy for AMBER FF. While the peak shape matches with CHARMM FF. The first comparison of distribution of excitation energy for the first FMO 8 pigments between the new CGenFF and CHARMM is presented in fig 3.6. The results show that the new CGenFF DOS peak position matches with AMBER and the shape of the curve matches with old CHARMM FF. This proves that the energy broadening comes from the FF that is employed but the average DOS is same for both the FF.

The figure 3.7 shows the averaged spectral density graph for different FF and quantum

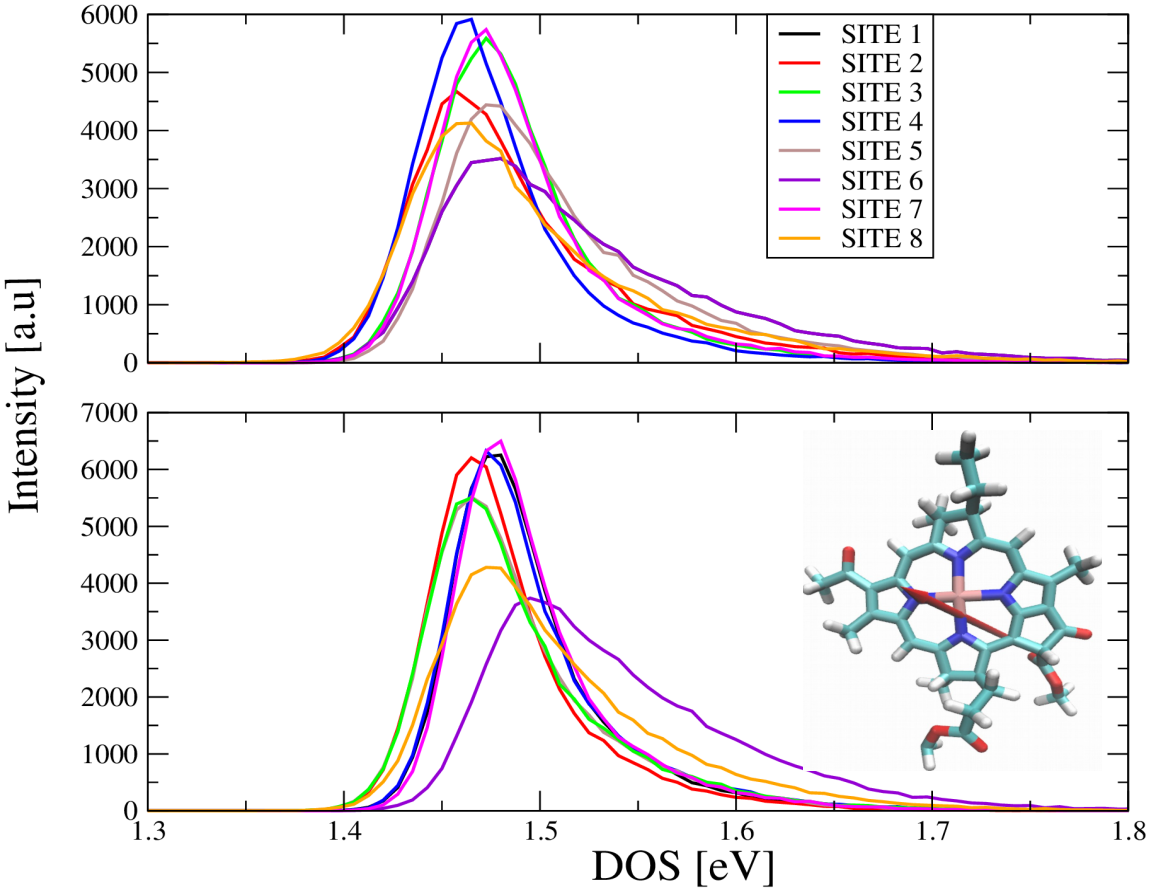

Figure 3.6: Shows the energy gap fluctuation for the first eight BChl monomer complex of FMO in CHARMM FF (top), CGenFF (bottom). The inset image shows the Single BChl molecule selected for parametrisation along with Q_y transition dipole moment.

methods used to compute the excitation energy. The detailed method for obtaining spectral density is reported elsewhere [104, 108]. The normal mode analysis along the trajectory might be a appropriate method to describe the MD optimized bonded parameters, since we don't have a proper methodology for it. We have opted to spectral density, which also have the capability to show the Infrared peaks at higher frequency region. The figure 3.7 shows increase in intensity in the lower frequency region, this region is usually attributed to the excitonic coupling between the system and bath function. The intensity of the bump is found to vary based up on the FF and quantum chemistry method used. The AMBER FF along with B3LYP/3-21g method always showed lesser intensity in that region. The new CGenFF spectral density along with ZINDO/(S-CIS) semi emprical method has found to show higher intensity in the lower frequency region. This might be due to fact the new CGenFF has additional dihedral parameters leading to more internal fluctuation of interaction with the

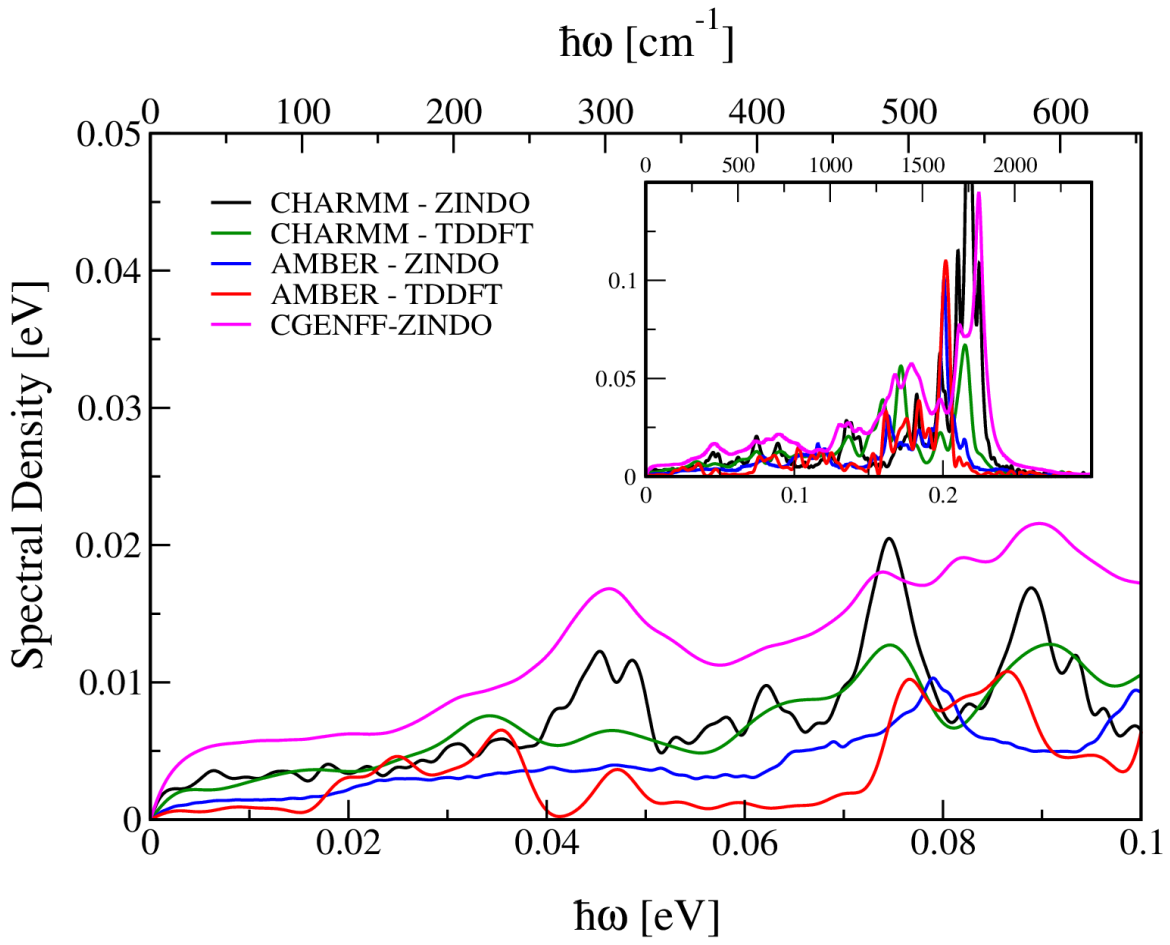

Figure 3.7: The graph shows the spectral density of different FF and QM methods previously employed for FMO complex along with newly developed CGenFF. The inset shows the same graph for higher scale.

protein molecule results in longer correlation fluctuation[133]. The other significant characteristics of IR peaks below 1000 cm^{-1} arises from in-plane and out of plane vibrational mode of distribution arising mainly from the central ring motion involving Mg, N and C of the central molecular body. The key IR finger peaks at higher frequencies also matches well with the pure QM hessian calculation as well. The peak at 1000 cm^{-1} and 1020 cm^{-1} seems to be of low intensity when compared with QM/MM obtained spectral density, because the peak corresponds to the $-CH_3$ rocking vibration of the molecule which is truncated usually during QM/MM calculation to reduce the computational cost along the trajectory.

3.4 Conclusion

A new set of CGenFF FF parameters have been generated for BChl *a* molecule. The set of partial charges were done by computing interaction energy using ab-initio method, Later on the MM IE is fitted against QM IE with better agreement. The bond and angle parameters are fitted by doing QM Hessian calculation followed by MM optimization. The bond parameters were tweaked later to match the desired frequencies. The dihedral angle are fitted by scanning the PES of each individual dihedral angle and then fitted with respect to MM energy surface computed. These parameters have been generated by using actual CGenFF procedure with reduced QM calculation levels (B3LYP/6-31G**) to overcome the drawbacks existed in the previous BChl *a* FF parameterization methods. The newly developed FF parameters has been tested in single BChl *a* and FMO complex. The QM/MM method has been used in the determination of the spectral densities. The new CGenFF excitonic coupling regime in spectral density has been found to show higher excitonic coupling compared to the previous CHARMM FF. This proves the fact that the FF sets differ by FF method employed rather than FF parameters. Since BChl *a* complex is various in other LH systems too. Probably in near future the current CGenFF parameters can be employed to study the excitonic properties for various other systems.

Chapter 4

Protein Arrangement effects the Exciton Dynamics in the PE555 Complex

[0]I have done all the quantum calculations and molecular dynamics simulations and written part of the manuscript.

Abstract

The environmental coupling of the phycobiliprotein antenna complex PE555 and its excitonic energy transfer mechanisms are studied in detail. Molecular dynamics simulations were performed followed by calculations of the vertical transition energies along the classical ground-state trajectory. To this end, the distributions of energy levels for the PE555 complex were found to be similar to those of the PE545 complex despite the clear differences in the respective protein structures. In the PE555 complex the two $\alpha\beta$ monomers are rotated by $\sim$73° compared to the PE545 structure leading to a water filled channel. Moreover, the connections between the bilins, which act as pigments in these aggregates, and the protein show clear differences in the two structures. Analyzing the coupling of the individual chromophores to the protein environment, however, yielded similar spectral densities in the two protein complexes. In addition, the partial transition charges of the involved bilins have been determined in order to calculate the electronic couplings using the transition charges from electrostatic potentials (TrESP) method. For comparison purposes, the couplings have been extracted using the point-dipole approximation as well. On average the coupling values predicted by the dipole approximation are slightly larger than those from the TrESP method leading to enhanced population decay rates as tested in ensemble-averaged wave packet dynamics. Moreover, the exciton dynamics in the PE555 structure is significantly slower than in the PE545 complex due to the smaller coupling induced by the dissimilar arrangements of the monomers.

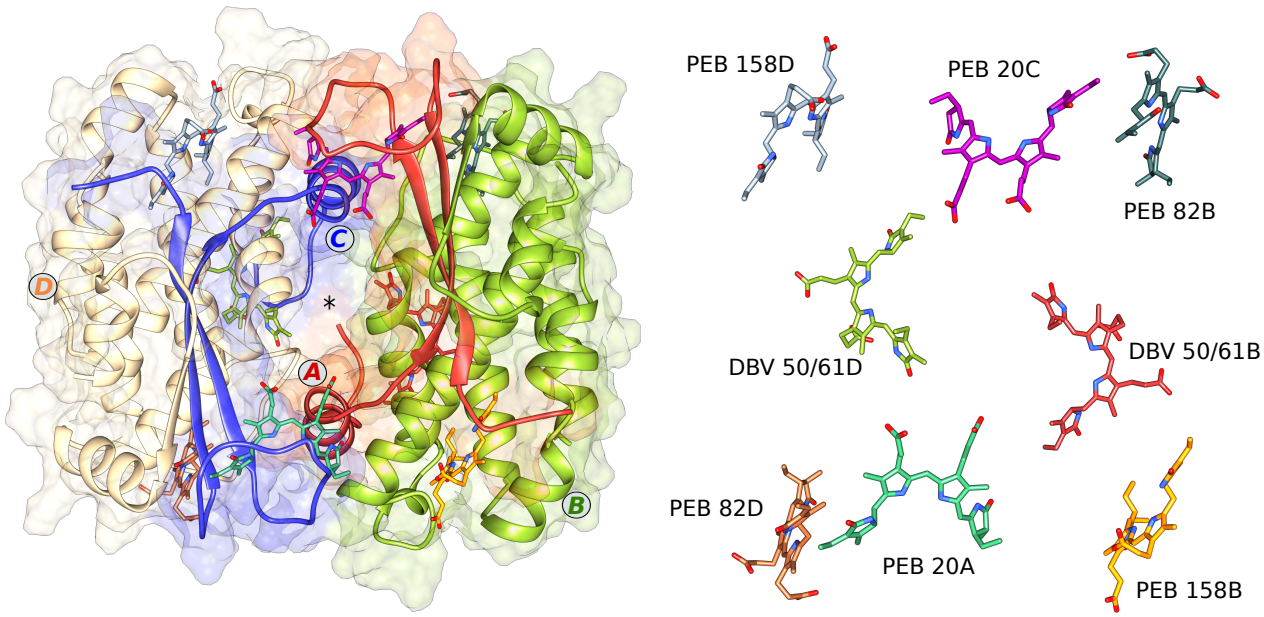

Figure 4.1: Structure of the PE555 complex with protein in cartoon representation and pigments shown in van der Waals spheres in the left panel. The asterisk sign indicates the position of the (water-filled) channel. The right panel depicts only the PEB and DBV bilins without the protein scaffold.

4.1 Introduction

While photosynthetic light harvesting sustains life on earth [2], understanding the molecular details of biological complexes might help to improve the design and efficiency of (organic) solar cells [10, 96]. Besides plants and bacteria [178], also some algae use light harvesting as their primary source of energy. Among these algae are the unicellular cryptophyte algae, which live in all kinds of aqueous habitats from marine, brackish, to freshwater. Recently the interest in the light-harvesting apparatus of these algae increased, after long-lived quantum coherence had experimentally been observed in the Phycoerythrin 545 (PE545) antenna of *Rhodomonas sp. CS24* marine algae [179, 180]. These experiments followed the seminal 2D experiments on the Fenna-Matthews-Olson (FMO) complex observing long-lived quantum coherent oscillations for the first time [28, 30, 93]. By now, electronic 2D spectra have also been obtained, for example, for the cryptophyte complexes PE555 and PC645[40, 181]. In addition, four-wave mixing, transient absorption and femtosecond stimulated Raman spectroscopy experiments have been performed to record ground- and excited-state coherences in different cryptophyte proteins [182, 183].

Cryptophyte algae come in different colors stemming from a remarkable range of chemical

versatile pigments called bilins[6, 184]. A large variety of different compositions and chromic variations exists in cryptophycean phycobilin proteins. Among them are the phycoerythrins PE545, PE555, and PE566 as well as the phycocyanins PC569, PC577, PC612, PC630 and PC645 [6, 185–189]. The naming is according to the position of the absorption maximum of the native protein in units of nm. All these phycobilin proteins consist of two so-called α and β subunits, i.e., four subunits in total. In the present study we focus on the phycoerythrins and more specifically on PE555 which has quite some similarities with PE545. For both complexes crystal structures exist, i.e., for PE545 from *Rhodomonas sp. CS24* [190] and PE555 from *Hermiselmis andersenii* [40]. The structure of PE545 consists of 4 subunits (A, B, C and D) forming a dimer of two $\alpha\beta$ monomers where the β subunits contain three phycoerythrobilins (PEBs) β50/61 (PEB 50/61B, 50/61D), β82 (PEB 82B, 82D) and β158 (PEB 158B, 158D) and the α part one dihydrobiliverdin, DBV, denoted α20 (DBV 20A, 20C). Responsible for the respective names are the cysteine residues to which the bilins are covalently linked. The PE545 aggregate is in the so-called "closed" form in which the two central β50/61 are in physical contact. As shown in Fig. 4.1 for the PE555 complex, however, the two central β50/61 pigments are separated by a water-filled channel and the two $\alpha\beta$ monomers are rotated by $\sim$73°[40]. Moreover, in case of the PE545 complex all bilins in the β subunits are PEBs and the one pigment in the α subunit is a DBV, while in case of the PE555 protein the β50/61 pigment is a DBV and the other three are PEBs [40]. A slightly more subtle difference is in the bonding pattern of the bilins to the α and the β50/61 positions of the proteins [6, 187]. The pigments are singly connected to the α subunits, while doubly connected to the β50/61 position in both cases. This finding is independent of the kind of bilin connected to either the α or β50/61 positions. Furthermore, the PEBs at the two other β positions are always singly connected.

For the FMO complex, a huge number of theoretical studies is present (see, for example, Ref. 75, 86, 108, 111, 123, 132, 159). The number of investigations on cryptophyte proteins is much smaller, however. The respective calculations have so far concentrated on the PC645 and PE545 complexes. In case of PC645, absorption and fluorescence spectra were modeled based on the available structure [191]. Later on, these results on the system Hamiltonian together with an estimate of the spectral density, i.e., the coupling to the protein environment, were employed in density matrix calculations to model the excitation energy transfer [181, 192]. Moreover, a semi-classical exciton transfer theory has been applied to this complex [193]. At the same time, the PE545 complex has been investigated putting a larger emphasis on the coupling between exciton transfer and environmental modes. To this end, molecular dynamics (MD) simulations have been performed on the aggregate followed by QM/MM calculations of the excitation energies including polarization effects [194]. Subsequently, possible spatial

correlations were studied [114]. Furthermore, spectral densities have been determined for this complex using a combination of MD simulations and QM/MM calculations [98, 115] as well as the respective exciton dynamics [162, 195]. Aim of the present study is to compare the results for spectral densities and exciton dynamics of the PE555 structure with those of the similar but different PE545 complex.

4.2 Details of the classical, QM/MM and dynamical simulations

As described earlier for similar systems in more detail [86, 98, 116, 120, 161], the present study started with a MD simulation of the PE555 complex (PDB ID code 4LMX [40]) solvated in TIP3P water. The AMBER parm99SB [58, 196] force field was employed for the protein while the force field for the bilins were constructed using GAFF [154]. These force fields have already been employed in the case of the previous study of the PE545 complex [98] though some of them had to be slightly modified due to the different connectivities to the surrounding protein. The system was equilibrated for 12 ns at 300 K and 1 atm using NAMD [125]. Subsequently, a constant volume run of 720 ps was performed in which the atomic coordinates were stored every 2 fs. This procedure lead to a total of 360.000 stored frames. Using a larger time step between the saved frames would lead to inaccuracies in the high-frequency regime of spectral densities [89].

As previously done for the PE545 complex to which we want to compare our present results, the energy gap between the ground and first excited state of the bilins were determined along the MD trajectory. Thus, we performed a ground-state MD with non-polarizable force fields and calculated the excited state long this trajectory using the ZINDO/S-CIS approach (Zerner Intermediate Neglect of Differential Orbital method with parameters for spectroscopic properties together with the configuration interaction scheme using single excitations only) [119]. Although this semi-empirical approach has its limitations, we have recently shown that its results along a trajectory compare reasonably well to TDDFT calculations[161]. In the calculations of the vertical energies every bilin is treated separately within a QM/MM approach, i.e., the environment is taken into account by including all the partial charges in the force field. To this end, we employed the ORCA code [126] which has the scheme outlined in Ref. 197 implemented. Before each QM/MM calculation, we do actually move the respective bilin into the center of the simulation box since the MD part employs periodic boundary conditions but not the QM/MM calculations.

The excitonic coupling between the pigments is determined with two different approaches in the present study. As, for example, in the Förster approach describing exciton dynamics, the coupling can be assumed to be dominated by the Coulomb interaction and calculated using the point-dipole approximation (PDA). The necessary dipole moments are taken from the above described ZINDO/S-CIS calculations. To account for the charge distributions in a more detailed way, we also employed the TrEsp method (where TrEsp stands for transition charges from electrostatic potentials) [198, 199]. The transition densities have been determined in configuration interaction singles CIS/6-31g in vacuum using *Gaussian 09* [172]. These calculations and results for the transition dipole moments are quite similar to those in Ref. 200 and also in Ref. 201 which includes environmental effects in the polarizable continuum method (PCM). Subsequently, the TrEsp charges have been extracted using version 3.3.8 of the program package *Multiwfn* [202] and are listed in Tab. S1. To account for environmental screening effects in the present study, we applied a constant screening factor of $f = 0.69$ to both PDA and TrEsp couplings [199].

One main result of the present study are spectral density calculations. These results can subsequently be employed in density matrix propagation schemes [203, 204] to determine the exciton dynamics or in ensemble averaged wave packet approaches [107, 120]. In the proper limit, the density matrix and ensemble averaged wave packet approaches do, of course, lead to the same results [89]. In the latter approach, the time-dependent Schrödinger equation is solved for the fluctuating Hamiltonian with the time divided into short time intervals during, which the Hamiltonian can be assumed to be constant. In the present calculations the length of the time intervals with constant Hamiltonian coincide with the time step of saving MD conformations. Assuming that these time intervals are short enough, this scheme yields the solution of the time-independent Schrödinger equation. To this end, the exciton dynamics can be determined assuming that the excitation was initially localized on one of the sites. Moreover, the calculation of this exciton dynamics was repeated many times with different starting positions along the MD trajectory and then averaged to yield an approximation of the ensemble average. This procedure is possible since the time for the exciton dynamics of a few ps is much shorter than the available trajectory length of 720 ps.

4.3 Energy and coupling distributions

Representative pieces of the excitation energy gaps, also called site energies, along the MD trajectory are shown in Fig. 4.2. Clearly visible are the fast oscillations on a roughly 20 fs

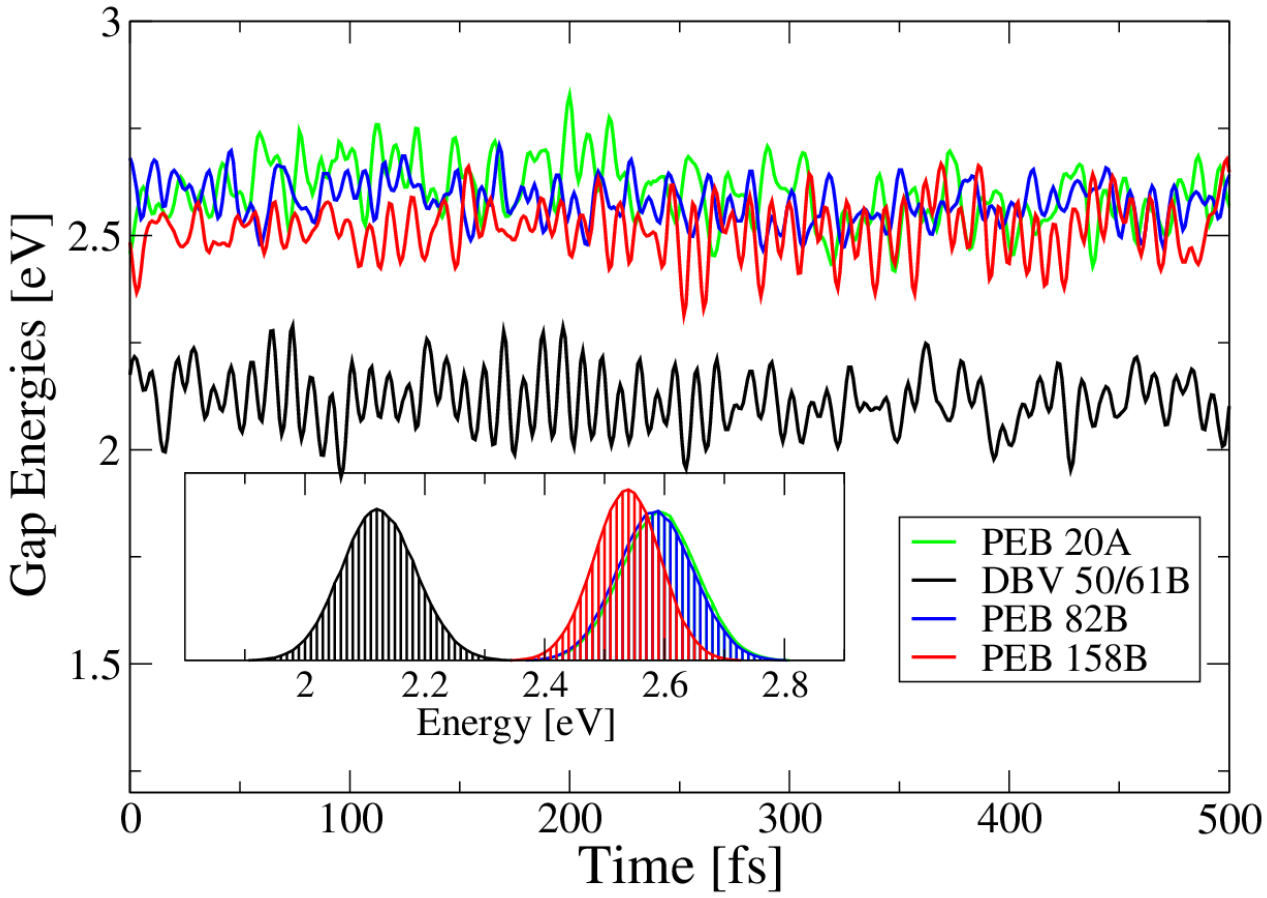

Figure 4.2: Representative piece of the excited energy trajectories together with the respective distributions of energy levels (DOS).

time scale as well as the separation between the DBV energies from the PEB ones. This becomes even more apparent if one looks at the distribution of states (DOS) or energy levels as depicted in the inset. Actually, the other four pigments behave very similar, i.e., there is a splitting between the DBV and PEB DOS. This feature has already been observed in earlier studies on the PE545 complex [98, 162, 194]. Furthermore, the widths of the site energy DOS are very similar to those in the PE545 complex for the corresponding pigments. The average peak position of the pigments is actually not much different when comparing the PE545 and PE555 aggregates.

As described in the previous section, the excitonic couplings are determined in two different ways: the PDA approach with transition dipole moments from the ZINDO/S-CIS calculations and the more detailed and elaborate TrEsp scheme based in the present case on

Table 4.1: Transisiton dipole moments based on ZINDO/S-CIS for PDA and on CIS/6-31G for TrEsp averaged along the MD trajectory in units of Debye.

site	1	2	3	4	5	6	7	8	average
pigment	PEB 20A	DBV 50/61B	PEB 82B	PEB 158B	PEB 20C	DBV 50/61D	PEB 82D	PEB 158D	
ZINDO/S	10.31	13.87	10.59	10.31	10.16	13.69	10.49	10.26	11.21
CIS/6-31G	9.375	12.678	9.290	9.573	9.672	11.603	9.376	9.728	10.16

CIS/6-31g partial transition charges. Important properties concerning the coupling determinations are the transition dipole moments of the individual pigments which enter the PDA expression directly and can be constructed from the partial TrEsp charges as well. These values are given in Tab. 4.1. For the PDA approach, the average magnitude of the transition dipole of 11.21 D is almost identical to the experimental value of 11.25 D reported in Doust et al. [205]. In case of the TrEsp scheme this average is about 10 % lower with a value of 10.16 D which is still very reasonable and therefore we decided against a rescaling of the TrEsp charges. Theoretical transition dipole values reported earlier [200, 201] are rather similar depending on the details of the calculations. Moreover, including environmental effects through the PCM approach did not lead to a significant large change of these values.

The obtained distributions for the excitonic couplings between the bilins is shown in Fig. 4.3 for both the PDA and the TrEsp schemes. As is clearly visible, the distributions for the PDA approximation are broader than those of the TrEsp method. The partial transition charges for the TrEsp scheme are calculated once while they were projected onto the atomic position along the MD trajectory. Thus, these partial transition charges are frozen in time as is also the case for electrostatic partial charges in MD simulations. The TrEsp scheme has been tested extensively in several studies, for example, recently in Refs. 206 and 207. For large distances, the PDA results converge to those of the TrEsp approach if the underlying method for the charge determination is the same. As can be seen in Fig. 4.3, the average peak positions for the same coupling in the two approaches lie close while the distributions are broader in case of the PDA coupling. Only for the 2-6 coupling a large discrepancy between PDA and TrEsp values are found. In this case the PDA coupling between the two bilins DBV 50/61B and DBV 50/61D is found to be six times higher than the TRESP value showing that for certain configuations the PDA approximations is rather poor [198]. Interestingly, a similar large coupling is also observed in the case of the PE545 complex. In this protein the coupling between the PEB 50/61C and PEB 50/61D is found to be 10.625 meV within the PDA approximation (see Tab. S2). No TrEsp data is yet available for that complex. In both, the PE545 and the PE555 complex, the rather high coupling values are present between the two central pigments .

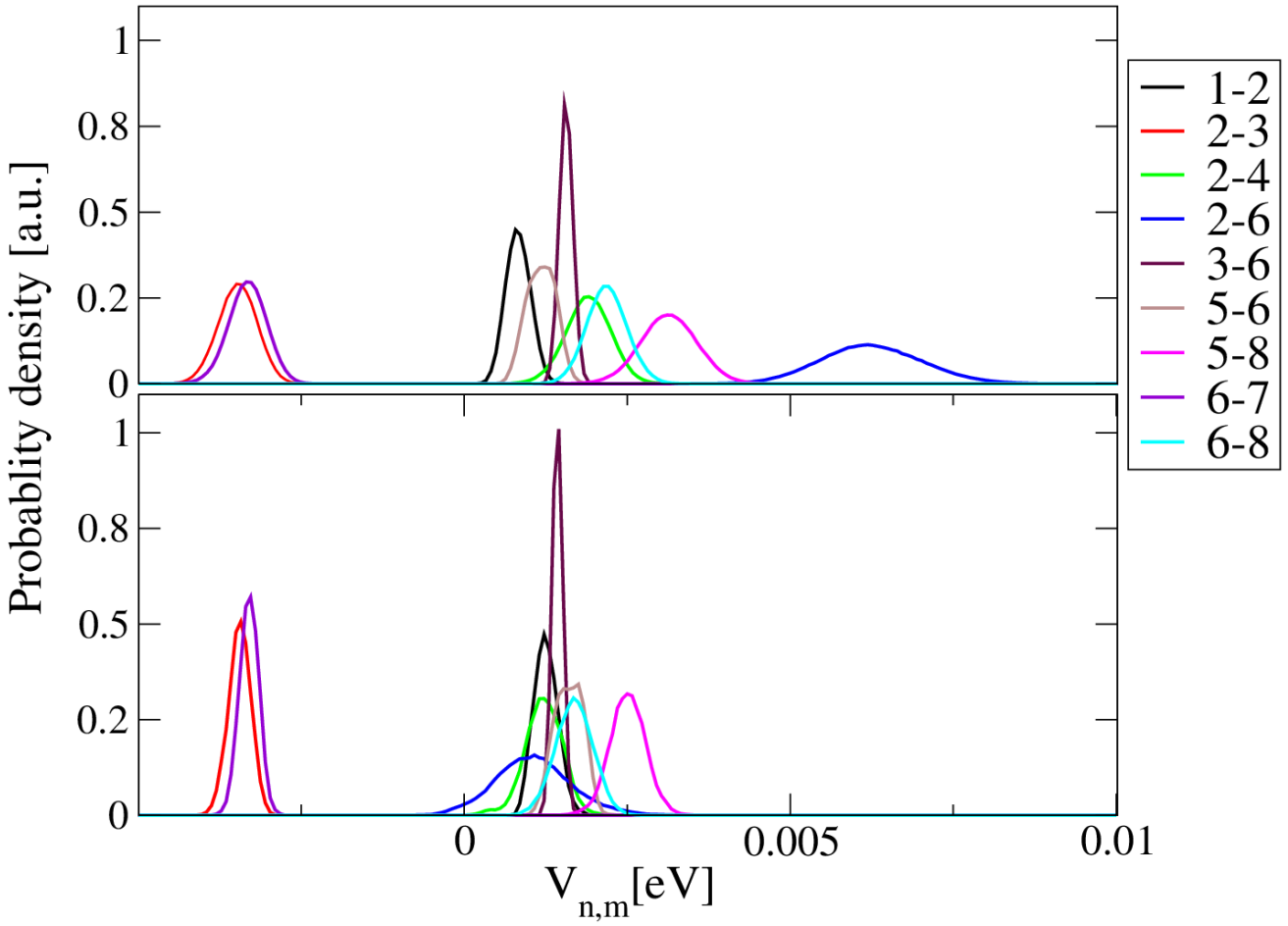

Figure 4.3: Distributions of couplings from the PDA (top) and TrEsp (bottom) methods.

The average values for the couplings are shown in Tab. 4.2 together with the site energies. These values can, for example, be employed in a density matrix propagation describing the exciton dynamics within the single-exciton manifold. The average values of the couplings for the PE555 are clearly smaller than those in the PE545 aggregate employed in Ref. 162 for the exciton dynamics and listed for completeness in the present supplementary material. Moreover, Harrop et al. [40] predicted the excitonic coupling for the PE555 complex using the Transition Density Cube Method [208] at the CIS/cc-pvtz level. Those data are listed in Tab. S3 using the present pigment enumeration and an environmental scaling factor of $f = 0.69$ for a better comparison with the present results. Qualitatively, there is a large degree of agreement with our results especially on the ordering and signs of the couplings. The values do, however, vary with the findings by Harrop et al. [40] having a larger magnitude in many cases. Part of the discrepancies might stem from the fact that our values are averaged

Table 4.2: Time-averaged Hamiltoninan with the site energies on the diagonal including the shifts for the DBV pigments. The upper off-diagonal triangle is given by the TrEsp coupling while the lower off-diagonal triangle shows the PDA couplings. The coupling values are given in units of meV.

site	1	2	3	4	5	6	7	8
1	**2.317**	1.215	0.895	2.243	-0.902	-0.885	0.804	0.303
2	0.778	**2.222**	-3.481	1.176	-0.669	1.026	1.423	0.199
3	0.925	-3.523	**2.293**	0.597	-0.415	1.394	0.267	0.211
4	3.045	1.850	0.621	**2.341**	0.314	0.231	-0.004	0.199
5	-0.971	-0.218	-0.552	0.247	**2.346**	1.565	0.990	2.471
6	-0.517	6.201	1.513	0.269	1.130	**2.248**	-3.336	1.646
7	0.610	1.521	0.290	-0.064	1.010	-3.317	**2.267**	0.599
8	0.227	0.249	0.194	0.201	3.088	2.138	0.609	**2.332**

of the MD trajectory while the data by Harrop et al. [40] is based on a single structure, i.e., the crystal structure.

4.4 Spectral densities

Other than the average Hamiltonian, a key ingredient for density matrix calculations is the so-called spectral density [107]. These have previously been determined for complexes like LH2 [107, 120], FMO [104, 109] and PE545 [98, 115]. To this end, one first needs to determine the autocorrelation functions $C_j(t)$ for pigment j based on the energy gaps $\Delta E_j(t_i)$ at time steps t_i. The energy gap autocorrelation function for pigment j is defined as[107]

$$C_j(t_i) = \frac{1}{N-i} \sum_{k=1}^{N-i} \Delta E_j(t_i + t_k) \Delta E_j(t_k) \ . \tag{4.1}$$

To be able to properly compare the PE545 and the PE555 spectral densities, exactly the same parameters have been employed to extract the spectral densities. So the autocorrelation functions were calculated over time lengths of 2 ps. For this purpose trajectory pieces of 4 ps length are necessary. The autocorrelation functions of the 180 trajectory pieces (720 ps divided into 4 ps pieces) are averaged and an exponential cut-off function for the auto-correlation function is used with a damping range of 1 ps for each sampling. Based on these auto-correlation functions, the spectral density $J_j(\omega)$ of pigment j can be determined using[99, 109]

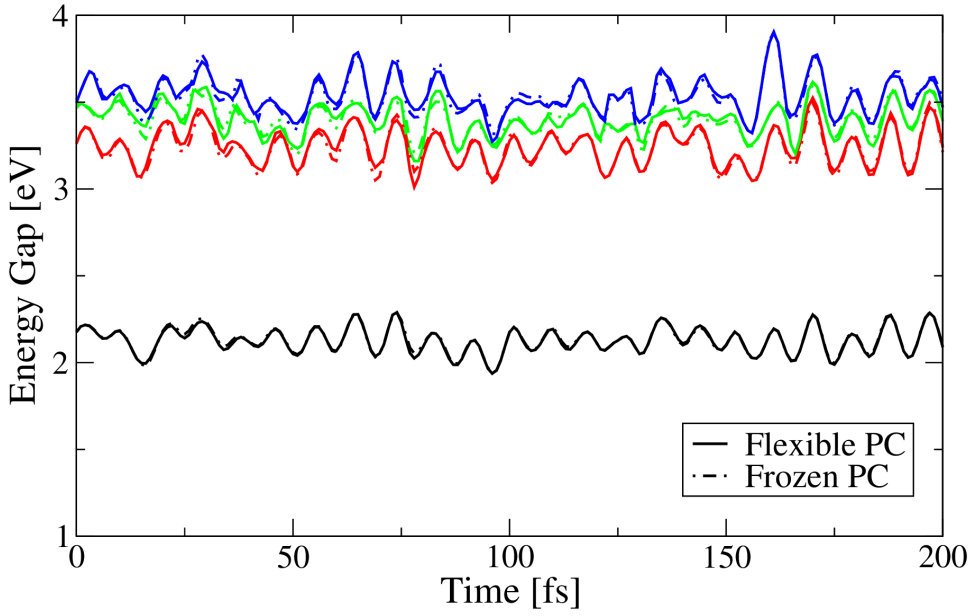

Figure 4.4: An example segment of the energy gap trajectories for the DBV 20B pigment is shown. The two variants refer to the same MD trajectories with full QM/MM coupling (flexible PC) and with frozen environmental point charges (frozen PC).

$$J_j(\omega) = \frac{\beta\omega}{\pi} \int_0^\infty \mathrm{d}t\, C_j(t) \cos(\omega t) \tag{4.2}$$

where $\beta = 1/(k_B T)$. We like to mention that for consistency reasons we used the high-temperature limit $\beta\omega/\pi$ of the prefactor instead of $2\tanh(\beta\hbar\omega/2)/\pi\hbar$ as employed in some previous studies [86, 107, 120]. This classical high-temperature limit has been shown by Valleau et al. [109] to yield more consistent results especially concerning the temperature-independence of spectral densities. At the same time, the choice of the pre-factor affects only the high-frequency regime of the spectral densities.

As in the case of FMO and PE545, our aim is to analyze the effects of the environmental fluctuations on the spectral densities. Therefore, spectral densities have been extracted from two different QM/MM calculations. In the first case, standard QM/MM calculations are performed with the QM part constituting of the respective bilin and using the time-dependent positions of the partial charges of the environmental atoms. In the second case, however, the positions of the environmental charges are kept fixed to those of the first frame

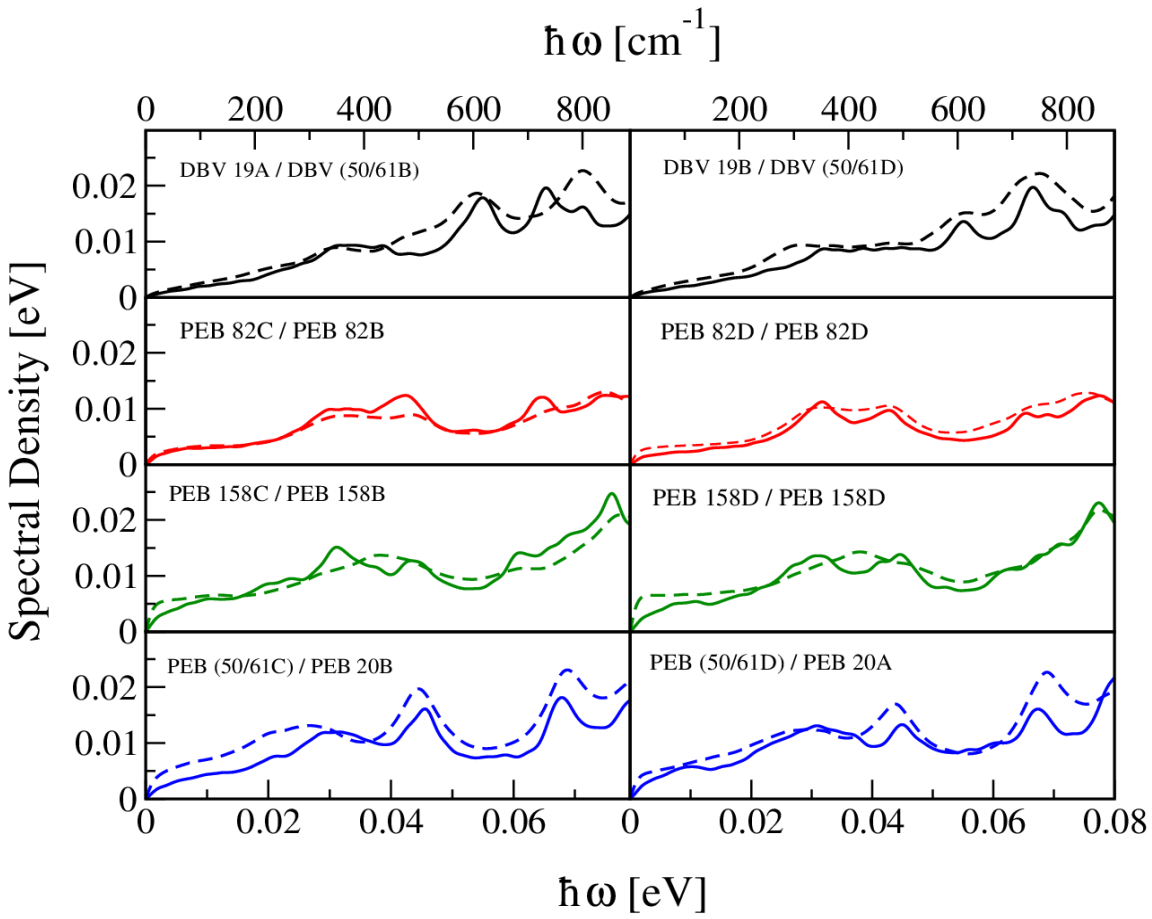

Figure 4.5: Spectral densities of the individual pigments in the PE555 complex (solid lines) compared to those of the respective bilins in the PE545 structure (dashed lines).

of the MD trajectory, i.e., the environmental fluctuations are frozen out. A representative piece of a trajectory is shown in Fig. 4.4. As in the case of PE545 [98], differences between the calculations with flexible and frozen environment are hardly visible. The results for the spectral densities with fluctuating and with frozen point charges are shown in Fig. S1. As already found for the similar PE545 complex [98] with the same pigments, there is almost no difference between the spectral densities with and without environmental fluctuations. Thus, the spectral densities almost completely result from intermolecular vibrations of the pigments [98].

Certainly it is very interesting to compare the spectral densities for the bilins in the PE545 and the PE555 complexes. Here one has to keep in mind that some of the DBV and PEB bilins traded places between the two proteins. Moreover, and as discussed in the Introduction, in PE555 the bonding pattern of the bilins to the α and the β50/61 positions of the proteins

[6, 187] is changed. The pigment is singly connected to the α subunit, while doubly connected to the β50/61 position in both cases. The PEBs at the two other β positions are always singly connected. When comparing the bilins from the two rather similar complexes, we do compare DBVs and PEBs with each other and if possible those at the same position. As can be seen in Fig. 4.5 in such a comparison, the respective pairs do show very similar spectral densities. In fact, it is impossible to state if the differences are statistically significant or simply are due to finite trajectory length or insufficient equilibration of the complex. The similarity between the spectral densities is not surprising since, as shown above, these are very insensitive to the environment. The largest difference might actually result from the different bonding pattern.

To compare spectral densities for different complexes in a more approximate fashion, one can also determine a spectral density averaged over all pigments of an individual complex. Such a comparison for the calculated spectral densities of PE555, PE545, FMO and an experimental spectral density is shown in Fig. S2. In such a plot the PE555 and PE545 spectral densities are very similar and differ only in peak heights especially at the largest frequency. Therefore, the same discussion as in Ref. 98 holds true.

4.5 Exciton Dynamics

Based on the above results, one could either use the average Hamiltonian together with the spectral densities or an ensemble-averaged wave packet dynamics scheme to obtain the exciton dynamics in the PE555 complex. Those two approaches do lead to the same results in certain limiting cases but do usually involve different approximations [89]. Before performing the wave packet dynamics, we have shifted the PEB and DBV pigment site energies by -1500 cm^{-1} and $+750$ cm^{-1}, respectively. For the exciton dynamics only the relative shift between the two bilin types actually matters. The shift is the same as already introduce in case of PE545 [162] due to the inaccuracy of the ZINDO/S-CIS approach to properly reproduce optical spectra. Shown in Fig. 4.6 are the wave packet dynamics for an exciton, which is initially located at one of the eight pigments. All eight different cases are actually displayed. The dynamics is shown up to a time of 6 ps at which the population has considerably relaxed but equilibrium is not reached yet. At the same time, we need to mention that the employed schemed of ensemble-averaged wave packet dynamics includes an implicit high-temperature limit, which leads to an equal population of 0.125 for all 8 sites at equilibrium which is non-physical by itself.

It is evident that the open structure of PE555 resulted in smaller couplings compared to

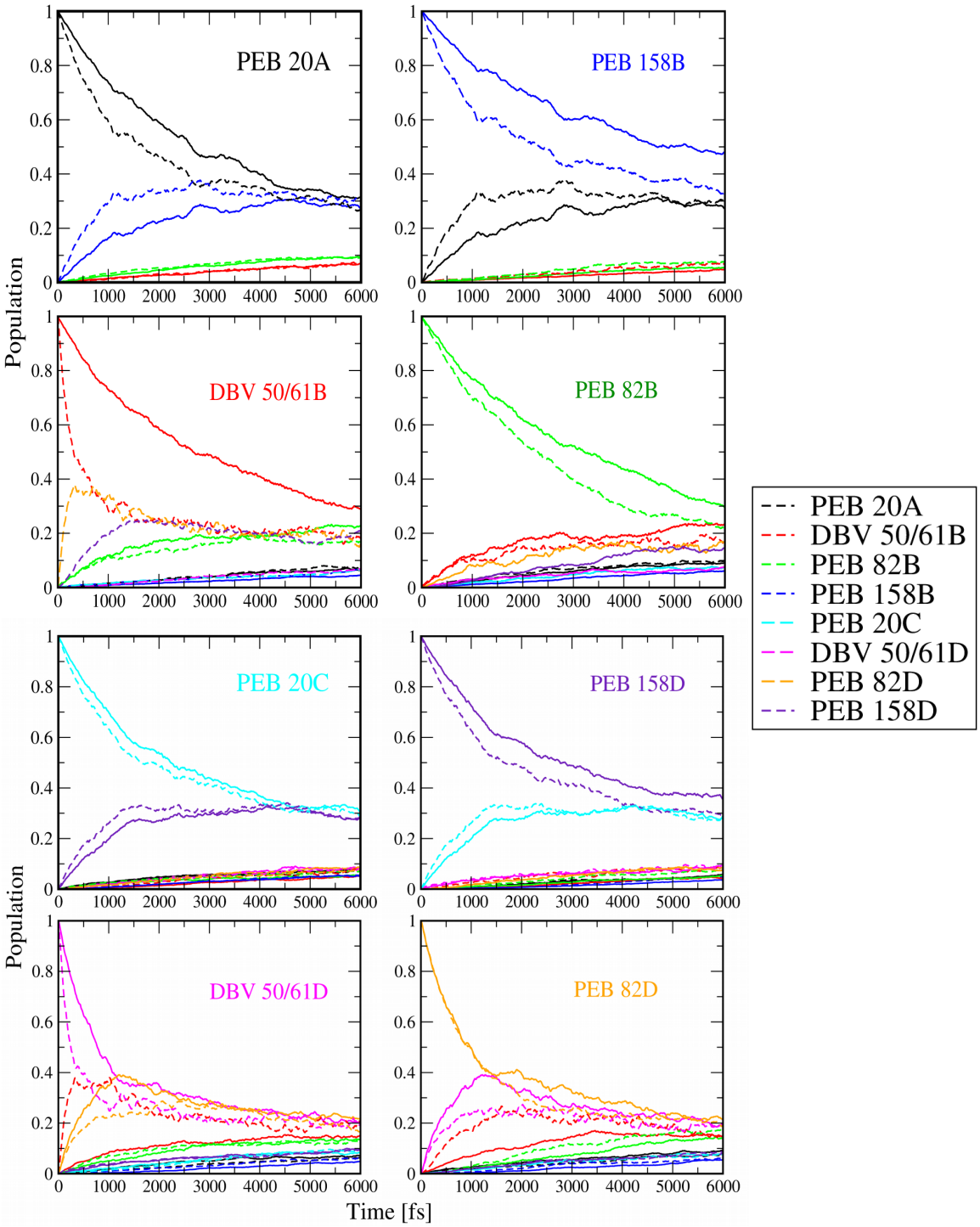

Figure 4.6: Exciton transfer dynamics with excitons starting at the respective pigment. The solid lines refers to calculations employing the TrEsp couplings while dynamics with the PDA couplings is shown by the dashed lines.

PE545 and therefore larger times to reach the thermal equilibrium. As can be seen in Fig. 4.6 in case of PE555 this time is larger than 6 ps while in the PE545 complex this value is of the

order of 2 ps [162]. In the present case, the population dynamics based on the PDA couplings reaches equilibrium faster due to the slightly larger coupling values given in Tab. 4.2. Using the PDA coupling both DBV pigments reach the equilibrium state on a similar time scale which is shorter that those of the PEB bilins. Because of smaller coupling values in the TrEsp approach, however, some couplings are smaller and the DBV 50/61B pigment shows a larger decay time. The realtive short decay times of the DBV pigments is mots likely due to their central location within the protein structure. Chromophores PEB 158B and PEB 158 D have the largest decay times which goes well beyond 6 ps. For some bilins like PEB 82B the populations decays simultaneously to all other pigments while for pigments like BV 50/61B or PEB 82D the excitation first decays mainly to one other molecule before than spreading onto all pigments.

4.6 Discussion and Conclusions

While the PE545 complex has been studied to some extend [98, 114, 162, 194, 201, 209–211], much less is known about the similar but different aggregate PE555 [40]. The PE545 dimer is in what has been called a "closed" form, in which the two central β50/61 chromophores are in physical contact [40]. In the structure of the PE555, however, the $\alpha\beta$ dimer is rotated by $\sim$73° compared to the closed form and is in a so-called "open" conformation. This leads to a water-filled channel, which separates the central β50/61 chromophores. As has been shown previously for PE545 and confirmed here for PE555, the site energy fluctuations are quite insensitive to the external fluctuation leading to distributions of the site energies and to spectral densities which are quite similar in the two complexes. This finding also leads to the fact that the spectral densities of the individual pigments are quite comparable when taking into account that some of the DBV bilins have traded placed with PEB chromophores.

The different spatial arrangements of the pigments in the open structure PE555 and the closed structure PE545 leads, however, to altered distances and in turn changed coupling values. Several couplings are smaller in the PE555 than in the PE545 complex. A clear consequence of this finding is the much slower relaxation dynamics in the PE555 complex with more than 6 ps compared to 2-3 ps in the PE545 aggregate. Interestingly, this change in dynamics does affects all bilins in a rather similar way and not only, for example, the central β50/61 chromophore pair.

Beyond the presented analysis, the current data allows for extended calculations based on the time-averaged Hamiltonian, the spectral densities and/or the time-dependent Hamilto-

nian. Since the spectral densities are almost completely independent from the environmental fluctuation of the individual chromophore as has already discussed in more detail elsewhere [98, 162], these could be employed for other complexes involving the same pigments as well. The couplings, however, will have to be recomputed for each complex individually though for that purpose a calculation based on the crystal structure might be sufficient. The dynamical simulations, so far have been proven to be quite insensitive to the fluctuations in the couplings.

Summary

The aim of this thesis was to study the EET among LH pigments in photosynthetic bacteria since the transfer of excitation energy among the different LH pigments occurs at nearly 100 % efficiency. In this work ,the FMO and PE555 complexes was been studied in detail. The FMO is a homo trimeric complex in which each monomer contains 8 bacteriochlorophyll a (BChl a) a pigments. The PE555 aggregate is a phycobilin complex. It consists of 6 phycoerythrobilin (PEB) and 2 dihydrobiliverdin (DBV) LH pigments in four different protein chains. Experimental studies of both complexes have proven the existence of long-lived coherence [28, 190, 205]. Moreover, theoretical studies have been carried out to obtain an atomistic level understanding of EET mechanism in these LH complexes.

The EET among the pigments is studied using an open quantum system approach. In this formalism, the system of interest (pigments) was truncated from the environment to reduce the computational cost. In a later step, the effect of environment (protein, water and ions) is included. A QM/MM approach is used to calculate the vertical excitation energies of the individual chromophoric pigments. In this scheme, the LH pigments (BChl a, PEB and DBV) are treated at the QM level (ZINDO/S-CIS or TDDFT B3LYP/3-21G) and the rest of the system (protein, solvent, and ions) as MM point charges (partial charges from standard FF). A time-dependent Hamiltonian is then constructed from the site energies, fluctuations and excitonic couplings. The Hamiltonian at each point in time has site energies on the diagonal along with pigment-pigment couplings as off-diagonal element. Using an ensemble averaged wave packet approach, the population dynamics is obtained by solving the time-dependant Schrödinger equation. Furthermore, a spectral density analysis is carried out to calculate the frequency-dependent strength of system-bath coupling.

The spectral density analysis of the FMO complex has shown that the system and bath coupling varies with respect to the employed FF. The results of the AMBER FF together with the TDDFT B3LYP/3-21G approach for the vertical excitation energies has lead to a weaker coupling between the system and the environment. The CHARMM FF together wwith the

ZINDO (S/CIS) semi-emprical approach resulted in spectral densities for the system-bath coupling. A more detailed analysis was carried concerning the two different FF (CHARMM and AMBER) along with the two different quantum methods (ZINDO (S/CIS) and TDDFT B3LYP/3-21G). Two different FMO complexes extracted from two different bacterium *Prosthecochloris aestuarii* and *Chlorobaculum tepidum* were used for this comparative study. In a further step, using the different FF and quantum methods vertical excitation energy calculation were performed for both FMO complexes. The distribution of excitation energies (DOS) results predicted from the ZINDO (S/CIS) calculations compared to the CHARMM FF MD simulation has always shown broader non-Gaussian DOS. Interestingly, the cases with broader non-Gaussian DOS have always shown stronger system-bath couplings. However, neglecting the effect of the environment in all the different methods has shown very similar DOS and spectral densities. This result clearly shows that the environment has a major effect on the vertical excitation energies and thus the spectral densities and EET dynamics.

Since the previously parametrization procedure for a BChl a CHARMM FF differed from the actual CHARMM general force field (CGenFF) procedure, we have carried out the CGenFF procedure for parameterizing a BChl a molecule. During this process, the partial charges were obtained using QM interaction energies rather than electrostatic potential (ESP) charges. Moreover, the previous FF misses dihedral angles in several places. Subsequently, the new CGenFF has been tested for the FMO complex and an individual BChl a molecule in solution. The obtained spectral densities show a stronger system-bath coupling compared to those obtained from the previous CHARMM FF.

In a further part of the thesis, the PE555 complex containing PEB and DBV LH pigments was studied in detail using the same QM/MM method. The system was simulated using MD simulations with the AMBER FF and the vertical excitation energies have been predicted using the ZINDO (S/CIS) method. The DOS and spectral density analysis of the PE555 complex was performed with a special emphasis on the comparison to the PE545 LH complex. Both, the PE555 and PE545 complex, contain the same LH pigments but oriented in different ways inside the protein. The PEB and DBV LH pigments also differ by the way (single and doubly) they are connected to the proteins through cysteine units. However, the individual DOS and spectral densities for the individual pigments of the PE545 and PE555 complexes do not show significant differences. In a next step, the excitonic couplings among the pigments was obtained using the point dipole approximation (PDA) as well as the Transition Electrostatic Potential charges (TrEsp) method. Using Mulliken transition electrostatic potential charges (TrEsp), the TrEsp couplings are calculated between all PEB and DBV

pigments. Subsequently, ensemble-averaged wave packet dynamics has been used to solve the time dependent Schrdinger equation for both the PDA and TrEsp couplings. The population transfer among the PE555 LH pigments has shown longer time decays compared to those in the PE545 complex independent pf the way the excitonic coupling were determined. This finding might be due to the open protein structure of the PE555 complex containing water filled channel while the PE545 complex is in a closed form.

Based on the result in this thesis, further studies can be envisoned for other bilin systems like the phycobilisome protein (PC 577, PC 612) complexes. Further analysis needs to be performed with respect to the new CGenFF for BChl a molecules. This study can be extended to other LH complexes containing BChl a complex such as LH I, LH II etc.

Appendix A

Supplementary Information: Protein Arrangement effects the Exciton Dynamics in the PE555 Complex

Table A.1: Atomic transition charges in units of e for the PEB and DBV bilins in the PE555 determined at the CIS/6-31G level. Crystal conformations of the pigments were used in these calculations.

ATOM	PEB	ATOM	PEB		ATOM	DBV	ATOM	DBV
CHC	-0.007604	CGB	-0.005518		NA	-0.001165	CBD	-0.000366
NC	0.000448	O1B	-0.008180		C1A	-0.004601	OD	0.011788
C1C	-0.029030	O2B	-0.009209		C2A	-0.051241	HB1D	0.005102
C2C	0.076038	HM1D	0.000635		C3A	0.035503	HB2D	0.001588
C3C	-0.047024	HM2D	0.006942		C4A	-0.085456	HA1D	0.003632
C4C	0.075969	HM3D	0.006495		CMA	0.010343	HM1D	0.000445
CMC	0.004030	HND	-0.000232		CBA	0.002798	HM2D	0.006067
CAC	-0.018502	H1D	0.015331		OA	-0.072318	HM3D	0.006445
CBC	-0.011825	HCD1	0.024566		CHA	0.085508	HND	-0.000649
CGC	0.005940	HCD2	0.013382		CAA	-0.002405	H1D	0.012567
O1C	0.010661	HM1C	0.007880		NB	0.009970	HCD1	0.020485
O2C	0.020131	HM2C	0.007574		C1B	-0.099244	HCD2	0.012408
ND	-0.006555	HM3C	0.006404		C2B	0.065990	HM1C	0.007173
C1D	-0.005641	HA1C	0.016659		C3B	-0.049358	HM2C	0.006708
C2D	-0.005834	HA2C	0.025987		C4B	0.006835	HM3C	0.008957
C3D	0.014395	HB1C	0.008419		CHB	0.027024	HA1C	0.016711
C4D	-0.001490	HB2C	0.016107		CMB	-0.008026	HA2C	0.015338
CMD	-0.001649	HBC	0.008018		CAB	0.008424	HB1C	0.014518
CAD	-0.005467	HNB	-0.020764		CBB	0.001798	HB2C	0.008830
CBD	0.008041	HM1B	-0.007297		CGB	0.001547	HBC	0.009552
OD	0.010561	HM2B	-0.012983		O1B	-0.010168	HNB	-0.010389
NA	-0.002408	HM3B	-0.000546		O2B	0.006873	HA1B	-0.016880
C1A	-0.000367	HA1B	-0.029902		CHC	-0.005848	HA2B	-0.003532
C2A	0.002619	HA2B	-0.011819		NC	-0.001774	HB1B	-0.005213
C3A	0.011935	HB1B	0.000058		C1C	-0.012040	HB2B	0.004688
C4A	-0.041539	HB2B	-0.010502		C2C	0.060525	HM1B	-0.006802
CMA	0.002629	HAB	-0.027392		C3C	-0.035802	HM2B	0.005426
CBA	0.002063	HNA	-0.006160		C4C	0.061509	HM3B	0.020460
OA	-0.021909	HM1A	-0.004008		CMC	0.003987	HAB	-0.011099
CHA	0.033428	HM2A	-0.006163		CAC	-0.012876	HNA	-0.017657
CAA	0.005256	HM3A	-0.007272		CBC	-0.012872	HMA1	-0.016461
NB	0.011113	H2A	-0.009149		CGC	0.004453	HMA2	-0.017054
C1B	-0.078349	H3A	-0.015968		O1C	0.012043	HMA3	-0.021794
C2B	0.036019	HB1A	-0.010209		O2C	0.012219	HB1A	-0.012129
C3B	-0.043846	HB2A	-0.006113		ND	-0.005156	HB2A	0.005031
C4B	-0.034230	HB3A	0.007013		C1D	-0.006056	HB3A	-0.006653
CHB	0.042597	HA1A	-0.006065		C2D	-0.004787	HA1A	-0.004215
CMB	-0.000973	HNC	0.020559		C3D	0.006740	HNC	0.017756
CAB	0.014468	HB1D	0.000489		C4D	0.000626	HB3D	-0.015451
CBB	0.006829	HB2D	0.004457		CMD	-0.001293	-	-
HB3D	-0.012453	CAD	0.002477		-	-		

Table A.2: For comparions the site energies and PDA couplings for the PE545 complex (in meV) as determined in Ref. 98 and employed in Ref. 162.

sites	1 (DBV 19A)	2 (DBV 19B)	3 (PEB 158C)	4 (PEB 158D)	5 (PEB 50C)	6 (PEB 50D)	7 (PEB 82C)	8 (PEB 82D)
1	**2.232**	-	-	-	-	-	-	-
2	-0.479	**2.232**	-	-	-	-	-	-
3	2.566	0.354	**2.331**	-	-	-	-	-
4	0.327	1.992	0.385	**2.312**	-	-	-	-
5	0.006	-4.133	1.867	1.541	**2.411**	-	-	-
6	-4.115	0.174	1.589	2.132	10.625	**2.361**	-	-
7	1.245	3.664	0.547	-0.495	-2.862	1.417	**2.299**	-
8	3.444	1.272	-0.574	0.589	1.263	-2.820	-0.268	**2.237**

Table A.3: Excitonic couplings for the PE555 complex determined using the transition density cube approach at the CIS/cc-pvtz in meV units as reported by Harrop et al. [40]. For better comparison with the present results, the couplings have been multiplied with the constant environmental screening factor $f = 0.69$.

sites	1	2	3	4	5	6	7	8
1	-	-	-	-	-	-	-	-
2	1.73	-	-	-	-	-	-	-
3	1.45	-5.11	-	-	-	-	-	-
4	5.80	3.11	1.04	-	-	-	-	-
5	-1.10	0	2.48	0.43	-	-	-	-
6	-0.68	0.33	1.73	-0.17	1.10	-	-	-
7	2.21	2.07	0.36	0.35	1.38	-4.76	-	-
8	0.43	0.083	0.26	0.43	5.38	3.66	1.035	-

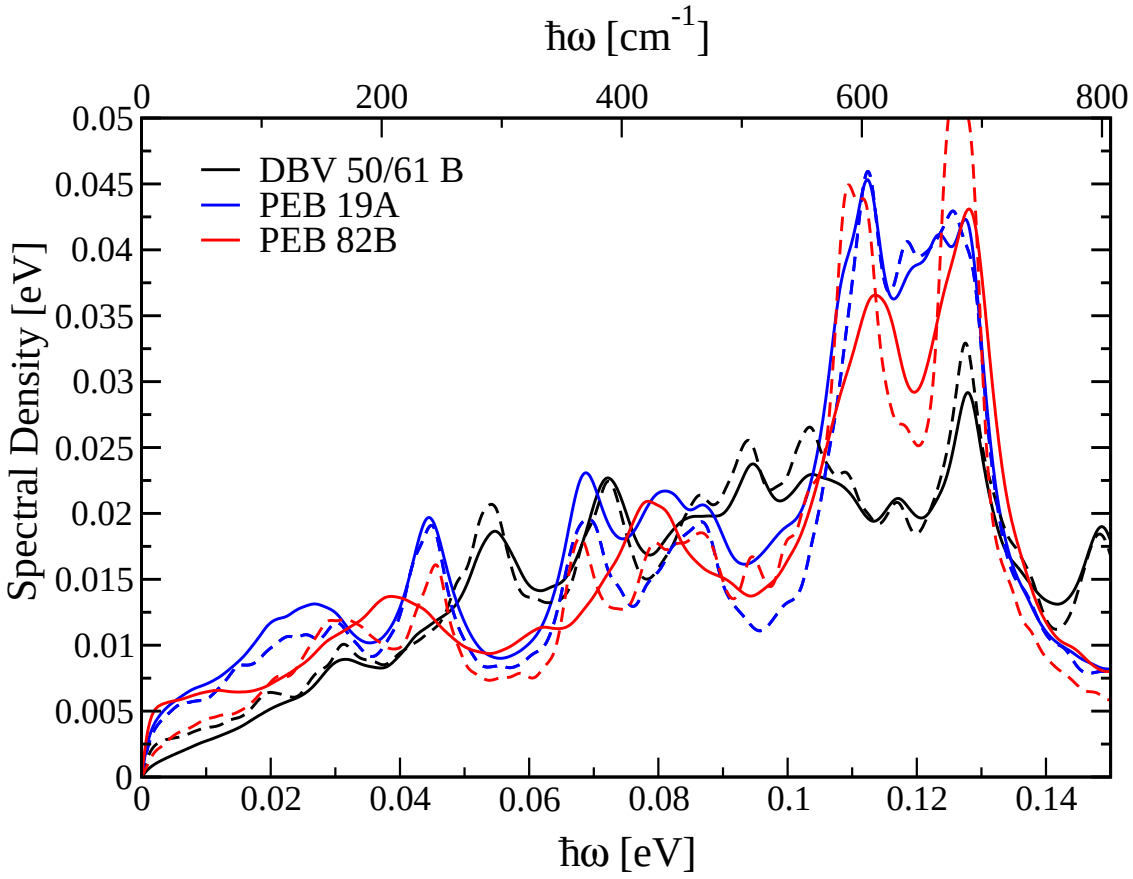

Figure A.1: Spectral densities of three bilins with full protein dynamics shown as solid lines. The dotted lines correspond to results with frozen environmental fluctuations.

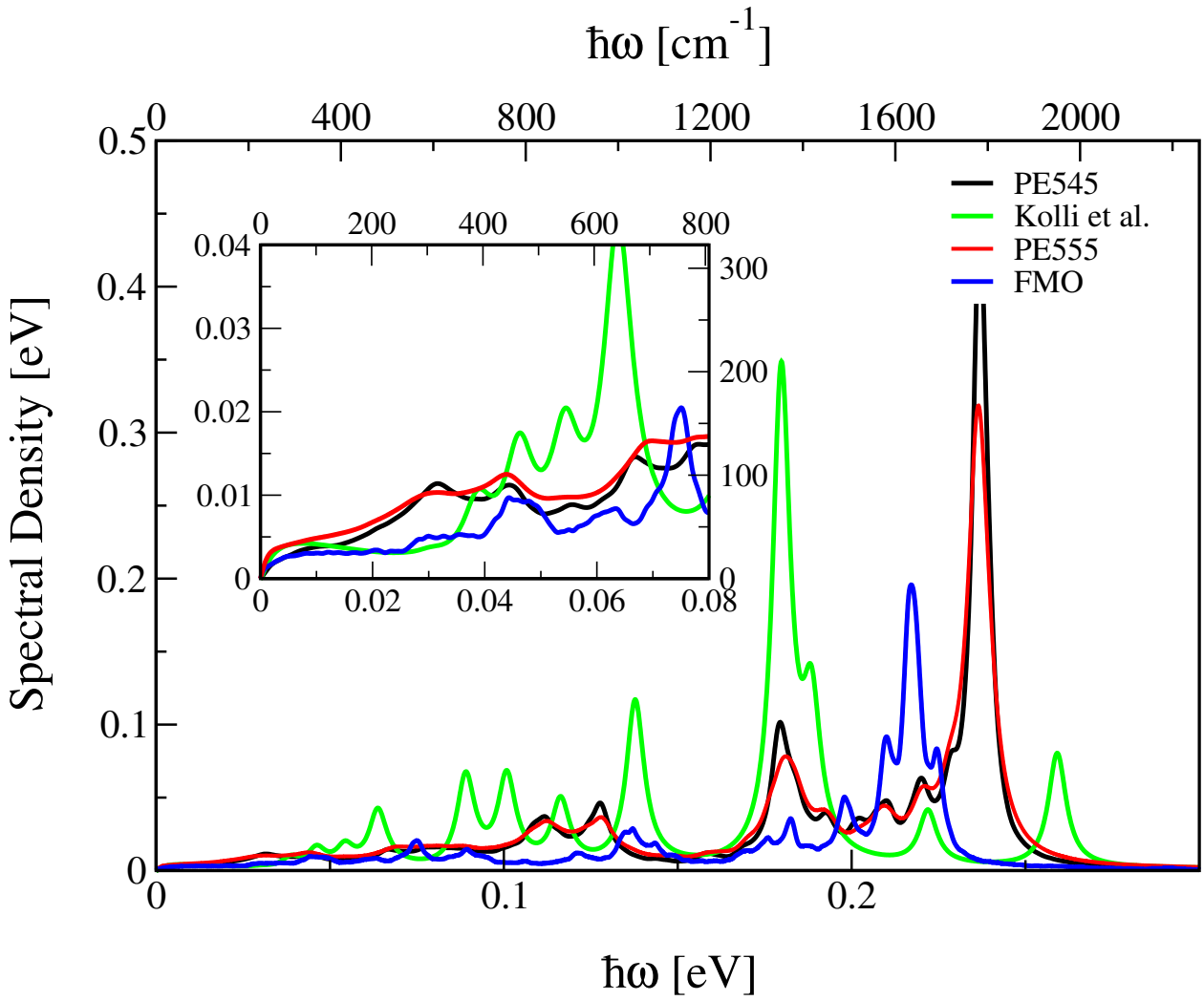

Figure A.2: Comparison of the average PE555 spectral density evaluated in the present study (red) with spectral densities for the PE545 complex from simulations[98] (black) and estimated from spectroscopic experiments[211]. In addition, an average FMO spectral density reported earlier [104] is given.

List of Tables

List of Figures

List of Publications

[7] Chandrasekaran, S.; Kleinekathfer, U. CHARMM general force field for Bacteriochlorophyll-a complex and FMO protein Complex. *Manuscript under preparation*.

[6] Chandrasekaran, S.; Pothula, K, R.; Kleinekathfer, U. Protein Arrangement effects the Exciton Dynamics in the PE555 Complex. *J. Phys. Chem. B* Manuscript accepted recently.

[5] Mallus, M. I.; Aghtar, M.; Chandrasekaran, S.; Lüdemann, G.; Elstner, M. & Kleinekathfer, U. Relation between Dephasing Time and Energy Gap Fluctuations in Biomolecular Systems. *J. Phys. Chem. Lett.* 7: 1102-1108, 2016.

[4] Chandrasekaran, S.; Aghtar, M.; Valleau, S.; Aspuru-Guzik, A. & Kleinekathfer, U. Influence of Force Fields and Quantum Chemistry Approach on Spectral Densities of BChl a in Solution and in FMO Protein.*J. Phys. Chem. B*, 119: 9995-10004, 2015.

Other Publication of the Author

[3] Suryanarayanan, C.; Prasannan, A.; Hong, P.-D.; Sambathkumar, B. & Somanathan, N. Variable temperature studies on mesogenic polythiophenes using 2D-IR and WAXS. *Materials Chemistry and Physics*, 143: 1352-1363, 2014.

[2] Suryanarayanan, C.; Sankaranarayanan, K.; Divakara, C. & Somanathan, N. Studies on the Langmuir-Blodgett films of polythiophene containing a mesogenic side chain. *RSC Adv.*, 4: 38341-38349, 2014.

[1] Suryanarayanan, C.; Ravindran, E.; Ananthakrishnan, S. J.; Somanathan, N. & Mandal, A. B. A molecular insight on the supramolecular assembly of thiophene polymers. *J. Mater. Chem.*, 22: 18975-18982, 2012.

e-link

Bibliography

[1] P. D. Boyer and W. E. Kohlbrenner, *The present status of the binding-change mechanism and its relation to ATP formation by chloroplasts*, in *Energy Coupling in Photosynthesis*, edited by B. R. . Selman and S. Selman-Reimer, 231–240 (Elsevier, Amsterdam, 1981).

[2] R. E. Blankenship, *Molecular mechanisms of photosynthesis* (Blackwell Science, Oxford, 2008).

[3] N. Pfennig, *Phototrophic Green and Purple Bacteria: A Comparative, Systematic Survey*, Annual Review of Microbiology **31**, 275–290 (1977), pMID: 410355.

[4] J. Deisenhofer, O. Epp, K. Miki, R. Huber and H. Michel, *Structure of the protein subunits in the photosynthetic reaction centre of Rhodopseudomonas viridis at 3 Å resolution*, Nature **318**, 618–624 (1985).

[5] J. Deisenhofer, O. Epp, K. Miki, R. Huber and H. Michel, J. Mol. Biol. **180**, 385 (1984).

[6] G. D. Scholes, T. Mirkovic, D. B. Turner, F. Fassioli and A. Buchleitner, *Solar light harvesting by energy transfer: from ecology to coherence*, Energy Environ. Sci. **5**, 9374–9393 (2012).

[7] R. M. Pearlstein and H. Zuber, *Antennas and Reaction Centers of Photosynthetic Bacteria* (Springer, Berlin, 1985).

[8] M. Marchi, J. N. Gehlen, D. Chandler and M. Newton, *Diabatic surfaces and the pathway for primary electron transfer in a photosynthetic reaction center*, J. Am. Chem. Soc. **115**, 4178–4190 (1993).

[9] M. A. Marquez, *Solar impulse 2 is closer to the round-the-world flight.* (2016).

[10] R. E. Blankenship, D. M. Tiede, J. Barber, G. W. Brudvig, G. Fleming, M. Ghirardi, M. R. Gunner, W. Junge, D. M. Kramer, A. Melis, T. A. Moore, C. C. Moser, D. G.

Nocera, A. J. Nozik, D. R. Ort, W. W. Parson, R. C. Prince and R. T. Sayre, *Comparing Photosynthetic and Photovoltaic Efficiencies and Recognizing the Potential for Improvement*, Science **332**, 805–809 (2011).

[11] D. Goswami and Y. Zhao, *Proceedings of ISES World Congress 2007 (Vol.1-Vol.5): Solar Energy and Human Settlement* (Springer Berlin Heidelberg, 2009).

[12] E. N. K. J. L. J. M. J. F. R. J. Kline, M. D. McGehee and M. F. Toney, *Dependence of Regioregular Poly(3-hexylthiophene) Film Morphology and Field-Effect Mobility on Molecular Weight*, Macromolecules **38**, 3312–3319 (2005).

[13] D. L. Cheung and A. Troisi, *Theoretical Study of the Organic Photovoltaic Electron Acceptor PCBM: Morphology, Electronic Structure, and Charge Localization*, J. Phys. Chem. C **114**, 20 479–20 488 (2010).

[14] Y. Zhao, Z. Xie, H. Gu, C. Zhu and Z. Gu, *Bio-inspired variable structural color materials*, Chem. Soc. Rev. **41**, 3297–3317 (2012).

[15] H. Wang and M. Pumera, *Fabrication of Micro/Nanoscale Motors*, Chemical Reviews **115**, 8704–8735 (2015), pMID: 26234432.

[16] P. T. Wong and S. K. Choi, *Mechanisms of Drug Release in Nanotherapeutic Delivery Systems*, Chemical Reviews **115**, 3388–3432 (2015).

[17] N. J. Halas, *Plasmonics: An Emerging Field Fostered by Nano Letters*, Nano Letters **10**, 3816–3822 (2010), pMID: 20853888.

[18] Danielle E. Chandler, Johan Strümpfer, Melih Sener, Simon Scheuring and Klaus Schulten, *Light Harvesting by Lamellar Chromatophores in Rhodospirillum photometricum*, Biophys. J **106**, 2503–2510 (2014).

[19] C. Suryanarayanan, E. Ravindran, S. J. Ananthakrishnan, N. Somanathan and A. B. Mandal, *A molecular insight on the supramolecular assembly of thiophene polymers*, J. Mater. Chem. **22**, 18 975–18 982 (2012).

[20] M. E. Cinar and T. Ozturk, *Thienothiophenes, Dithienothiophenes, and Thienoacenes: Syntheses, Oligomers, Polymers, and Properties*, Chemical Reviews **115**, 3036–3140 (2015), pMID: 25831021.

[21] Y.-J. Cheng, S.-H. Yang and C.-S. Hsu, *Synthesis of Conjugated Polymers for Organic Solar Cell Applications*, Chemical Reviews **109**, 5868–5923 (2009), pMID: 19785455.

[22] C. Suryanarayanan, K. Sankaranarayanan, C. Divakara and N. Somanathan, *Studies on the Langmuir-Blodgett films of polythiophene containing a mesogenic side chain*, RSC Adv. **4**, 38 341–38 349 (2014).

[23] G. D. Scholes, *Biophysics: Green quantum computers*, Nat. Phys **6**, 402–403 (2010).

[24] J. M. Olson, *The FMO Protein*, Photosynth. Res. **80**, 181–187 (2004).

[25] D. E. Tronrud, M. F. Schmid and B. W. Matthews, *Structure and X-ray amino acid sequence of a bacteriochlorophyll a protein from Prosthecochloris aestuarii refined at 1.9 A resolution*, J. Mol. Biol. **188**, 443–444 (1986).

[26] R. E. Fenna and B. W. Matthews, *Chlorophyll Arrangement in a Bacteriochlorophyll Protein from Chlorobium limicola*, Nature **258**, 573–577 (1975).

[27] J. Wen, H. Zhang, M. L. Gross and R. E. Blankenship, *Membrane orientation of the FMO antenna protein from Chlorobaculum tepidum as determined by mass spectrometry-based footprinting*, Proc. Natl. Acad. Sci. USA **106**, 6134–6139 (2009).

[28] G. S. Engel, T. R. Calhoun, E. L. Read, T. K. Ahn, T. Mancal, Y. C. Cheng, R. E. Blankenship and G. R. Fleming, *Evidence for wavelike energy transfer through quantum coherence in photosynthetic systems*, Nature **446**, 782–786 (2007).

[29] D. Hayes and G. S. Engel, *Extracting the excitonic Hamiltonian of the Fenna-Matthews-Olson complex using three-dimensional third-order electronic spectroscopy*, Biophys. J. **100**, 2043–2052 (2011).

[30] G. Panitchayangkoon, D. Hayes, K. A. Fransted, J. R. Caram, E. Harel, J. Wen, R. E. Blankenship and G. S. Engel, *Long-lived quantum coherence in photosynthetic complexes at physiological temperature*, Proc. Natl. Acad. Sci. USA **107**, 12 766–12 770 (2010).

[31] M. Schmidt am Busch, F. Müh, M. E. Madjet and T. Renger, *The Eighth Bacteriochlorophyll Completes the Excitation Energy Funnel in the FMO Protein*, J. Phys. Chem. Lett. **2**, 93–98 (2011).

[32] S. Huelga and M. Plenio, *Vibrations, quanta and biology*, Contemporary Physics **54**, 181–207 (2013).

[33] S. Valleau, S. K. Saikin, D. Ansari-Oghol Beig, M. Rostami, H. Mossallaei and A. Aspuru Guzik, *Electromagnetic Study of the Chlorosome Antenna Complex of Chlorobium tepidum*, ACS Nano **8**, 3884–3894 (2014), pMID: 24641680.

[34] P. J. Lockhart, A. W. Larkum, M. Steel, P. J. Waddell and D. Penny, *Evolution of chlorophyll and bacteriochlorophyll: the problem of invariant sites in sequence analysis*, Proceedings of the National Academy of Sciences **93**, 1930–1934 (1996).

[35] M. K. Şener, J. D. Olsen, C. N. Hunter and K. Schulten, *Atomic-level structural and functional model of a bacterial photosynthetic membrane vesicle*, Proc. Natl. Acad. Sci. USA **104**, 15 723–15 728 (2007).

[36] M. K. Şener, D. Lu, T. Ritz, S. Park, P. Fromme and K. Schulten, *Robustness and optimality of light harvesting in cyanobacterial photosystem I*, J. Phys. Chem. B **106**, 7948–7960 (2002).

[37] J. W. Weigl, *Concerning the Absorption Spectrum of Bacteriochlorophyll*, J. Am. Chem. Soc **75**, 999–1000 (1953).

[38] *The Porphyrin HandbooK* (Academic Press, Amsterdam, 2003).

[39] B. Krautler, *Phyllobilins - the abundant bilin-type tetrapyrrolic catabolites of the green plant pigment chlorophyll*, Chem. Soc. Rev. **43**, 6227–6238 (2014).

[40] S. J. Harrop, K. E. Wilk, R. Dinshaw, E. Collini, T. Mirkovic, C. Y. Teng, D. G. Oblinsky, B. R. Green, K. Hoef Emden, R. G. Hiller, G. D. Scholes and P. M. G. Curmi, *Single-residue insertion switches the quaternary structure and exciton states of cryptophyte light-harvesting proteins*, Proc. Natl. Acad. Sci. U. S. A. **111**, E2666–E2675 (2014).

[41] A. V. Akimov and O. V. Prezhdo, *Large-Scale Computations in Chemistry: A Bird's Eye View of a Vibrant Field*, Chem. Rev. **115**, 5797–5890 (2015).

[42] J. M. A. Blair, M. A. Webber, A. J. Baylay, D. O. Ogbolu and L. J. V. Piddock, *Molecular mechanisms of antibiotic resistance*, Nat. Rev. Micro. **13**, 42–51 (2015).

[43] R. Komanduri, N. Chandrasekaran and L. Raff, *Molecular dynamic simulations of uniaxial tension at nanoscale of semiconductor materials for micro-electro-mechanical systems (MEMS) applications*, Materials Science and Engineering: A **340**, 58 – 67 (2003).

[44] R.-l. Wu, T. Li and E. Nies, *Polymer networks by molecular dynamics simulation: Formation, thermal, structural and mechanical properties*, Chinese Journal of Polymer Science **31**, 21–38 (2013).

[45] B. J. Alder and T. E. Wainwright, *Studies in Molecular Dynamics. I. General Method*, The Journal of Chemical Physics **31**, 459–466 (1959).

[46] P. J. Dandliker, R. E. Holmlin and J. K. Barton, *Oxidative Thymine Dimer Repair in the DNA Helix*, Science **275**, 1465–1468 (1997).

[47] P. M. Agrawal, A. N. A. Samadh, L. M. Raff, M. T. Hagan, S. T. Bukkapatnam and R. Komanduri, *Prediction of molecular-dynamics simulation results using feedforward neural networks: Reaction of a C2 dimer with an activated diamond (100) surface*, The Journal of Chemical Physics **123**, 224711 (2005).

[48] R. Dutzler, E. Campbell, M. Cadene, B. Chait and R. MacKinnon, *X-ray structure of a ClC chloride channel at 3.0 Å reveals the molecular basis of anion selectivity*, Nature **415**, 287–294 (2002).

[49] X. Cheng, S. Jo, F. Marassi and W. Im, *NMR-Based Simulation Studies of Pf1 Coat Protein in Explicit Membranes*, Biophys. J. **105**, 691–698 (2016).

[50] J. Kapla, O. Engstrom, B. Stevensson, J. Wohlert, G. Widmalm and A. Maliniak, *Molecular dynamics simulations and NMR spectroscopy studies of trehalose-lipid bilayer systems*, Phys. Chem. Chem. Phys. **17**, 22 438–22 447 (2015).

[51] M. Griebel, S. Knapek and G. Zumbusch, *Numerical Simulation in Molecular Dynamics. Numerics, Algorithms, Parallelization, Applications* (Springer, Berlin, 2007).

[52] G. Zhao, J. R. Perilla, E. L. Yufenyuy, X. Meng, B. Chen, J. Ning, J. Ahn, A. M. Gronenborn, K. Schulten, C. Aiken and P. Zhang, *Mature HIV-1 capsid structure by cryo-electron microscopy and all-atom molecular dynamics*, Nature **497**, 643–646 (2013).

[53] Huilin Ma, Flaviyan Jerome Irudayanathan, Wenjuan Jiang and Shikha Nangia, *Simulating Gram-Negative Bacterial Outer Membrane: A Coarse Grain Model*, J. Phys. Chem. B **119**, 14 668–14 682 (2015), pMID: 26374325.

[54] C. J. F. Solano, K. R. Pothula, J. D. Prajapati, P. M. De Biase, S. Y. Noskov and U. Kleinekathöfer, *The BROMOCEA code: an improved grand canonical Monte Carlo/Brownian dynamics algorithm including explicit atoms*, Journal of Chemical Theory and Computation **12**, 2401–2417 (2016).

[55] P. M. De Biase, S. Markosyan and S. Noskov, *Microsecond simulations of DNA and ion transport in nanopores with novel ion-ion and ion-nucleotides effective potentials*, J. Comput. Chem. **35**, 711–721 (2014).

[56] J. W. Ponder and D. A. Case, *Force fields for protein simulations.*, Adv. Protein Chem. **66**, 27–85 (2003).

[57] A. MacKerell, D. Bashford, M. Bellott, R. Dunbrack, J. Evanseck, M. Field, S. Fischer, J. Gao, H. Guo, S. Ha, D. Joseph McCarthy, L. Kuchnir, K. Kuczera, F. Lau, C. Mattos, S. Michnick, T. Ngo, D. Nguyen, B. Prodhom, W. Reiher, B. Roux, M. Schlenkrich, J. Smith, R. Stote, J. Straub, M. Watanabe, J. Wiorkiewicz Kuczera, D. Yin and M. Karplus, *All-Atom Empirical Potential for Molecular Modeling and Dynamics Studies of Proteins*, J. Phys. Chem. B **102**, 3586–3616 (1998).

[58] V. Hornak, R. Abel, A. Okur, B. Strockbine, A. Roitberg and C. Simmerling, *Comparison of multiple Amber force fields and development of improved protein backbone parameters*, Proteins: Structure, Function, and Bioinformatics **65**, 712–725 (2006).

[59] L. Zhang, H. T. Davis and H. S. White, *Molecular Dynamics Simulations of Water in a Spherical Cavity*, J. Phys. Chem. **99**, 2878–2884 (1995).

[60] I. N. Levine, *Quantum Chemistry* (Prentice Hall, Englewood Cliffs, 1991), 4th edn..

[61] P. W. Atkins and J. de Paula, *Physical Chemistry* (Oxford University Press, Oxford, 2004), 7th edn..

[62] D. A. McQuarrie, *Quantum Chemistry* (Oxford Univ. Press, Oxford, 1983).

[63] F. Jensen, *Introduction to Computational Chemistry* (Wiley, West Sussex, 2007), 2nd edn..

[64] J. P. Perdew, J. A. Chevary, S. H. Vosko, K. A. Jackson, M. R. Pederson, D. J. Singh and C. Fiolhais, *Atoms, molecules, solids, and surfaces: Applications of the generalized gradient approximation for exchange and correlation*, Phys. Rev. B **46**, 6671–6687 (1992).

[65] W. Kohn and L. J. Sham, *Self-Consistent Equations Including Exchange and Correlation Effects*, Phys. Rev. **140**, A1133–A1138 (1965).

[66] M. Y. Amusia, A. Z. Msezane and V. R. Shaginyan, *Density Functional Theory versus the HartreeFock Method: Comparative Assessment*, Physica Scripta **68**, C133 (2003).

[67] A. Graczyk, J. M. Zurek and M. J. Paterson, *On the linear and non-linear electronic spectroscopy of chlorophylls: a computational study*, Photochem. Photobiol. Sci. **13**, 103–111 (2014).

[68] Y. F. Liu, J. Guan, D. Hu, L. Du, H. Sun, J. Gao, J. Zhao and Z. Lan, *Computational Investigation of Acene-Modified Zinc-Porphyrin Based Sensitizers for Dye-Sensitized Solar Cells*, J. Phys. Chem. C **119**, 8417–8430 (2015).

[69] E. Runge and E. K. U. Gross, *Density-Functional Theory for Time-Dependent Systems*, Phys. Rev. Lett. **52**, 997–1000 (1984).

[70] Z. Vokacova and J. V. Burda, *Computational Study on Spectral Properties of the Selected Pigments from Various Photosystems: Structure-Transition Energy Relationship*, J. Phys. Chem. A **111**, 5864–5878 (2007).

[71] O. Valsson, P. Campomanes, I. Tavernelli, U. Röthlisberger and C. Filippi, *Rhodopsin Absorption from First Principles: Bypassing Common Pitfalls*, J. Chem. Theory Comput. **9**, 2441–2454 (2013).

[72] D. Lee, L. Greenman, M. Sarovar and K. B. Whaley, *Ab Initio Calculation of Molecular Aggregation Effects: A Coumarin-343 Case Study*, J. Phys. Chem. A **117**, 11 072–11 085 (2013).

[73] S. Jurinovich, G. Pescitelli, L. Di Bari and B. Mennucci, *A TDDFT/MMPol/PCM model for the simulation of exciton-coupled circular dichroism spectra.*, Phys. Chem. Chem. Phys. **16**, 16 407–16 418 (2014).

[74] W. J. D. Beenken and T. Pullerits, *Spectroscopic Units in Conjugated Polymers: A Quantum Chemically Founded Concept?*, J. Phys. Chem. B **108**, 6164–6169 (2004).

[75] N. Christensson, H. F. Kauffmann, T. Pullerits and T. Mančal, *Origin of Long-Lived Coherences in Light-Harvesting Complexes*, J. Phys. Chem. B **116**, 7449–7454 (2012).

[76] H. M. Senn and W. Thiel, *QM/MM Methods for Biomolecular Systems*, Angewandte Chemie International Edition **48**, 1198–1229 (2009).

[77] A. Warshel and M. Levitt, *Theoretical studies of enzymic reactions: Dielectric, electrostatic and steric stabilization of the carbonium ion in the reaction of lysozyme*, Journal of Molecular Biology **103**, 227 – 249 (1976).

[78] M. J. Field, P. A. Bash and M. Karplus, *A combined quantum mechanical and molecular mechanical potential for molecular dynamics simulations*, Journal of Computational Chemistry **11**, 700–733 (1990).

[79] J. Lameira, I. Kupchencko and A. Warshel, *Enhancing Paradynamics for QM/MM Sampling of Enzymatic Reactions*, The Journal of Physical Chemistry B **120**, 2155–2164 (2016).

[80] C. Bo and F. Maseras, *QM/MM methods in inorganic chemistry*, Dalton Trans. 2911–2919 (2008).

[81] P. Sherwood, A. H. de Vries, M. F. Guest, G. Schreckenbach, C. A. Catlow, S. A. French, A. A. Sokol, S. T. Bromley, W. Thiel, A. J. Turner, S. Billeter, F. Terstegen, S. Thiel, J. Kendrick, S. C. Rogers, J. Casci, M. Watson, F. King, E. Karlsen, M. Sjvoll, A. Fahmi, A. Schfer and C. Lennartz, *QUASI: A general purpose implementation of the QM/MM approach and its application to problems in catalysis*, Journal of Molecular Structure: {THEOCHEM} **632**, 1 – 28 (2003).

[82] C. Olbrich and U. Kleinekathöfer, *From atomistic modeling to electronic properties of light-harvesting systems*, in *Quantum Efficiency in Complex Systems, Part II: From Molecular Aggregates to Organic Solar Cells*, edited by U. Würfel, M. Thorwart and E. R. Weber, vol. 85 of *Semiconductors and Semimetals*, 83–114 (Academic Press, Burlington, 2011).

[83] D. W. Zhang, Y. Xiang and J. Z. H. Zhang, *New Advance in Computational Chemistry: Full Quantum Mechanical ab Initio Computation of StreptavidinBiotin Interaction Energy*, The Journal of Physical Chemistry B **107**, 12 039–12 041 (2003).

[84] G. D. Scholes, K. P. Ghiggino, A. M. Oliver and M. N. Paddon-Row, *Through-space and through-bond effects on exciton interactions in rigidly linked dinaphthyl molecules*, Journal of the American Chemical Society **115**, 4345–4349 (1993).

[85] V. May and O. Kühn, *Charge and Energy Transfer in Molecular Systems* (Wiley–VCH, Berlin, 2011), 3rd edn..

[86] C. Olbrich, T. L. C. Jansen, J. Liebers, M. Aghtar, J. Strümpfer, K. Schulten, J. Knoester and U. Kleinekathöfer, *From atomistic modeling to excitation dynamics and two-dimensional spectra of the FMO light-harvesting complex*, J. Phys. Chem. B **115**, 8609–8621 (2011).

[87] J. Adolphs, F. Müh, M. E. Madjet, M. Schmidt am Busch and T. Renger, *Structure-Based Calculations of Optical Spectra of Photosystem I Suggest an Asymmetric Light-Harvesting Process*, J. Am. Chem. Soc. **132**, 3331–3343 (2010).

[88] A. G. Dijkstra, T. L. C. Jansen and J. Knoester, *Localization and coherent dynamics of excitons in the two-dimensional optical spectrum of molecular J-aggregates*, J. Chem. Phys. **128**, 164 511 (2008).

[89] M. Aghtar, J. Liebers, J. Strümpfer, K. Schulten and U. Kleinekathöfer, *Juxtaposing density matrix and classical path-based wave packet dynamics*, J. Chem. Phys. **136**, 214 101–9 (2012).

[90] A. Muñoz Losa, C. Curutchet, I. F. Galván and B. Mennucci, *Quantum mechanical methods applied to excitation energy transfer: A comparative analysis on excitation energies and electronic couplings*, J. Chem. Phys. **129**, 034104 (2008).

[91] C. Didraga and J. Knoester, *Absorption and dichroism spectra of cylindrical J aggregates and chlorosomes of green bacteria*, Journal of Luminescence **102103**, 60 – 66 (2003), proceedings of the 2002 International Conference on Luminescence and Optical Spectroscopy of Condensed Matter.

[92] T. Renger and F. Müh, *Understanding Photosynthetic Light-Harvesting: A Bottom Up Theoretical Approach*, Phys. Chem. Chem. Phys. **15**, 3348–3371 (2013).

[93] T. Brixner, J. Stenger, H. M. Vaswani, M. Cho, R. E. Blankenship and G. R. Fleming, *Two-dimensional spectroscopy of electronic couplings in photosynthesis*, Nature **434**, 625–628 (2005).

[94] J. Strümpfer, M. Şener and K. Schulten, *How Quantum Coherence Assists Photosynthetic Light-Harvesting*, J. Phys. Chem. Lett. **3**, 536–542 (2012).

[95] F. Caruso, A. W. Chin, A. Datta, S. F. Huelga and M. B. Plenio, *Highly efficient energy excitation transfer in light-harvesting complexes: The fundamental role of noise-assisted transport*, J. Chem. Phys. **131**, 105 106 (2009).

[96] G. D. Scholes, G. R. Fleming, A. Olaya Castro and R. van Grondelle, *Lessons from nature about solar light harvesting*, Nat. Chem. **3**, 763–764 (2011).

[97] D. E. Tronrud, J. Wen, L. Gay and R. E. Blankenship, *The structural basis for the difference in absorbance spectra for the FMO antenna protein from various green sulfur bacteria*, Photosynth. Res. **100**, 79–87 (2009).

[98] M. Aghtar, J. Strümpfer, C. Olbrich, K. Schulten and U. Kleinekathöfer, *Different Types of Vibrations Interacting with Electronic Excitations in Phycoerythrin 545 and Fenna-Matthews-Olson Antenna Systems*, J. Phys. Chem. Lett. **5**, 3131–3137 (2014).

[99] M. Aghtar, J. Strümpfer, C. Olbrich, K. Schulten and U. Kleinekathöfer, *The FMO Complex in a Glycerol-Water Mixture*, J. Phys. Chem. B **117**, 7157–7163 (2013).

[100] N. H. List, C. Curutchet, S. Knecht, B. Mennucci and J. Kongsted, *Toward Reliable Prediction of the Energy Ladder in Multichromophoric Systems: A Benchmark Study on the FMO Light-Harvesting Complex*, J. Chem. Theory Comput. **9**, 4928–4938 (2013).

[101] C. Kreisbeck and T. Kramer, *Long-Lived Electronic Coherence in Dissipative Exciton Dynamics of Light-Harvesting Complexes*, J. Phys. Chem. Lett. **3**, 2828–2833 (2012).

[102] P. Nalbach and M. Thorwart, *The role of discrete molecular modes in the coherent exciton dynamics in FMO*, J. Phys. B: At., Mol. Opt. Phys. **45**, 154 009– (2012).

[103] C. Olbrich, J. Strümpfer, K. Schulten and U. Kleinekathöfer, *Quest for spatially correlated fluctuations in the FMO light-harvesting complex*, J. Phys. Chem. B **115**, 758–764 (2011).

[104] C. Olbrich, J. Strümpfer, K. Schulten and U. Kleinekathöfer, *Theory and Simulation of the Environmental Effects on FMO Electronic Transitions*, J. Phys. Chem. Lett. **2**, 1771–1776 (2011).

[105] A. Chenu, N. Christensson, H. F. Kauffmann and T. Mančal, *Enhancement of Vibronic and Ground-State Vibrational Coherences in 2D Spectra of Photosynthetic Complexes*, Sci. Rep. **3**, 2029 (2013).

[106] C. König and J. Neugebauer, *Quantum chemical description of absorption properties and excited-state processes in photosynthetic systems.*, ChemPhysChem **13**, 386–425 (2012).

[107] A. Damjanović, I. Kosztin, U. Kleinekathöfer and K. Schulten, *Excitons in a Photosynthetic Light-Harvesting System: A Combined Molecular Dynamics, Quantum Chemistry and Polaron Model Study*, Phys. Rev. E **65**, 031 919 (2002).

[108] S. Shim, P. Rebentrost, S. Valleau and A. Aspuru Guzik, *Atomistic Study of the Long-Lived Quantum Coherences in the Fenna-Matthew-Olson Complex*, Biophys. J. **102**, 649–660 (2012).

[109] S. Valleau, A. Eisfeld and A. Aspuru Guzik, *On the alternatives for bath correlators and spectral densities from mixed quantum-classical simulations*, J. Chem. Phys. **137**, 224 103–13 (2012).

[110] H. W. Kim, A. Kelly, J. W. Park and Y. M. Rhee, *All-Atom Semiclassical Dynamics Study of Quantum Coherence in Photosynthetic Fenna-Matthews-Olson Complex*, J. Am. Chem. Soc. **134**, 11 640–11 651 (2012).

[111] J. Gao, W.-J. Shi, J. Ye, X. Wang, H. Hirao and Y. Zhao, *QM/MM Modeling of Environmental Effects on Electronic Transitions of the FMO Complex*, J. Phys. Chem. B **117**, 3488–3495 (2013).

[112] E. Rivera, D. Montemayor, M. Masia and D. F. Coker, *Influence of Site-Dependent Pigment-Protein Interactions on Excitation Energy Transfer in Photosynthetic Light Harvesting*, J. Phys. Chem. B **117**, 5510–5521 (2013).

[113] L. Zhang, D.-A. Silva, H. Zhang, A. Yue, Y. Yan and X. Huang, *Dynamic Protein Conformations Preferentially Drive Energy Transfer Along the Active Chain of the Photosystem Ii Reaction Centre*, Nat. Commun. **5**, 4170 (2014).

[114] L. Viani, C. Curutchet and B. Mennucci, *Spatial and Electronic Correlations in the PE545 Light-Harvesting Complex*, J. Phys. Chem. Lett. **4**, 372–377 (2013).

[115] L. Viani, M. Corbella, C. Curutchet, E. J. O'Reilly, A. Olaya Castro and B. Mennucci, *Molecular Basis of the Exciton-phonon Interactions in the PE545 Light-harvesting Complex*, Phys. Chem. Chem. Phys. **16**, 16 302–16 311 (2014).

[116] S. Jurinovich, L. Viani, C. Curutchet and B. Mennucci, *Limits and Potentials of Quantum Chemical Methods in Modelling Photosynthetic Antennae*, Phys. Chem. Chem. Phys. **17**, 30 783–30 792 (2015).

[117] M. Ceccarelli, P. Procacci and M. Marchi, *An ab initio force field for the cofactors of bacterial photosynthesis*, J. Comput. Chem. **24**, 129–132 (2003).

[118] K. Karki and D. Roccatano, *Molecular Dynamics Simulation Study of Chlorophyll a in Different Organic Solvents*, J. Chem. Theory Comput. **7**, 1131–1140 (2011).

[119] M. G. Cory, M. C. Zerner, X. Hu and K. Schulten, *Electronic Excitations in Aggregates of Bacteriochlorophylls*, J. Phys. Chem. B **102**, 7640–7650 (1998).

[120] C. Olbrich and U. Kleinekathöfer, *Time-dependent atomistic view on the electronic relaxation in light-harvesting system II*, J. Phys. Chem. B **114**, 12 427–12 437 (2010).

[121] M. Higashi, T. Kosugi, S. Hayashi and S. Saito, *Theoretical Study on Excited States of Bacteriochlorophyll a in Solutions with Density Functional Assessment*, J. Phys. Chem. B **118**, 10 906–10 918 (2014).

[122] M. Wanko, M. Hoffmann, P. Strodel, A. Koslowski, W. Thiel, F. Neese, T. Frauenheim and M. Elstner, *Calculating absorption shifts for retinal proteins: Computational Challenges*, J. Phys. Chem. B **109**, 3606 (2005).

[123] S. Jurinovich, C. Curutchet and B. Mennucci, *The Fenna-Matthews-Olson Protein Revisited: A Fully Polarizable (TD)DFT/MM Description*, ChemPhysChem **15**, 3194–3204 (2014).

[124] W. F. Humphrey, A. Dalke and K. Schulten, *VMD – Visual Molecular Dynamics*, J. Mol. Graph. **14**, 33–38 (1996).

[125] J. C. Phillips, R. Braun, W. Wang, J. Gumbart, E. Tajkhorshid, E. Villa, C. Chipot, R. D. Skeel, L. Kale and K. Schulten, *Scalable molecular dynamics with NAMD*, J. Comput. Chem. **26**, 1781–1802 (2005).

[126] T. Petrenko and F. Neese, *Analysis and prediction of absorption band shapes, fluorescence band shapes, resonance Raman intensities, and excitation profiles using the time-dependent theory of electronic spectroscopy*, J. Chem. Phys. **127**, 164 319 (2007).

[127] W. L. Jorgensen, J. Chandrasekhar, J. D. Madura, R. W. Impey and M. L. Klein, *Comparison of simple potential functions for simulating liquid water*, J. Chem. Phys. **79**, 926–935 (1983).

[128] W. Jorgensen and J. Madura, *Temperature and Size Dependence for Monte-Carlo Simulations of TIP4P Water*, Mol. Phys. **56**, 1381–1392 (1985).

[129] I. P. Mercer, I. R. Gould and D. R. Klug, *A Quantum Mechanical/Molecular Mechanical Approach to Relaxation Dynamics: Calculation of the Optical Properties of Solvated Bacteriochlorophyll-a*, J. Phys. Chem. B **103**, 7720–7727 (1999).

[130] L. Janosi, I. Kosztin and A. Damjanović, *Theoretical prediction of spectral and optical properties of bacteriochlorophylls in thermally disordered LH2 antenna complexes*, J. Chem. Phys. **125**, 014 903 (2006).

[131] M. Wendling, T. Pullerits, M. A. Przyjalgowski, S. I. E. Vulto, T. J. Aartsma, R. v. Grondelle and H. v. Amerongen, *Electron-Vibrational Coupling in the Fenna-Matthews-Olson Complex of Prosthecochloris aestuarii Determined by Temperature-Dependent Absorption and Fluorescence Line-Narrowing Measurement*, J. Phys. Chem. B **104**, 5825–5831 (2000).

[132] J. Adolphs and T. Renger, *How proteins trigger excitation energy transfer in the FMO complex of green sulfur bacteria.*, Biophys J **91**, 2778–2797 (2006).

[133] D. R. Martin and D. V. Matyushov, *Non-Gaussian Statistics and Nanosecond Dynamics of Electrostatic Fluctuations Affecting Optical Transitions in Proteins*, J. Phys. Chem. B **116**, 10 294–10 300 (2012).

[134] C. M. Isborn, A. W. Götz, M. A. Clark, R. C. Walker and T. J. Martinez, *Electronic Absorption Spectra from MM and ab Initio QM/MM Molecular Dynamics: Environmental Effects on the Absorption Spectrum of Photoactive Yellow Protein*, J. Chem. Theory Comput. **8**, 5092–5106 (2012).

[135] D. Flaig, M. Beer and C. Ochsenfeld, *Convergence of Electronic Structure with the Size of the QM Region: Example of QM/MM NMR Shieldings*, J. Chem. Theory Comput. **8**, 2260–2271 (2012).

[136] G. Ritschel, J. Roden, W. T. Strunz, A. Aspuru Guzik and A. Eisfeld, *Absence of Quantum Oscillations and Dependence on Site Energies in Electronic Excitation Transfer in the Fenna-Matthews-Olson Trimer*, J. Phys. Chem. Lett. **2**, 2912–2917 (2011).

[137] C. A. Mujica Martinez, P. Nalbach and M. Thorwart, *Quantification of Non-markovian Effects in the Fenna-Matthews-Olson Complex*, Phys. Rev. E **88**, 062 719 (2013).

[138] O. F. Lange, D. van der Spoel and B. L. de Groot, *Scrutinizing Molecular Mechanics Force Fields on the Submicrosecond Timescale with NMR Data*, Biophys. J. **99**, 647–655 (2010).

[139] E. A. Cino, W.-Y. Choy and M. Karttunen, *Comparison of Secondary Structure Formation Using 10 Different Force Fields in Microsecond Molecular Dynamics Simulations*, J. Chem. Theory Comput. **8**, 2725–2740 (2012).

[140] K. Lindorff-Larsen, P. Maragakis, S. Piana, M. P. Eastwood, R. O. Dror and D. E. Shaw, *Systematic Validation of Protein Force Fields Against Experimental Data.*, PLoS One **7**, e32 131 (2012).

[141] J. Wang, W. Zhuang, S. Mukamel and R. Hochstrasser, *Two-Dimensional Infrared Spectroscopy as a Probe of the Solvent Electrostatic Field for a Twelve Residue Peptide*, J. Phys. Chem. B **112**, 5930–5937 (2007).

[142] P. S. Georgoulia and N. M. Glykos, *Using J-Coupling Constants for Force Field Validation: Application to Hepta-alanine*, J. Phys. Chem. B **115**, 15 221–15 227 (2011).

[143] K. Kwac and E. Geva, *A Mixed Quantum-Classical Molecular Dynamics Study of anti-Tetrol and syn-Tetrol Dissolved in Liquid Chloroform: Hydrogen-Bond Structure and Its Signature on the Infrared Absorption Spectrum*, J. Phys. Chem. B **117**, 16 493–16 505 (2013).

[144] T. L. C. Jansen, *Linear Absorption and Two-Dimensional Infrared Spectra of N-Methylacetamide in Chloroform Revisited: Polarizability and Multipole Effects*, J. Phys. Chem. B **118**, 8162–8169 (2014).

[145] J. T. Yurkov, V V. Beatty, *Aerobic Anoxygenic Phototrophic Bacteria*, Microbiol Mol Biol Rev **62**, 695–724 (1998).

[146] H. van Amerongen, L. Valkunas and R. van Grondelle, *Photosynthetic Excitons* (World Scientific, Singapore, 2000).

[147] J. Koepke, X. Hu, C. Muenke, K. Schulten and H. Michel, *The crystal structure of the light harvesting complex II (B800-850) from Rhodospirillum molischianum*, Structure **4**, 581–597 (1996).

[148] R. Fenna, B. Matthews, J. Olson and E. Shaw, *Structure of a bacteriochlorophyll-protein from the green photosynthetic bacterium Chlorobium limicola: Crystallographic evidence for a trimer*, J. Mol. Biol. **84**, 231–240 (1974).

[149] H. Grubmüller and K. Schulten, *Special issue: Advances in molecular dynamics simulations*, J. Struct. Biol. **157**, 443 (2007).

[150] W. D. Cornell, P. Cieplak, C. I. Bayly, I. R. Gould, K. M. Merz, D. M. Ferguson, D. C. Spellmeyer, T. Fox, J. W. Caldwell and P. A. Kollman, *A Second Generation Force Field for the Simulation of Proteins, Nucleic Acids, and Organic Molecules*, Journal of the American Chemical Society **117**, 5179–5197 (1995).

[151] B. R. Brooks, C. L. Brooks, A. D. Mackerell, L. Nilsson, R. J. Petrella, B. Roux, Y. Won, G. Archontis, C. Bartels, S. Boresch, A. Caflisch, L. Caves, Q. Cui, A. R. Dinner, M. Feig, S. Fischer, J. Gao, M. Hodoscek, W. Im, K. Kuczera, T. Lazaridis, J. Ma, V. Ovchinnikov, E. Paci, R. W. Pastor, C. B. Post, J. Z. Pu, M. Schaefer, B. Tidor, R. M. Venable, H. L. Woodcock, X. Wu, W. Yang, D. M. York and M. Karplus, *CHARMM: The biomolecular simulation program*, Journal of Computational Chemistry **30**, 1545–1614 (2009).

[152] C. Oostenbrink, A. Villa, A. E. Mark and W. F. Van Gunsteren, *A biomolecular force field based on the free enthalpy of hydration and solvation: The GROMOS force-field*

parameter sets 53A5 and 53A6, Journal of Computational Chemistry **25**, 1656–1676 (2004).

[153] W. L. Jorgensen and J. Tirado-Rives, *The OPLS [optimized potentials for liquid simulations] potential functions for proteins, energy minimizations for crystals of cyclic peptides and crambin*, Journal of the American Chemical Society **110**, 1657–1666 (1988).

[154] J. Wang, R. M. Wolf, J. W. Caldwell, P. A. Kollman and D. A. Case, *Development and testing of a general amber force field*, Journal of computational chemistry **25**, 1157–1174 (2004).

[155] K. Vanommeslaeghe, E. Hatcher, C. Acharya, S. Kundu, S. Zhong, J. Shim, E. Darian, O. Guvench, P. Lopes, I. Vorobyov and A. D. Mackerell, *CHARMM general force field: A force field for drug-like molecules compatible with the CHARMM all-atom additive biological force fields*, J. Comput. Chem. **31**, 671–690 (2010).

[156] C. I. Bayly, P. Cieplak, W. Cornell and P. A. Kollman, *A Well-behaved Electrostatic Potential Based Method Using Charge Restraints for Deriving Atomic Charges: The RESP Model*, J. Phys. Chem. **97**, 10 269–10 280 (1993).

[157] . William L. Jorgensen, D. S. Maxwell, and J. Tirado-Rives, *Development and Testing of the OPLS All-Atom Force Field on Conformational Energetics and Properties of Organic Liquids*, Journal of the American Chemical Society **118**, 11 225–11 236 (1996).

[158] E. R. Hatcher, O. Guvench and A. D. MacKerell, *CHARMM Additive All-Atom Force Field for Acyclic Polyalcohols, Acyclic Carbohydrates, and Inositol*, J. Chem. Theory Comput. **5**, 1315–1327 (2009).

[159] Carles Curutchet and Benedetta Mennucci, *Quantum Chemical Studies of Light Harvesting*, Chem. Rev. **0**, null (2016), pMID: 26958698.

[160] B. W. Matthews, R. E. Fenna, M. C. Bolognesi, M. F. Schmid and J. M. Olson, *Structure of a bacteriochlorophyll a-protein from the green photosynthetic bacterium Prosthecochloris aestuarii*, J. Mol. Biol. **131**, 259–265 (1979).

[161] S. Chandrasekaran, M. Aghtar, S. Valleau, A. Aspuru-Guzik and U. Kleinekathöfer, *Influence of Force Fields and Quantum Chemistry Approach on Spectral Densities of BChl a in Solution and in FMO Proteins*, J. Phys. Chem. B **119**, 9995–10 004 (2015).

[162] M. Aghtar and U. Kleinekathöfer, *Environmental Coupling and Population Dynamics in the PE545 Light-harvesting Complex*, J. Lumin. **169**, 406–409 (2016).

[163] T. Renger, A. Klinger, F. Steinecker, M. Schmidt am Busch, J. Numata and F. Müh, *Normal Mode Analysis of the Spectral Density of the Fenna-Matthews-Olson Light-Harvesting Protein: How the Protein Dissipates the Excess Energy of Excitons*, J. Phys. Chem. B **116**, 14 565–14 580 (2012).

[164] V. May and O. Kühn, *Charge and Energy Transfer in Molecular Systems* (Wiley–VCH, Berlin, 2000).

[165] X. Wang, G. Ritschel, S. Wuster and A. Eisfeld, *Open quantum system parameters for light harvesting complexes from molecular dynamics*, Phys. Chem. Chem. Phys. **17**, 25 629–25 641 (2015).

[166] M. B. J. S. J. C. Foloppe, F. Ferrand, *Structural model of the photosynthetic reaction center of Rhodobacter capsulatus*, Proteins: Struct. Funct. Gen. **22**, 226–244 (1995).

[167] P. Palencar, F. Vacha and M. Kuty, *Force field development on pigments of photosystem 2 reaction centre*, Photosynthetica **43**, 417–420 (2005).

[168] L. Zhang, D.-A. Silva, Y. Yan and X. Huang, *Force field development for cofactors in the photosystem II*, J. Comput. Chem. **33**, 1969–1980 (2012).

[169] C. G. Mayne, J. Saam, K. Schulten, E. Tajkhorshid and J. C. Gumbart, *Rapid parameterization of small molecules using the force field toolkit*, Journal of Computational Chemistry **34**, 2757–2770 (2013).

[170] K. Vanommeslaeghe, E. P. Raman and J. A. D. MacKerell, *Automation of the CHARMM General Force Field (CGenFF) II: Assignment of Bonded Parameters and Partial Atomic Charges*, Journal of Chemical Information and Modeling **52**, 3155–3168 (2012), pMID: 23145473.

[171] K. Vanommeslaeghe, E. P. Raman and A. MacKerell Jr, *Automation of the CHARMM General Force Field (CGenFF) II: assignment of bonded parameters and partial atomic charges*, J. Chem. Inf. Model. **52**, 3155–3168 (2012).

[172] M. J. Frisch, G. W. Trucks, H. B. Schlegel, G. E. Scuseria, M. A. Robb, J. R. Cheeseman, G. Scalmani, V. Barone, B. Mennucci, G. A. Petersson, H. Nakatsuji, M. Caricato, X. Li, H. P. Hratchian, A. F. Izmaylov, J. Bloino, G. Zheng, J. L. Sonnenberg, M. Hada, M. Ehara, K. Toyota, R. Fukuda, J. Hasegawa, M. Ishida, T. Nakajima, Y. Honda, O. Kitao, H. Nakai, T. Vreven, J. A. Montgomery, Jr., J. E. Peralta, F. Ogliaro, M. Bearpark, J. J. Heyd, E. Brothers, K. N. Kudin, V. N. Staroverov,

R. Kobayashi, J. Normand, K. Raghavachari, A. Rendell, J. C. Burant, S. S. Iyengar, J. Tomasi, M. Cossi, N. Rega, J. M. Millam, M. Klene, J. E. Knox, J. B. Cross, V. Bakken, C. Adamo, J. Jaramillo, R. Gomperts, R. E. Stratmann, O. Yazyev, A. J. Austin, R. Cammi, C. Pomelli, J. W. Ochterski, R. L. Martin, K. Morokuma, V. G. Zakrzewski, G. A. Voth, P. Salvador, J. J. Dannenberg, S. Dapprich, A. D. Daniels, Ö. Farkas, J. B. Foresman, J. V. Ortiz, J. Cioslowski and D. J. Fox, *Gaussian*∼ 09 *Revision E.01* (2009), gaussian Inc. Wallingford CT 2009.

[173] R. E. Christofferson, *Basic Principles and Techniques of Molecular Quantum Mechanics* (Springer, New York, 1989).

[174] L. Kalé, R. Skeel, M. Bhandarkar, R. Brunner, A. Gursoy, N. Krawetz, J. Phillips, A. Shinozaki, K. Varadarajan and K. Schulten, *NAMD2: Greater scalability for parallel molecular dynamics*, J. Comp. Phys. **151**, 283 (1999).

[175] N.-T. Van Oanh, C. Falvo, F. Calvo, D. Lauvergnat, M. Basire, M.-P. Gaigeot and P. Parneix, *Improving anharmonic infrared spectra using semiclassically prepared molecular dynamics simulations*, Phys. Chem. Chem. Phys. **14**, 2381–2390 (2012).

[176] A. Pavlova and J. C. Gumbart, *Parametrization of macrolide antibiotics using the force field toolkit*, Journal of Computational Chemistry **36**, 2052–2063 (2015).

[177] S. Chandrasekaran, M. Aghtar, S. Valleau, A. Aspuru-Guzik and U. Kleinekathfer, *Influence of Force Fields and Quantum Chemistry Approach on Spectral Densities of BChl a in Solution and in FMO Proteins*, The Journal of Physical Chemistry B **119**, 9995–10 004 (2015), pMID: 26156758.

[178] X. Hu, T. Ritz, A. Damjanović, F. Autenrieth and K. Schulten, *Photosynthetic apparatus of purple bacteria*, Q. Rev. Biophys. **35**, 1–62 (2002).

[179] E. Collini, C. Y. Wong, K. E. Wilk, P. M. G. Curmi, P. Brumer and G. D. Scholes, *Coherently wired light-harvesting in photosynthetic marine algae at ambient temperature*, Nature **463**, 644–647 (2010).

[180] C. Y. Wong, R. M. Alvey, D. B. Turner, K. E. Wilk, D. A. Bryant, P. M. G. Curmi, R. J. Silbey and G. D. Scholes, *Electronic coherence lineshapes reveal hidden excitonic correlations in photosynthetic light harvesting*, Nat. Chem. **4**, 396–404 (2012).

[181] F. Fassioli, R. Dinshaw, P. C. Arpin and G. D. Scholes, *Photosynthetic Light Harvesting: Excitons and Coherence*, J. Roy. Soc. Interface. **11**, 1742–5662 (2014).

[182] G. H. Richards, K. E. Wilk, P. M. G. Curmi and J. A. Davis, *Disentangling Electronic and Vibrational Coherence in the Phycocyanin-645 Light-harvesting Complex*, J. Phys. Chem. Lett. **5**, 43–49 (2013).

[183] P. C. Arpin, D. B. Turner, S. D. McClure, C. C. Jumper, T. Mirkovic, J. R. Challa, J. Lee, C. Y. Teng, B. R. Green, K. E. Wilk, P. M. G. Curmi, K. Hoef Emden, D. W. McCamant and G. D. Scholes, *Spectroscopic Studies of Cryptophyte Light Harvesting Proteins: Vibrations and Coherent Oscillations*, J. Phys. Chem. B **119**, 10 025–10 034 (2015).

[184] N. K. Singh, R. R. Sonani, R. P. Rastogi and D. Madamwar, *The Phycobilisomes: An Early Requisite for Efficient Photosynthesis in Cyanobacteria*, EXCLI J. **14**, 268–289 (2015).

[185] G. J. Wedemayer, D. E. Wemmer and A. N. Glazer, *Phycobilins of Cryptophycean Algae. Structures of Novel Bilins with Acryloyl Substituents from Phycoerythrin 566*, J. Biol. Chem. **266**, 4731–4741 (1991).

[186] G. J. Wedemayer, D. G. Kidd, D. E. Wemmer and A. N. Glazer, *Phycobilins of Cryptophycean Algae. Occurrence of Dihydrobiliverdin and Mesobiliverdin in Cryptomonad Biliproteins*, J. Biol. Chem. **267**, 7315–7331 (1992).

[187] D. E. Wemmer, G. J. Wedemayer and A. N. Glazer, *Phycobilins of Cryptophycean Algae. Novel Linkage of Dihydrobiliverdin in a Phycoerythrin 555 and a Phycocyanin 645.*, J. Biol. Chem. **268**, 1658–69 (1993).

[188] A. N. Glazer and G. J. Wedemayer, *Cryptomonad Biliproteins — an Evolutionary Perspective*, Photosynth. Res. **46**, 93–105 (1995).

[189] K. E. Overkamp, S. Langklotz, M. Aras, S. Helling, K. Marcus, J. E. Bandow, K. Hoef Emden and N. Frankenberg Dinkel, *Chromophore Composition of the Phycobiliprotein Cr-PC577 from the Cryptophyte Hemiselmis Pacifica*, Photosynth. Res. **122**, 293–304 (2014).

[190] K. E. Wilk, S. J. Harrop, L. Jankova, D. Edler, G. Keenan, F. Sharples, R. G. Hiller and P. M. Curmi, *Evolution of a light-harvesting protein by addition of new subunits and rearrangement of conserved elements: Crystal structure of a cryptophyte phycoerythrin at 1.63-Å resolution*, Proc. Natl. Acad. Sci. USA **96**, 8901–8906 (1999).

[191] T. Mirkovic, A. B. Doust, J. Kim, K. E. Wilk, C. Curutchet, B. Mennucci, R. Cammi, P. M. G. Curmi and G. D. Scholes, *Ultrafast Light Harvesting Dynamics in the Cryptophyte Phycocyanin 645*, Photochem. Photobiol. Sci. **6**, 964–975 (2007).

[192] P. Huo and D. F. Coker, *Theoretical Study of Coherent Excitation Energy Transfer in Cryptophyte Phycocyanin 645 at Physiological Temperature*, J. Phys. Chem. Lett. **2**, 825–833 (2011).

[193] W.-G. Lee, A. Kelly and Y. M. Rhee, *Behavior of Poisson Bracket Mapping Equation in Studying Excitation Energy Transfer Dynamics of Cryptophyte Phycocyanin 645 Complex*, Bull. Korean Chem. Soc. **33**, 933–940 (2012).

[194] C. Curutchet, V. I. Novoderezhkin, J. Kongsted, A. Munoz Losa, R. van Grondelle, G. D. Scholes and B. Mennucci, *Energy Flow in the Cryptophyte PE545 Antenna Is Directed by Bilin Pigment Conformation*, J. Phys. Chem. B **117**, 4263–4273 (2013).

[195] X. Leng and X.-T. Liang, *Simulation of Two-Dimensional Electronic Spectra of Phycoerythrin 545 at Ambient Temperature*, J. Phys. Chem. B **118**, 12 366–12 370 (2014).

[196] J. Wang, P. Cieplak and P. A. Kollman, *How well does a restrained electrostatic potential (RESP) model perform in calculating conformational energies of organic and biological molecules?*, Journal of Computational Chemistry **21**, 1049–1074 (2000).

[197] S. F. Alberti and J. Echave, *Theoretical study of the solvatochromism of a merocyanine dye*, Chem. Phys. **223**, 183–194 (1997).

[198] M. E. Madjet, A. Abdurahman and T. Renger, *Intermolecular coulomb couplings from ab initio electrostatic potentials: Application to optical transitions of strongly coupled pigments in photosynthetic antennae and reaction centers*, J. Phys. Chem. B **110**, 17 268–81 (2006).

[199] T. Renger and F. Müh, *Theory of excitonic couplings in dielectric media :Foundation of Poisson-TrEsp method and application to photosystem I trimers*, Photosynth. Res. **111**, 47–52 (2012).

[200] A. B. Doust, C. N. Marai, S. J. Harrop, K. E. Wilk, P. M. Curmi and G. D. Scholes, *Developing a structure-function model for the cryptophyte phycoerythrin 545 using ultrahigh resolution crystallography and ultrafast laser spectroscopy*, J. Mol. Biol. **344**, 135–143 (2004).

[201] V. I. Novoderezhkin, A. B. Doust, C. Curutchet, G. D. Scholes and R. van Grondelle, *Excitation dynamics in Phycoerythrin 545: modeling of steady-state spectra and transient absorption with modified Redfield theory*, Biophys. J. **99**, 344–352 (2010).

[202] T. Lu and F. Chen, *Multiwfn: A Multifunctional Wavefunction Analyzer*, J. Comput. Chem. **33**, 580–592 (2012).

[203] L. Mühlbacher and U. Kleinekathöfer, *Preparational Effects on the Excitation Energy Transfer in the FMO Complex*, J. Phys. Chem. B **116**, 3900–3906 (2012).

[204] J. Strümpfer and K. Schulten, *Open Quantum Dynamics Calculations with the Hierarchy Equations of Motion on Parallel Computers*, J. Chem. Theory Comput. **8**, 2808–2816 (2012).

[205] A. B. Doust, K. E. Wilk, P. M. Curmi and G. D. Scholes, *The photophysics of cryptophyte light-harvesting*, J. Photochem. Photobiol. A: Chem. **184**, 1–17 (2006).

[206] B. Blachowicz, Lasiak, M. Maj, M. Cho and R. W. Gora, *Distributed Multipolar Expansion Approach to Calculation of Excitation Energy Transfer Couplings*, J. Chem. Theory Comput. **11**, 3259–3266 (2015).

[207] Elise P. Kenny and Ivan Kassal, *Benchmarking Calculations of Excitonic Couplings Between Bacteriochlorophylls*, J. Phys. Chem. B **120**, 25–32 (2016).

[208] B. Krueger, G. Scholes and G. Fleming, *Calculation of Couplings and Energy Transfer Pathways Between the Pigments of LH2 by the ab initio Transition Density Cube Method*, J. Phys. Chem. B **102**, 5378–5386 (1998).

[209] C. Curutchet, J. Kongsted, A. Munoz Losa, H. Hossein Nejad, G. D. Scholes and B. Mennucci, *Photosynthetic light-harvesting is tuned by the heterogeneous polarizable environment of the protein*, J. Am. Chem. Soc. **133**, 3078–3084 (2011).

[210] H. Hossein Nejad, C. Curutchet, A. Kubica and G. D. Scholes, *Delocalization-Enhanced Long-Range Energy Transfer between Cryptophyte Algae PE545 Antenna Proteins*, J. Phys. Chem. B **115**, 5243–5243 (2011).

[211] A. Kolli, E. J. O'Reilly, G. D. Scholes and A. Olaya Castro, *The fundamental role of quantized vibrations in coherent light harvesting by cryptophyte algae*, J. Chem. Phys. **137**, 174 109–15 (2012).